

University of Alberta

Computational Study of the Water Cycle at the Surface of Mars

by

Jakub T. Zubik

A thesis submitted to the Faculty of Graduate Studies and Research
in partial fulfillment of the requirements for the degree of

Master of Science

Department of Mechanical Engineering

© Jakub T. Zubik

Fall 2012

Edmonton, Alberta

Permission is hereby granted to the University of Alberta Libraries to reproduce single copies of this thesis and to lend or sell such copies for private, scholarly or scientific research purposes only. Where the thesis is converted to, or otherwise made available in digital form, the University of Alberta will advise potential users of the thesis of these terms.

The author reserves all other publication and other rights in association with the copyright in the thesis and, except as herein before provided, neither the thesis nor any substantial portion thereof may be printed or otherwise reproduced in any material form whatsoever without the author's prior written permission.

This thesis is dedicated to my wife.

Abstract

To understand the water cycle on Mars, details of mass and energy transfer between the surface and the atmosphere are of importance. A complete model, involving transient variations of the water in gaseous and solid phases in the atmosphere and the regolith, is developed and solved numerically for results. The diffusion of water vapour in the ground is treated for Knudsen and thermal diffusion effects. Numerical simulations of the evening hours of Sol 70 of the Phoenix mission confirmed that a deposition of water can occur. The results show how phase change occurred right after the temperature of air is cooled down below the frost point and deposited on the surface as frost, then sublimated back into the atmosphere in the morning. Results of the two-dimensional model show that there are additional spatial fluctuations of fog structure resulting from variations in the nature and slope of the local terrain.

Preface

This thesis comprises six chapters. Chapter 1 introduces the Phoenix mission and the history of water on Mars including the recent studies. Chapter 2 describes the theory of modelling a multicomponent flow with heat and mass transfer in the atmosphere and regolith of Mars. Chapter 3 describes the numerical modelling part using Finite Volume Method. Chapter 4 shows the validation of the model during fog formation in the atmosphere and the validation of thermal diffusion in the regolith. Chapter 5 demonstrates the numerical models of water cycle based on Sol 70 of the Phoenix mission. Finally, chapter 6 contains conclusions and potential next steps of this work.

Acknowledgements

Thanks be to CSA and the University of Alberta for their financial support;
to my supervisor, Dr. Carlos Lange for his guidance, great inspiration and helpful suggestions throughout this work;
to my family for their support and understanding;
and most of all to my lab mates for many useful discussions and comments.

Contents

1	Introduction	1
1.1	The Phoenix Mission	2
1.2	Water Cycle Study at the Surface of Mars	5
2	Theory	10
2.1	Water Vapour and Ice Transport in the Martian Atmosphere .	11
2.1.1	Governing Equations	14
2.1.2	Simplified Equations for the Atmosphere	17
2.1.3	Sublimation/Deposition Source Term	18
2.1.4	Moist Parametrization	20
2.1.5	Binary Diffusion Coefficient	22
2.2	Water Vapour and Ice Transport in the Martian Regolith . . .	25
2.2.1	Governing Equations for the Regolith	28
2.2.2	Knudsen Diffusion	31

CONTENTS

2.2.3	Thermal Diffusion	35
2.3	Surface Temperature and Solar Radiation	40
3	Numerical Method	43
3.1	Numerical Code	44
3.2	Theory of Grid Independence	47
3.3	Numerical Implementation	48
3.4	Software Limitations	51
4	Validation and Verification	54
4.1	Validation of Near Surface Atmosphere	55
4.2	Grid Independence Analysis	60
4.3	Validation of Thermal Diffusion in the Regolith	62
5	Numerical Simulations	66
5.1	One-Dimensional Model of Sol 70 of the Phoenix Mission	67
5.1.1	Effect of Thermal Diffusion	73
5.2	Two-Dimensional Model of Sol 70 of the Phoenix Mission	75
6	Conclusions	81
6.1	Summary	81
6.2	Future Investigations	82

CONTENTS

References	83
A Derivations	96
A.1 Relationships for an ideal gas mixture	96
A.2 Mixture properties	97
A.3 Derivation of thermal energy equation	98
A.4 Numerical discretization	100
A.5 Relationships for the mass fluxes	104
A.6 Correlation equations for the functionals	105
A.7 Combination rules for mixtures	106
A.8 Relationships for the collision integrals	107
B Code	108
B.1 <i>thfactor.m</i>	108

List of Tables

1.1	Properties summary at the Phoenix landing site.	4
2.1	Regolith properties used in the simulations.	34
2.2	Molecular potential parameters.	38
4.1	Time integral of water vapour mass flux area average at a horizontal plane 1 mm above the surface, calculated at five grid levels.	61
4.2	Measured binary and effective diffusion coefficients for mixture of He-CO ₂ and calculated obstruction and thermal diffusion factors.	64
A.1	The coefficients a and b for the collision integrals.	107

List of Figures

1.1	Instruments on Phoenix Mars Lander. Image credit: NASA/JPL-Caltech/UA/Lockheed Martin.	3
2.1	Plot showing the minimum, maximum, and average temperature (left) and the total pressure (right) measured during the Phoenix mission.	11
2.2	Comparison of mixture viscosity (left) and thermal conductivity (right) obeying the linear mixture rule (dashed lines) with those showing deviations (solid lines).	14
2.3	Plot showing the phase diagrams for CO ₂ (left) and H ₂ O (right) [1, 2].	19
2.4	The binary diffusion coefficient for H ₂ O in CO ₂ as a function of temperature at 774 Pa.	23
2.5	Cubic cell model for a soil with ice accumulated around the solid particle.	27
2.6	Diagram showing definitions and directions for Darcy's law.	29
2.7	Generic shape of an interaction potential.	36

LIST OF FIGURES

2.8	Thermal diffusion factor for mixture of H ₂ O-CO ₂ at constant volume mixing ratio. Solid line shows the values of $\alpha_{T_{H_2O}}$ calculated from the force constants for the central potential and the dotted line for the Stockmayer molecular potential.	39
4.1	Surface energy fluxes calculated for Sol 30 of the Phoenix mission. S_{net} is the net solar irradiation flux, L_{net} is the net radiation from the ground, and R_{net} is the net radiation at the surface.	56
4.2	Temperature profiles for the Phoenix site at $L_S=90^\circ$ at 1719, 2100, 0000 and 0200 LT from the Sol 30 simulation.	57
4.3	Modelled relative humidity at the ground (solid) and at 2 m above the ground (dashed) for Phoenix sols 30 to 31.	58
4.4	Modelled water vapour mixing ratio for Phoenix sols 30 to 31.	59
4.5	Modelled water ice mixing ratio for Phoenix sols 30 to 31. . .	60
4.6	Time integral values of water vapour mass flux area average at different grid levels.	61
4.7	Time integral values of water vapour mass flux area average at different time-steps.	62
4.8	Sketch of the two-bulb experiment.	63
4.9	The two-bulb mesh.	64
4.10	The modelled (solid line) and experimental (triangles) results of thermodiffusion separation for He-CO ₂ binary mixture. . . .	65

LIST OF FIGURES

5.1	Surface energy fluxes calculated for Sol 70 of the Phoenix mission. S_{net} is the net solar irradiation flux, L_{net} is the net radiation from the ground, and R_{net} is the net radiation at the surface.	67
5.2	Observed 2 m (points) and modelled 2 m (solid line) temperatures for Sol 70 of the Phoenix mission.	68
5.3	The atmosphere temperature profiles at 17, 20, 22, 01, 04, and 06 LT during the Sol 70 simulations.	69
5.4	The regolith temperature profiles at 17, 20, 22, 01, 04, and 06 LT during the Sol 70 simulations.	70
5.5	Modelled relative humidity at different heights for Phoenix sols 70 to 71.	71
5.6	Modelled water vapour pressure at the ground (solid) and at 2 m above the ground (dashed) for Phoenix sols 70 to 71.	71
5.7	Modelled water ice mixing ratio at 2 m above the ground for Phoenix sols 70 to 71.	72
5.8	The regolith ice mixing ratio profiles at 02, 04, and 06 LT during the Sol 70 simulations.	73
5.9	Modelled water vapour mixing ratio at 5 cm above the ground for thermodiffusion (dashed) and non-thermodiffusion (solid) case.	74
5.10	Total average water vapour fluxes across a horizontal surface at 5 cm above the ground for thermodiffusion (triangles) and non-thermodiffusion (diamonds) case.	74
5.11	The regolith and near-surface temperature profiles at 17, 18, 19, and 20 LT during the Sol 70 simulations.	75

LIST OF FIGURES

5.12	View of the structured hexahedral mesh with local refinement used for 2-D simulations.	76
5.13	Modelled water vapour pressure at 2 m above the ground.	77
5.14	Temperature (left) and relative humidity (right) contours at 1930 LT.	78
5.15	Fog contours at 1925 LT (top left), 1930 LT (top right), 2200 LT (bottom left), and 2300 LT (bottom right).	79
5.16	Near-surface water vapour flux vectors at 1930 LT (left) and 2200 LT (right).	80
A.1	Hexahedral element.	102

List of Symbols

Latin symbols

A_v	Avogadro constant	mol^{-1}
a	Albedo	—
C_c	Cunningham correction factor	—
c_p	Specific heat at constant pressure	J/kg K
c_v	Volumetric heat capacity	$\text{J/m}^3 \text{K}$
c_α	Molar concentration of component α	mol/m^3
D_o	Pore diameter	m
$D_{\alpha K}$	Knudsen diffusion coefficient	m^2/s
$D_{\alpha\beta}$	Binary diffusion coefficient for the component α into β	m^2/s
d_{ice}	Diameter of ice particles	m
e_M	Mars eccentricity	—
G_S	Total solar energy incident	W/m^2
\mathbf{g}	Gravitational acceleration	m/s^2

LIST OF FIGURES

H	Sensible heat flux	W/m^2
h	Specific enthalpy	m^2/s^2
h_{GS}	Specific latent heat of phase change from vapour to solid	kJ/kg
I	Thermal inertia	$\text{J/m}^2 \text{ s}^{0.5} \text{ K}$
I_{rad}	Total surface energy loss by radiation	W/m^2
\mathbf{j}_α	Diffusive flux	$\text{kg/m}^2 \text{ s}$
K	Permeability	m^2
k	Thermal conductivity	W/m K
k_b	Stefan-Boltzmann constant	$\text{W/m}^2 \text{ K}^4$
k_T	Thermal diffusion ratio	—
L_d	Long-wave down-welling flux from the atmosphere	W/m^2
L_{net}	Net long-wave flux	W/m^2
L_u	Long-wave upwelling flux to the atmosphere	W/m^2
LE	Latent heat flux	W/m^2
L_S	Areocentric longitude of the sun	$^\circ$
M_w	Molecular weight	kg/mol
m	Total mass	kg
m_α	Mass of component α	kg
N	Molecular concentration	molecules/m^3
N_α	Partial molecular concentration of component α	molecules/m^3

LIST OF FIGURES

P	Mixture pressure	Pa
P_α	Partial pressure of component α	Pa
p	Order of the numerical scheme	–
\mathbf{Q}	Volumetric flow rate	m^3/s
Q	Heat generation per unit volume	W/m^3
\mathbf{q}	Heat flux vector	kg/s^3
q	Specific humidity	–
R	Universal gas constant	$\text{J}/\text{kmol K}$
R_p	Porous momentum resistance	$\text{kg}/\text{m}^2 \text{ s}^2$
R_{net}	Total net radiation at the surface	W/m^2
R_α	Specific gas constant for component α	$\text{J}/\text{kg K}$
r_p	Pore radius	m
r_α	Mass rate of production/consumption of component α	$\text{kg}/\text{m}^3 \text{ s}$
RH	Relative humidity	%
S_D	Direct solar irradiation at the horizontal surface	W/m^2
S_{net}	Net surface solar flux	W/m^2
S_{TOA}	Solar irradiation at the top of the atmosphere	W/m^2
T	Temperature	K
T_g	Surface temperature	K
t	Time	s

LIST OF FIGURES

V	Mixture volume	m^3
V_α	Partial volume of component α	m^3
\mathbf{v}	Mass average velocity	m/s
\mathbf{v}_α	Velocity of component α	m/s
\mathbf{w}	Darcy velocity or superficial velocity	m/s
w_r	Mixing ratio	—
x_α	Mole fraction of component α	—
Z_{ice}	Ice table depth	m

Greek symbols

α_S	Solar absorptivity of the surface	—
α_{T_α}	Thermal diffusion factor	—
α_α	Polarizability of species α	\AA^3
δ	Kronecker delta	—
δ_0	Mars obliquity of rotation axis	$^\circ$
δ_s	Solar declination angle	$^\circ$
ϵ	Potential well depth	J
ϵ	Emissivity	—
ϵ_h^d	Discretization error	—
Γ_e	Effective thermal diffusivity	m^2/s
Γ_φ	Diffusion coefficient of φ	m^2/s

LIST OF FIGURES

γ_h	Hour angle	°
κ	Dilatational viscosity	Pa s
λ	Mean free path	μm
μ	Dynamic viscosity	Pa s
ν_α	Dipole moment of species α	debye
Ω^*	Reduced collision integral	—
ω_α	Mass fraction of component α	—
Φ_e	Exact solution of the differential equations	—
ϕ	Volume porosity	—
ϕ_L	Latitude	°
φ	Conserved quantity per unit mass	—
φ_h	Exact solution of the discretized equations on grid h	—
ρ	Mixture density	kg/m^3
ρ_{ice}	Density of ice	kg/m^3
ρ_α	Mass concentration of component α	kg/m^3
$\hat{\rho}_\alpha$	Thermodynamic density of component α	kg/m^3
σ	Collision diameter	Å
Θ_z	Solar zenith angle	°
$\boldsymbol{\tau}$	Viscous stress tensor	$\text{kg}/\text{m s}^2$
τ	Tortuosity factor	—

1

Introduction

One of the highly debatable philosophical issues today is the question “Are we alone in the universe? ” Mars, being the closest planet to Earth, has played host to a number of interplanetary missions. Liquid water, being one of the precursors to life, is a typical substance sought out during these missions. The Martian atmosphere is composed mainly of CO₂ (95.32%) with traces of H₂O (0.03%) [3]. Recently, during the Phoenix Mars lander mission, atmospheric temperatures and total pressures were found to be in the range of 180 - 250 K and 720 - 860 Pa, respectively. In addition, the partial pressure of the water vapour in the atmosphere was found to be 1.8 Pa during the day and decreased to about 10⁻² Pa during the night [4]. From these observations, it can be concluded that CO₂ is not expected to have changed phase during the mission.

The water, however, is expected to be in either a gaseous or solid state in the atmosphere. There may also be the possibility for water to exist in a liquid state, when considering the subsurface of the Martian regolith [5–7]. Soil measurements from the Phoenix mission show substantial amounts of magnesium perchlorate [8], which when mixed with water molecules lowers the melting point down to $-68\text{ }^{\circ}\text{C}$ [9]. Because soil and ice co-exist in the regolith, it is hypothesized that, under favourable conditions, ice could melt forming water-salt systems [6]. Additional sources of liquid water could result from melting of early morning frost from surrounding areas. Such permanent melting-freezing cycle could contribute to more frequent heat and water exchange and could cause numerous physical, chemical and possibly biological processes.

1.1 The Phoenix Mission

The Phoenix Mars Lander touched down on the Green Valley of Vastitas Borealis on May 25, 2008, in the early Martian northern hemisphere’s summer, where the solar longitude L_S (the seasonal index) is about 78° . It operated successfully for 152 Martian solar days (sols, 1 sol \sim 24 h 40 min) spanning the peak of the annual water cycle and the beginning of ground frost formation. The objectives of the Phoenix mission were to study the history and current state of water there and to understand if the environment could support microbial life. To answer these questions, Phoenix’s instruments (as shown in Fig. 1.1) were suitable for analyzing samples of the soil and ice and monitoring the atmospheric conditions and phenomena.

The lander’s meteorological package (MET) [10] was equipped with wind, pressure and temperature sensors. The pressure sensor was located on the surface of the deck (\sim 1 m above the ground) and operated continuously, with a sampling rate of 0.5 hertz. It was designed to measure over the range of 700 - 1100 Pa with an accuracy of 10 Pa and a resolution of 0.1 Pa. Three ther-

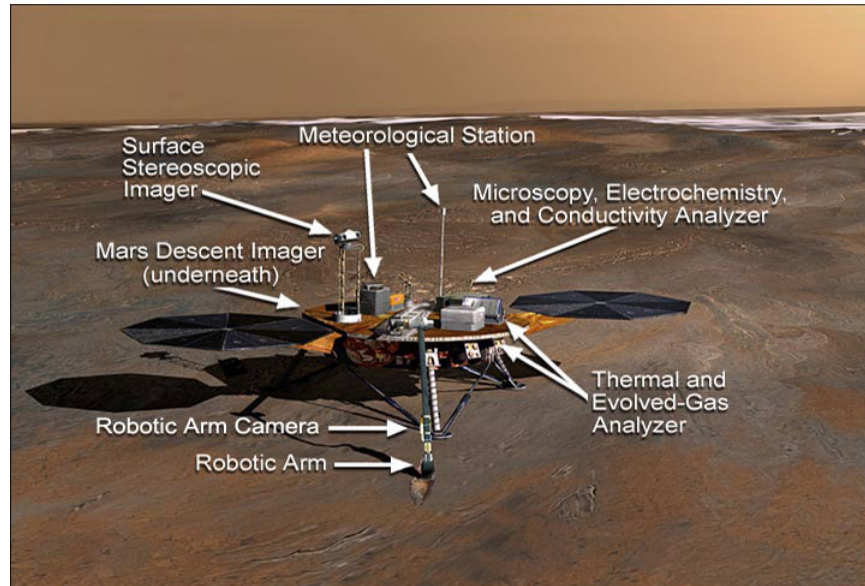


Figure 1.1: *Instruments on Phoenix Mars Lander. Image credit: NASA/JPL-Caltech/UA/Lockheed Martin.*

mocouples were mounted on a 1 m vertical mast at heights of 250, 500 and 1000 mm above the lander's deck. These sensors had a sampling rate of 0.5 Hz with an absolute accuracy of ± 1 K and a resolution of 0.5 K. Wind speed and direction were determined from images taken of the Telltale wind sensor by the stereo camera. The wind speed was based on the amount of deflection of the foil cylinder (Telltale) from the rest position, while the wind direction was inferred by which way this deflection occurred. The wind sensor was mounted on the top of the meteorological mast about 2 m above the ground. The accuracy of such measurement was estimated to be ± 1 m s⁻¹ in the range 2 - 5 m s⁻¹ and ± 2 m s⁻¹ in the range 5 - 10 m s⁻¹ [10]. The MET also contained a LIDAR (light detection and ranging device) which measured a vertical profile of the amount of dust and water ice clouds in the atmosphere. It operated at wavelengths of 1064 and 532 nm and was capable of detecting a cloud with optical thickness as low as 0.05 up to 20 km above the lander's deck [11]. Its one limitation was that the measurements were not possible below

200 m due to the transmitter-receiver overlap geometry [12]. However, it was possible to determine the altitude distribution of water-ice particles close to the surface by imaging the path of the LIDAR beam with the Surface Stereo Imager (SSI) [13]. The SSI, which was a high resolution camera, was capable of measuring atmospheric opacity and particle scattering, and sat on a platform near the base of the Robotic Arm (RA). The camera’s optical performance and multispectral capabilities were similar to the Pancam camera in the Mars Exploration Rover’s mission [14]. The soil temperature and heat transfer characteristics were provided by a Thermal and Electrical Conductivity Probe (TECP) [15]. The TECP was mounted near the end of the Robotic Arm and had four short, dual-probe sensors to perform six following measurements: the temperature of the Martian regolith with 2 K precision and an accuracy of $\pm 10\%$, the soil thermal conductivity with 10% accuracy, the volumetric heat capacity with 10% accuracy and the water vapour pressure with $\pm 10\%$ accuracy. The summary of the measurements from the Phoenix Mars Mission is given in Table 1.1.

Property	Measurements
Atmospheric temperature	193 - 243 K
Atmospheric pressure	720 - 860 Pa
Surface temperature	181 - 253 K
Thermal conductivity of the soil	0.03 - 0.14 W m ⁻¹ K ⁻¹
Volumetric heat capacity of the soil	0.5×10 ⁶ - 1.5×10 ⁶ J m ⁻³ K ⁻¹
Wind speed	1 - 12 m s ⁻¹
Water vapour pressure	0.05 - 1.8 Pa

Table 1.1: *Properties summary at the Phoenix landing site.*

Over the course of the mission, atmospheric pressure was found to be in the range of 720 - 860 Pa [16]. Atmospheric temperatures at ~ 2 m above the surface typically range from 193 K at night to 243 K in early afternoon [17]. The temperatures near the surface were found to be colder than those measured at 2 m and ranged from 253 K to 181 K. The overall average thermal conductivity of the soil was measured to be $0.085 \text{ W m}^{-1} \text{ K}^{-1}$ and the average volumetric heat capacity was found to be $\sim 1.05 \times 10^6 \text{ J m}^{-3} \text{ K}^{-1}$ [4]. Wind speeds ranged from 1 to 12 m s^{-1} [18]. Observations of the Phoenix landing site from the Meteorological Station (MET) indicate that the typical mid-sol relative humidity was about 5%. The daily maximum water vapour pressure measured by TECP was $\sim 1.8 \text{ Pa}$ at 5 cm above the surface. During the night, the vapour pressure dropped below 0.1 Pa [4]. The Lidar and SSI surface images of frost and fog [12], consistent with high relative humidity, suggest saturation of the near-surface atmosphere, while the sun was set. Systematic increase of regolith dielectric permittivity over the night indicated that the soil was accumulating water at night [4].

1.2 Water Cycle Study at the Surface of Mars

Empirical data on Mars collected from orbiters, landers, and telescopes is extensive enough to debate about the possibility of life there. Although the Phoenix mission found no evidence of life on the Martian surface, there is sufficient evidence that there was liquid water on the surface of the planet early in its history. Images from the Mars Global Surveyor and Odyssey show evidence of features such as dry riverbeds, lakes and deltas, gullies and large outflow channels [19]. The Mars Exploration Rover mission has discovered a water-altered mineral [20], known as hematite, and is often found in hot springs on Earth. The OMEGA/Mars Express has identified hydrated sulfates in the regolith [21, 22], which are thought to be left behind after water evaporated

from lakes or seas. Recently, the Phoenix Lander has analyzed surface samples and found that the soil contains carbonates [23]. Carbonates usually form through aqueous processes [24] and may suggest liquid water activity on Mars. Additionally, there may be occasional liquid water on the surface today when considering the subsurface of the Martian regolith [5–7]. Soil measurements from the Phoenix mission show substantial amounts of magnesium perchlorate [8], which when mixed with water molecules lowers its melting point down to $-68\text{ }^{\circ}\text{C}$ [9]. Because soil and ice co-exist in the regolith, it is hypothesized that, under favourable conditions, ice could melt forming water-salt systems [6]. An understanding of water transport mechanism is then the key to liquid water. Furthermore, the presence of liquid water on a planet naturally represents a potential habitat for life as well as a main water resource for future human exploration.

Study of the water transport on Mars has been a topic of research since water vapour was first detected in the Martian atmosphere [25]. This has led to multiple theories about the existence of water on Mars, the states it exists in, and its daily and seasonal cycle. In order to understand the water cycle on Mars, the details of the gas transport between the surface and the atmosphere is of importance. While spacecraft exploration cannot provide all of the relevant details for the surface-atmosphere water exchange, numerical models can reproduce the observations and show much more detail. The ability of these models to reproduce realistic conditions on Mars depends on the number of physical processes included in the model. There is no model, so far, that has taken into account all of the physical processes relevant for the water cycle on Mars at once. It is known, however, that the vapour amount near the surface can simultaneously vary by surface frost deposition/sublimation, surface fog formation/dissipation, horizontal and vertical transport and vapour flux into and out of the soil. Additionally, it has been observed that processes other than those stated previously take water vapour out of the atmosphere. Analyzing TECP results from the Phoenix mission Zent et al. [4] reported that the

reduction in atmospheric vapour content begins during the early evening, when the ground and air temperatures are well above the frost point. The inference is that either thermal diffusion or adsorption in the regolith is controlling a local H₂O. Answering these questions would give better insight into conditions favourable for liquid water to exist and would assist in the prediction of the future climate development on Mars.

Different modelling studies of water cycle on Mars have been performed in the past with the first dating back to the late 1970s [26–28]. The fog has been first studied by Ryan et al. [29]. They believed that the fog is responsible for the observed temperature inflection in the Martian data. Although, the inflection produced by their model was much weaker than inflections appearing in the Viking measurements, they were able to calculate how much water must be present in the atmosphere and to determine the frost point temperature within 2 °C. Later, Savijärvi [30] simulated Martian fog in the atmosphere using one-dimensional mesoscale model. The model produced a thin fog with mixing ratios of up to 2.5 g kg⁻¹. The model of Savijärvi [30] was next adapted by Möhlmann et al. [31] to verify that there are conditions in the near-surface atmosphere of Mars, which can be in favour of fog formation. Their results indicate that such conditions can develop on Mars, but better understanding of this phenomena is still needed.

A good summary of the seasonal water cycle is given by Jakosky and Haberle [32]. They concluded that sublimation and deposition of water can occur on Mars, but the amount was still very uncertain. Similarly, they stated that much of the water must be coming from the regolith, therefore, the water becomes more concentrated near the surface. Consequently, the later models [30, 33, 34] include the mass transport in the regolith. In most cases, the results show that the flux through the Martian surface reverses twice in the course of each sol, suggesting that the regolith plays a significant role in controlling the atmospheric water column abundance. Since these models use a very coarse

grid (e.g., the model of Savijärvi [30] has only 20 layers in the vertical direction from the surface up to 20 km), they can not realistically simulate near surface conditions. Similarly, the High Resolution Limited Area Models (HIRLAM) (e.g., Toigo et al. [35], Wing and Austin [36], Kauhanen et al. [37], Savijärvi and Määttänen [38]), which are used mostly as operational weather prediction models, cannot sufficiently capture rapid variations in the regolith. Their value is more in providing local weather conditions for the lander and rover missions rather than simulating small scale transport phenomena. Subtle or dramatic modifications in the spatial distribution of water can occur at very small-scale (cm to m). A typical resolution used in the previous models is still inadequate for incorporating many regionally and locally important processes. With much higher resolution there is the possibility to simulate “new” phenomena, which are averaged out in the previous models. Additionally, most of these models are one-dimensional and do not include effects of the local topography, which are important since the quantity of water vapour, in the atmosphere and regolith, has a spatio-temporal variation. Furthermore, there are spatial variations in the depth of the ice table and thickness of the regolith, as well as in salt content of the permafrost. All of the above suggest that a multi-dimensional, high resolution model is critical.

There is no multi-dimensional model so far that has been able to consider diurnal water vapour cycle at the surface of Mars, including frost or fog formation in the atmosphere and the regolith. Although, three-dimensional models have been developed in the past (e.g., Houben et al. [39]), they do not include surface topography and there is no diurnal cycle. It is also surprising that there is no model so far that accounts for the effect of thermal diffusion in the regolith. For the surface of Mars, where great daily fluctuations in thermal gradients occur ($\Delta T/z \sim 10^3 \text{ K m}^{-1}$), thermodiffusion of water vapour may play an important role in daily water cycle. Mellon and Jakosky [40] calculated the magnitude of thermal diffusion to be only about 1.5% that of Fickian diffusion and they simply neglected it in their model. For similar reason, the thermod-

CHAPTER 1: INTRODUCTION

iffusion was neglected in the model of Schorghofer and Aharonson [41]. Later, Hudson et al. [42] stated that thermodiffusion contributes noticeably to vapour transport on Mars, but neglected it as the others.

The goal of this research is to develop a fully functional, multi-dimensional model with source terms that account for the mass and heat transfer between the gaseous and solid phases of water. The model will help in understanding the mechanism of H₂O exchange between the atmosphere and the regolith of Mars. It will differ from the others by use of appropriate meteorological data transmitted from the Phoenix lander and highly detailed, multi-dimensional modelling of sublimation/deposition in the regolith and near atmosphere. Additionally, the effect of thermal diffusion in the regolith, which has not been studied yet for Mars, will be considered. The model will be tested with available data from the Mars Phoenix mission for possible uses in modelling and interpretation of orbital data far from the Phoenix site.

2

Theory

The present study is concerned with the modelling of the water vapour transport mechanism in the atmosphere and regolith of Mars using a multicomponent flow with heat and mass transfer. In this chapter, the equations that govern the fog formation in the atmosphere using both the Fickian and the thermal diffusion of gases in the regolith are derived. An additional correction is developed to include the effects of the porous medium on the diffusion coefficient and a simple surface radiation model is used to predict the net energy flux into the ground.

2.1 Water Vapour and Ice Transport in the Martian Atmosphere

The Martian atmosphere is composed mainly of carbon dioxide (95.32%) with traces of nitrogen (2.7%), argon (1.6%), oxygen (0.13%), carbon monoxide (0.07%), water vapour (0.03%), and nitric oxide (0.013%) [3]. Recently, during the Phoenix Mars lander mission, atmospheric temperatures and total pressures were found to be in the range of 180 - 250 K and 720 - 860 Pa, respectively (as shown in Fig. 2.1). Due to the very low pressures and the

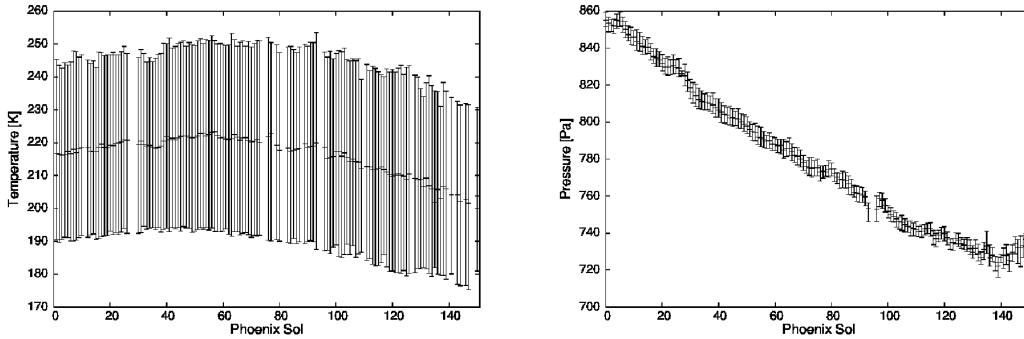


Figure 2.1: Plot showing the minimum, maximum, and average temperature (left) and the total pressure (right) measured during the Phoenix mission.

moderate temperatures, the Martian atmosphere is assumed to be a mixture of ideal gases: CO_2 and H_2O . Generally, deviation from an ideal gas tends to decrease with lower density (i.e., lower pressure) [43]. With information on the temperatures and pressures, the density is estimated using the ideal gas law

$$\rho = \frac{M_w P}{RT} \quad (2.1.1)$$

where M_w is the molar mass and $R=8314.5 \text{ J K}^{-1} \text{ kmol}^{-1}$ is the universal gas constant. The above equation of state applies only to an ideal gas and fails when intermolecular forces and molecular size become important. At Mars conditions (i.e., low pressure and moderate temperatures), the average dis-

tance between adjacent molecules is much larger than the molecular size and some heavier gases (e.g., CO₂) can be treated like ideal gases with negligible error [44]. The model of an ideal gas, however, is extremely inaccurate when modelling phase transition. These must be modelled by more accurate equations of state.

The properties of mixture of ideal gases can be calculated directly from the properties of the components and their proportions in the mixture. The two commonly used models for finding these properties are: the Amagat and the Dalton models [45]. The former states that the volume occupied by a gas mixture is equal to the sum of the volumes that the pure components would occupy at the same pressure and temperature. The later, however, states that the total pressure exerted by the mixture gases is equal to the sum of the pressure exerted by its components. By combining the results of the Amagat and Dalton models, it can be shown that, for ideal gas mixtures the partial pressure of the component is equal to the product of the mole fraction of the component and the mixture pressure. Moreover, the volume fraction and the mole fraction of a component in an ideal gas mixture are the same. Therefore, Amagat's law and Dalton's law are equivalent to each other if the gases and the mixture are ideal gases.

$$\frac{P_\alpha}{P} = \frac{V_\alpha}{V} = \frac{N_\alpha}{N} = x_\alpha \quad (2.1.2)$$

Here P_α is the partial pressure of component α , P is the mixture pressure, V_α is the partial volume of component α , V is the mixture volume, N_α is the partial molecular concentration of component α , N is the total number of molecules of all components per unit volume and x_α is the mole fraction of component α . The full derivation of this equation is found in [A.1](#).

In this work, the mixture density, ρ , is calculated based on the law of additive volumes. Thus, the partial volumes of all components must sum to the total

volume

$$V = \sum_{\alpha=1}^n V_{\alpha} \quad (2.1.3)$$

If the mass of component α , present in this volume is m_{α} , then the concentration of component α is

$$\rho_{\alpha} = \frac{m_{\alpha}}{V} \quad (2.1.4)$$

The partial volume of component α would be the volume occupied by the same mass of the component at the same local temperature and pressure as the mixture. In this case, the density of the component can be evaluated from the equation of state at the mixture temperature and pressure. Such density is also known as the thermodynamic density and may be expressed as

$$\hat{\rho}_{\alpha} = \frac{m_{\alpha}}{V_{\alpha}} \quad (2.1.5)$$

Using the above relations with the Amagat's law, it follows that

$$1 = \sum_{\alpha=1}^n \frac{V_{\alpha}}{V} = \sum_{\alpha=1}^n \frac{m_{\alpha}/\hat{\rho}_{\alpha}}{m_{\alpha}/\rho_{\alpha}} = \sum_{\alpha=1}^n \frac{\rho_{\alpha}}{\hat{\rho}_{\alpha}} = \sum_{\alpha=1}^n \frac{\rho\omega_{\alpha}}{\hat{\rho}_{\alpha}} \quad (2.1.6)$$

or

$$\frac{1}{\rho} = \sum_{\alpha=1}^n \frac{\omega_{\alpha}}{\hat{\rho}_{\alpha}} \quad (2.1.7)$$

where $\omega_{\alpha} = \rho_{\alpha}/\rho$ is the mass fraction of component α . The intensive properties of the mixture are calculated using a mass fraction weighted average

$$Z = \sum_{\alpha=1}^n \omega_{\alpha} Z_{\alpha} \quad (2.1.8)$$

where Z_{α} is the property value for component α . Here, Eqn. 2.1.8 is used to calculate the specific heat of the mixture c_p , the mixture dynamic viscosity μ and the mixture thermal conductivity k . It should be noted that, the above linear mixture rule may lead to large overestimates when calculating the last two properties. Fig. 2.2 shows the viscosity and thermal conductivity of the mixture of CO₂ and H₂O plotted as a function of x_{H_2O} at constant temperature (i.e., 293 K). The straight lines are based on the linear mixture rule (Eqn.

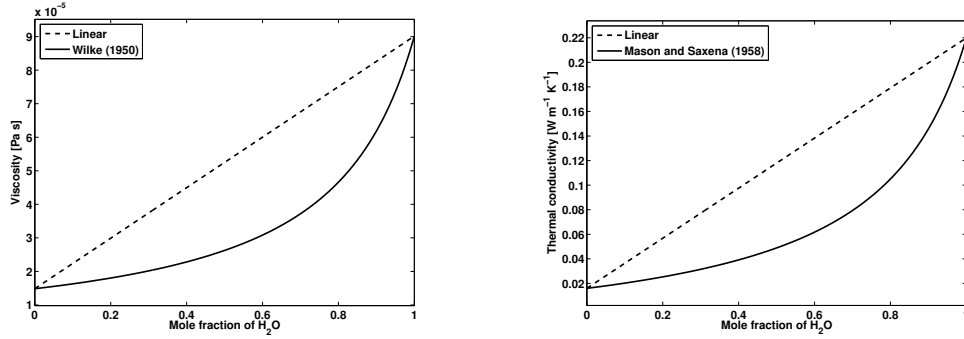


Figure 2.2: Comparison of mixture viscosity (left) and thermal conductivity (right) obeying the linear mixture rule (dashed lines) with those showing deviations (solid lines).

2.1.8) and the curved lines are calculated from more accurate formulas given in A.2. It is seen that dependence of mixture viscosity and thermal conductivity on composition is extremely nonlinear for mixture of CO₂ and H₂O, however the magnitude of the deviations is small when the fraction of any of the mixture components is very small ($x_{H_2O} \ll x_{CO_2}$ or $x_{CO_2} \ll x_{H_2O}$). Since on Mars $x_{H_2O} \ll x_{CO_2}$, the linear mixture rule will not introduce a significant error when calculating μ and k .

Transport properties of pure components are functions of temperature and pressure and can be obtained from various formulas found in the literature [45–49]. They may be also determined based on the kinetic theory of gases and liquids [50–52]. In this work, the properties of pure components were imported from the material library available in ANSYS CFX 13.0 code.

2.1.1 Governing Equations

In a multicomponent fluid the various components are mixed at the molecular level and will share the same mean velocity, pressure and temperature fields. The total mass is equal to the sum of the individual masses m_α , i.e.,

$m = \sum m_\alpha$. Therefore, using Eqn. 2.1.4, it follows that the mixture density must be the sum of concentrations of all the individual components

$$\rho = \sum_{\alpha=1}^n \rho_\alpha \quad (2.1.9)$$

The governing equations for a general, non-isothermal, multicomponent fluid are [50]:

- The conservation of mass for a mixture

$$\frac{D\rho}{Dt} + \rho(\nabla \cdot \mathbf{v}) = 0 \quad (2.1.10)$$

where $\mathbf{v} = (u, v, w)$ is the velocity of gas mixture defined for a multicomponent mixture as

$$\mathbf{v} = \frac{\sum_{\alpha=1}^n \rho_\alpha \mathbf{v}_\alpha}{\sum_{\alpha=1}^n \rho_\alpha} = \frac{\sum_{\alpha=1}^n \rho_\alpha \mathbf{v}_\alpha}{\rho} \quad (2.1.11)$$

where \mathbf{v}_α is the velocity of species α . The first term on the left side of Eqn. 2.1.10 is the total or material derivative of ρ with respect to time and is defined as

$$\frac{D\rho}{Dt} = \frac{\partial \rho}{\partial t} + \mathbf{v} \cdot \nabla \rho \quad (2.1.12)$$

- The conservation of mass for a pure component α

$$\frac{\partial \rho_\alpha}{\partial t} + \nabla \cdot (\rho_\alpha \mathbf{v} + \mathbf{j}_\alpha) = r_\alpha \quad (2.1.13)$$

where r_α is the component source/sink term, and \mathbf{j}_α is the diffusive flux of component α . Note that n species conservation equations (Eqn. 2.1.13) and the total mass conservation equation (Eqn. 2.1.10) are linearly dependent. Therefore, only $n - 1$ species equations and the total mass conservation equation are solved using $(\rho, \rho_\alpha, \rho_\beta, \dots, \rho_{n-1})$. ρ_n is evaluated from Eqn. 2.1.9.

- The momentum equation for the mixture

$$\rho \frac{D\mathbf{v}}{Dt} + \nabla P + \nabla \cdot \boldsymbol{\tau} - \rho \mathbf{g} + S_M = 0 \quad (2.1.14)$$

where \mathbf{g} is the gravity vector acting in the negative z direction, S_M represents other momentum sources and $\boldsymbol{\tau}$ is the stress tensor defined as

$$\boldsymbol{\tau} = -\mu \left[\nabla \mathbf{v} + (\nabla \mathbf{v})^T \right] + \left(\frac{2}{3}\mu - \kappa \right) (\nabla \cdot \mathbf{v}) \delta \quad (2.1.15)$$

where κ is dilatational viscosity, and δ is the unit tensor.

- The thermal energy equation

$$\rho \frac{Dh}{Dt} + (\nabla \cdot \mathbf{q}) + (\boldsymbol{\tau} : \nabla \mathbf{v}) - \frac{DP}{Dt} + S_E = 0 \quad (2.1.16)$$

where h is the specific enthalpy, S_E is an optional volumetric energy source and \mathbf{q} is the heat flux vector defined as

$$\mathbf{q} = -k \nabla T + \sum_{\alpha=1}^n \frac{h_\alpha}{M_{w_\alpha}} \mathbf{j}_\alpha \quad (2.1.17)$$

Here the quantity h_α is the partial molar enthalpy and T is the temperature. The derivation of Eqn. 2.1.16 is given in A.3. There is no need for a particular definition of enthalpy, since only changes in enthalpy are calculated. The thermal energy equation is transformed into a governing equation for the temperature by replacing the enthalpy with the general differential relationship

$$dh = \left(\frac{\partial h}{\partial T} \right)_p dT + \left(\frac{\partial h}{\partial p} \right)_T dp \quad (2.1.18)$$

which for ideal gases reduces to

$$dh = c_p dT \quad (2.1.19)$$

where c_p is the specific heat at constant pressure.

2.1.2 Simplified Equations for the Atmosphere

Local atmospheric phenomena are modelled using a laminar flow assumption. The simulated part of the diurnal period will be restricted to the evening and night, when the laminar flow assumption for the wind is reasonable.

For an incompressible flow, the mass conservation equation (Eqn. 2.1.10) becomes

$$\nabla \cdot \mathbf{v} = 0 \quad (2.1.20)$$

The conservation of mass for a single component α (Eqn. 2.1.13), written in terms of mass fraction (Eqn. 2.1.7), is

$$\rho \left(\frac{\partial \omega_\alpha}{\partial t} + \mathbf{v} \cdot \nabla \omega_\alpha \right) = -\nabla \cdot \mathbf{j}_\alpha + r_\alpha \quad (2.1.21)$$

For the case of a two-component mixture, Fick's law of mass diffusion is

$$\mathbf{j}_\alpha = -\rho D_{\alpha\beta} \nabla \omega_\alpha \quad (2.1.22)$$

where $D_{\alpha\beta}$ is the diffusivity of the component α in β . For an incompressible flow with a constant diffusivity $D_{\alpha\beta}$, Eqn. 2.1.21 becomes, after inserting Fick's law

$$\frac{\partial \omega_\alpha}{\partial t} + \mathbf{v} \cdot \nabla \omega_\alpha = D_{\alpha\beta} \nabla^2 \omega_\alpha + r_\alpha \quad (2.1.23)$$

Next, the viscous stress tensor in the momentum equation (Eqn. 2.1.15) reduces to

$$\boldsymbol{\tau} = -\mu \left[\nabla \mathbf{v} + (\nabla \mathbf{v})^T \right] \quad (2.1.24)$$

which then replaced into the momentum equation (Eqn. 2.1.14) gives

$$\rho \left[\frac{\partial \mathbf{v}}{\partial t} + (\mathbf{v} \cdot \nabla) \mathbf{v} \right] = -\nabla P + \nabla \cdot \left\{ \mu \left[\nabla \mathbf{v} + (\nabla \mathbf{v})^T \right] \right\} + \rho \mathbf{g} + S_M \quad (2.1.25)$$

In the presence of the gravitational force and density gradients, natural convective motion may be created due to the buoyancy forces. The buoyancy forces arises due to the difference in hydrostatic pressure gradient, which is proportional to the local density in a fluid ($\nabla P = -\rho \mathbf{g}$). If this pressure gradient

arises from gravity, then the dominant driving force of the flow is the term $(\rho - \rho_{ref}) \mathbf{g}$, where ρ_{ref} is a reference density in a bulk fluid. For buoyancy calculations, this term is added to the momentum equation as follows

$$\rho \left[\frac{\partial \mathbf{v}}{\partial t} + (\mathbf{v} \cdot \nabla) \mathbf{v} \right] = -\nabla P + \nabla \cdot \left\{ \mu \left[\nabla \mathbf{v} + (\nabla \mathbf{v})^T \right] \right\} + \mathbf{g}(\rho - \rho_{ref}) \quad (2.1.26)$$

The energy equation is solved using the specific enthalpy formulation. Since the temperature rise due to the viscous dissipation heating is small for low viscous fluids, $(\boldsymbol{\tau} : \nabla \mathbf{v})$ is neglected and Eqns. 2.1.16 to 2.1.19 reduce to

$$\rho c_p \left[\frac{\partial T}{\partial t} + (\mathbf{v} \cdot \nabla) T \right] = \nabla \cdot \left(k \nabla T - \sum_{\alpha=1}^n \frac{h_{\alpha}}{M_{w_{\alpha}}} \mathbf{j}_{\alpha} \right) + S_E \quad (2.1.27)$$

where at low velocities, the term $\frac{DP}{Dt}$ is assumed to be small compared to other terms, and it is also neglected.

2.1.3 Sublimation/Deposition Source Term

During the Phoenix Mars lander mission, the partial pressure of the water vapour in the atmosphere was found to be 1.8 Pa during the day and decreased to 1×10^{-2} Pa at night [4]. From these observations, it is taken that the CO_2 gas in the atmosphere did not change phase during the mission. The H_2O , however, is expected to exist in either a gaseous or solid state in the atmosphere depending on its ω (as shown in Fig. 2.3). The other components of the Martian atmosphere are too small and are neglected in this study. When the atmosphere is saturated, the partial pressure of water vapour is equal to the saturation pressure of water at the gas temperature. The temperature at which the saturation is reached, is called the frost point temperature. This comes from the fact that, if the atmosphere cools below this temperature, some of the water vapour initially present will condense, forming frost or fog. Any additional cooling should decrease the partial pressure and force the atmospheric water vapour to condense. Because of the low temperature

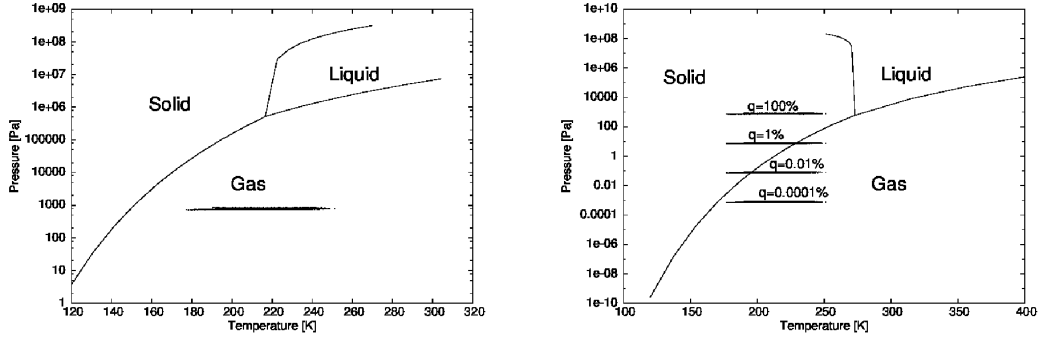


Figure 2.3: Plot showing the phase diagrams for CO_2 (left) and H_2O (right) [1, 2].

and pressure of the atmosphere, the water vapour sublimates directly into ice (deposition). The deposition rate, which is driven by a temperature gradient, is defined as the difference between the local water vapour density $\rho_{\text{H}_2\text{O}}^G$ and the saturation water vapour density $\rho_{\text{H}_2\text{O}sat}^G$. Thus, the source term for water mass balance is considered as

$$r_{\text{H}_2\text{O}}^G = \frac{1}{\Delta t} [\rho_{\text{H}_2\text{O}sat}^G(T, P_{\text{H}_2\text{O}sat}^G) - \rho_{\text{H}_2\text{O}}^G(T, P_{\text{H}_2\text{O}}^G)] \quad (2.1.28)$$

The equation used to calculate the saturation pressure, P_{sat} from which the saturation concentration is determined, is reported by Buck [53]

$$P_{sat}(T) = 611.35 \cdot \exp\left(\frac{22.542(T - 273.16)}{T + 0.32}\right) \quad (2.1.29)$$

The phase change process requires the energy transport between the species. The amount of heat required to change the phase of a fixed amount of a substance is known as latent heat. The source term for the energy equation (Eqn. 2.1.27), representing the latent heat, is written as

$$S_E = \frac{1}{\Delta t} [\rho_{\text{H}_2\text{O}sat}^G(T, P_{\text{H}_2\text{O}sat}^G) - \rho_{\text{H}_2\text{O}}^G(T, P_{\text{H}_2\text{O}}^G)] h_{GS} \quad (2.1.30)$$

where, h_{GS} is the specific latent heat of phase change from vapour to solid. h_{GS} is a function of temperature only and it varies from 2824 kJ kg⁻¹ for -100°C to 2834 kJ kg⁻¹ for 0°C [54]. For typical frost point temperatures on Mars, the latent heat of sublimation is approximately 2830 kJ kg⁻¹.

2.1.4 Moist Parametrization

To setup the boundary conditions properly, some additional atmospheric variables need to be defined. According to Dalton's law, in a mixture of ideal gases each gas can be assumed to behave as if the other gases were absent. Thus, for water vapour, the vapour pressure becomes

$$P_{H_2O} = \rho_{H_2O} R_{H_2O} T \quad (2.1.31)$$

where ρ_{H_2O} is the density and R_{H_2O} is the specific gas constant. Since the molecular weight of water is $M_{w_{H_2O}} = 18.01 \text{ kg kmol}^{-1}$, the value of R_{H_2O} is equal to

$$R_{H_2O} = \frac{R}{M_{w_{H_2O}}} = 461.5 \text{ J kg}^{-1} \text{ K}^{-1} \quad (2.1.32)$$

To measure a moisture content in the atmosphere, the specific humidity, q , and the mixing ratio, ω_r , are used. The former is defined as the number of grams of water vapour per unit mass of the atmosphere including water vapour, and is written as

$$q = \frac{\rho_{H_2O}}{\rho} = \frac{m_{H_2O}}{m} \quad (2.1.33)$$

Unlike the specific humidity, the mixing ratio is defined as the number of grams of water vapour per unit mass of dry atmosphere. Here, the atmosphere is assumed to be a mixture of CO_2 and H_2O , thus the mixing ratio is

$$w_r = \frac{\rho_{H_2O}}{\rho_{CO_2}} = \frac{m_{H_2O}}{m_{CO_2}} \quad (2.1.34)$$

Since

$$\frac{1}{q} = \frac{m_{CO_2} + m_{H_2O}}{m_{H_2O}} = \frac{m_{H_2O}}{m_{CO_2}} + 1 \quad (2.1.35)$$

it follows that

$$w_r = \frac{q}{1 - q} \quad (2.1.36)$$

or

$$q = \frac{w_r}{1 + w_r} \quad (2.1.37)$$

In the Martian atmosphere, both w_r and q are very small ($w_r, q \ll 1$) [55] and it follows that $w_r \approx q$. It should also be noted that in meteorology ρ_{H_2O} is often called the absolute humidity.

In literature (e.g., Whiteway et al. [55]), the volume mixing ratio is often used instead of the mass mixing ratio. The volume mixing ratio is defined as the number density of the gas (water vapour), N_{H_2O} , to the total number density of the atmosphere N

$$w_{r \text{ vol}} = \frac{N_{H_2O}}{N} = \frac{A_v \cdot c_{H_2O}}{A_v \cdot c} = \frac{c_{H_2O}}{c} = x_{H_2O} \quad (2.1.38)$$

where $A_v = 6.022 \times 10^{23} \text{ mol}^{-1}$ is the Avogadro's number and c is the molar concentration.

Another important parameter in numerical weather prediction is the relative humidity, RH , defined as

$$RH = \frac{P_{H_2O}}{P_{H_2O \text{ sat}}} \times 100\% \quad (2.1.39)$$

As it takes into account the variation in saturated vapour pressure, it is often preferable in modelling phase change over the absolute humidity. It provides information on how far the system is from the saturation point. For example, the atmosphere is said to be saturated when $RH = 100\%$. However, even a relative humidity of 100% might be not enough for condensation (or sublimation) to happen. Spontaneous condensation in the absence of nuclei needs extremely high relative humidity, which cannot easily occur in the atmosphere [56]. Field et al. [57] measured the threshold relative humidity over ice for nucleation onto desert dust to be in the range from 110 to 130%. Based on calculation for Pathfinder, Määttä et al. [58] reported the critical relative humidity for the nucleation of water onto dust to be 120%.

2.1.5 Binary Diffusion Coefficient

Many theoretical formulas have been suggested to calculate the binary diffusion coefficient. Most of them are based on the kinetic theory of gases, which can predict values of $D_{\alpha\beta}$ within about 6% [50]. In the first approximation [51] the result is

$$D_{\alpha\beta} = 0.002628 \frac{\sqrt{T^3 \frac{M_{w\alpha} + M_{w\beta}}{2M_{w\alpha}M_{w\beta}}}}{P \sigma_{\alpha\beta}^2 \Omega_{\alpha\beta}^{(1,1)} T_{\alpha\beta}^*} \quad (2.1.40)$$

The parameters $\sigma_{\alpha\beta}$, $\Omega_{\alpha\beta}^{(1,1)}$, and $T_{\alpha\beta}^*$ are known as the molecular potential parameters and are explained in section 2.2.3. Higher approximations to the coefficient of diffusion are given in Hirschfelder et al. [51], and are complex functions of the molecular weights, the mole fractions, the viscosities and of the temperature. There have been also several experimental measurements of the binary diffusion coefficient. For the mixture of H₂O-CO₂, the International Critical Tables [59] list the following correlation

$$D_{H_2O,CO_2} = 0.1387 \left[\frac{cm^2}{s} \right] \left(\frac{T}{273.15 [K]} \right)^2 \left(\frac{P_{ref}}{P} \right) \quad (2.1.41)$$

Marrero and Mason [60] recommend

$$D_{H_2O,CO_2} = 9.24 \times 10^{-5} \left[\frac{cm^2}{s} \right] T^{\frac{3}{2}} \exp\left(\frac{-307.9}{T}\right) \left(\frac{P_{ref}}{P} \right) \quad (2.1.42)$$

From the work of Wallace and Sagan [61], which is often cited in the context of Mars studies, the following correlation is suggested

$$D_{H_2O,CO_2} = 0.1654 \left[\frac{cm^2}{s} \right] \left(\frac{T}{273.15 [K]} \right)^{\frac{3}{2}} \left(\frac{P_{ref}}{P} \right) \quad (2.1.43)$$

Using a least squares fit method, Levin and Weatherwax [5] propose

$$D_{H_2O,CO_2} = 0.153 \left[\frac{cm^2}{s} \right] \left(\frac{T}{273.15 [K]} \right)^{1.5} \left(\frac{P_{ref}}{P} \right) \quad (2.1.44)$$

In all cases, $P_{ref} = 1013$ mbar.

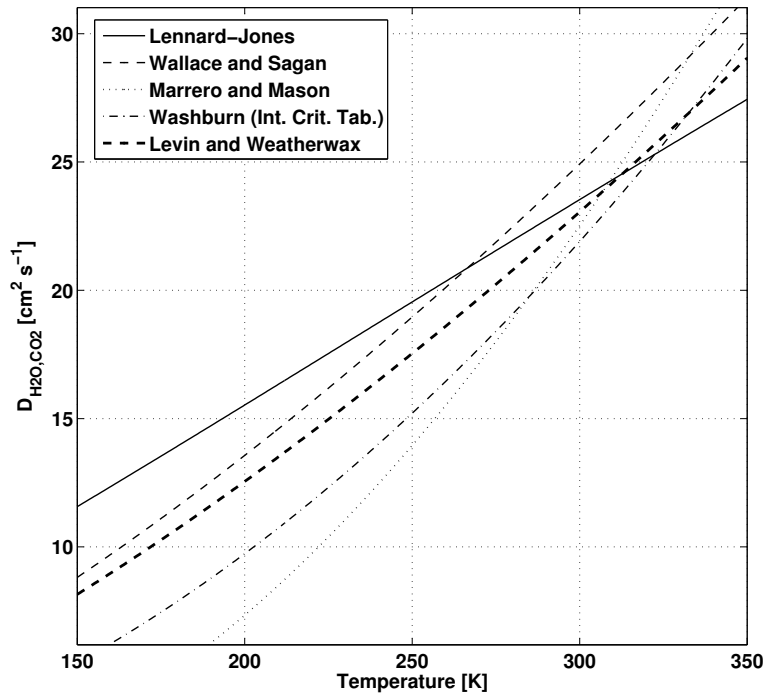


Figure 2.4: *The binary diffusion coefficient for H_2O in CO_2 as a function of temperature at 774 Pa.*

Fig. 2.4 shows theoretical values of the binary diffusion coefficient as a function of temperature. The curves calculated from the empirical fits (Eqns. 2.1.41 and 2.1.42), are based on measurements at high temperature and may not provide accurate results when extrapolated below 273 K. The theoretical formula for Lennard-Jones potential shows slightly higher values in the lower temperature range. The difference here is due to the first approximation in which the interactions between like pairs of molecules are ignored. In the higher approximations these forces are included. In this study, Eqn. 2.1.44 is used, as it seems to be an average of the others and has been used in previous water cycle studies on Mars.

To estimate the diffusion coefficient for ice particles in CO_2 , a mean free path

and particle diameters need to be known. From the images taken by the Compact Reconnaissance Imaging Spectrometer for Mars, in the early morning of Sol 70 of the Phoenix mission, the detected surface frost was determined to be of the order of 10 microns [62]. The mean free path, λ , of molecules in the Martian atmosphere is determined from the kinetic theory of gases using

$$\lambda = \frac{k_b T}{\sqrt{2} \pi \sigma^2 P} \quad (2.1.45)$$

where k_b is the Stefan-Boltzmann's constant and σ is the collision diameter of molecules. Here, σ for CO₂ gas is used ($\sigma_{CO_2}=3.996 \times 10^{-10}$ m [50]) since the Martian atmosphere is composed mainly of carbon dioxide. Next, the diffusion coefficient for H₂O ice is calculated using [63]

$$D_{ice,CO_2} = \frac{k_b T C_c}{3 \pi \mu d_{ice}} \quad (2.1.46)$$

where d_{ice} is the diameter of the ice particles and C_c is the Cunningham slip correction factor. According to Finlay [64], the Cunningham slip factor is a correction to the drag coefficient obtained with a continuum assumption and for $d_{ice} > 0.1 \mu\text{m}$, it is derived using

$$C_c = 1 + \frac{2.52 \lambda}{d_{ice}} \quad (2.1.47)$$

The dynamic molecular viscosity of CO₂ at constant low pressure is obtained from [45]

$$\mu = 11.336 + 0.49918 T - 1.0876 \cdot 10^{-4} T^2 \quad (2.1.48)$$

Therefore for CO₂ at 198 K, $\mu_{CO_2}=105.9 \times 10^{-7}$ Pa s. At that temperature and pressure of 774 Pa, the mean free path is $\sim 5 \mu\text{m}$, which gives $D_{ice,CO_2}=6 \times 10^{-12} \text{ m}^2 \text{ s}^{-1}$. This is more than 8 orders of magnitude smaller than the atmospheric diffusivities and can be safely omitted.

2.2 Water Vapour and Ice Transport in the Martian Regolith

The top layer of the Martian soil is made up of rock, ice and dust particles. This material is referred to as Regolith, a common planetary science term which refers to a layer of loose, unconsolidated material covering solid rock [65]. The Martian regolith is a major source and sink in the local and global water cycle on Mars. Gas transport in the upper part of the regolith influences the geographic distribution of water vapour and ice, and plays a key role in the diurnal and seasonal atmospheric water vapour content. Diffusion of water vapour in the sub-surface also controls the depth of the ice tables, which are found beneath the northern polar region of Mars. Every year a layer of frost is transported deep into the sub-surface where it accumulates and remains as a ground ice. The mean depth of such ice was found to be about 5 cm at the Phoenix site [66]. The upper layers of the regolith are dry because the large diurnal temperature oscillations lead to sublimation if any ice is present. The overall average thermal conductivity of the soil was measured to be $0.085 \text{ W m}^{-1} \text{ K}^{-1}$ [4]. The Phoenix Lander returned data showing the Martian soil to be made up mainly of silicates and iron oxides with smaller amounts of aluminium oxides, sulfates, magnesium oxides and calcium oxides along with other trace constituents [8, 23, 67]. The images from Optical Microscope (OM) show that by number, the dominant size consist of reddish fine-grained particles $< 10 \mu\text{m}$ across. A second size distribution of different origin includes magnetic particles in range from 20 to 100 μm . In terms of soil mass, 20% is in the reddish small particles and the other 80% in the larger particles [24]. In this work, the soil is modelled as a mixture of bulk basalt and hematite. Basalt is made up of dark coloured particles, similar to those from OM images. It is fine-grained and contains more than 50% of silica, $\sim 14\%$ of alumina, $\sim 10\%$ of magnesia and 5-12% of calcium oxide. The oxides are modelled as hematite, the mineral form of iron oxide which are responsible

for the red colour of the Martian soil. The mass fraction of hematite at the Phoenix landing site was found to be 0.2 [68]. Assuming the average volumetric heat capacity c_v of $\sim 1.05 \times 10^6 \text{ J m}^{-3} \text{ K}^{-1}$, the porosity, ϕ , accessible to flow is estimated from

$$c_v = \phi_s \rho_s c_{p_s} \quad (2.2.1)$$

where

$$\phi = 1 - \phi_s \quad (2.2.2)$$

and ϕ_s is the fraction of volume occupied by solid particles to the total volume.

Taking the density of the bulk basalt as 3011 kg m^{-3} [69], the density of bulk hematite as 5260 kg m^{-3} [70], and using Eqn. 2.1.7, it follows that the average density of the solid particles is 3293 kg m^{-3} . Next, the specific heat capacity of the basalt is found from Wechsler and Glaser [71] and for hematite from Grønvold and Westrum [72]. The average specific heat capacity of solid material is

$$c_{p_s} = \left[\frac{0.8}{879} + \frac{0.2}{511} \right]^{-1} \cong 768 \text{ J kg}^{-1} \text{ K}^{-1} \quad (2.2.3)$$

which results from equations 2.2.1 and 2.2.2 in a porosity $\phi = 0.58$. Using mercury porosimetry, Sizemore and Mellon [73] measured the porosity of JSC Mars-1 material, a widely used Martian regolith simulant, to be 0.65. This helps confirm the estimated porosity value.

The thermal conductivity of dry regolith is calculated based on the volumetric heat capacity and average thermal inertia calculated by Zent et al. [4] in accordance with the TECP findings

$$k_{dry} = \frac{I^2}{c_v (1 - \phi)} = \frac{280^2}{3293 \cdot 768 (1 - 0.58)} = 0.074 \text{ W m}^{-1} \text{ K}^{-1} \quad (2.2.4)$$

The thermal inertia, I , is a measure of the subsurface's ability to store heat during the day and re-radiate it during the night. Materials with higher thermal inertia need more time to heat up during the day and to cool off at night.

If the local atmospheric vapour density exceeds the pore-space vapour, water vapour will diffuse into the soil and ice will accumulate in the pore-space. This will influence the physical parameters of the soil. The effective porosity, which includes ice filled fraction of pores, V_{ice}/V_{void} , is then given by

$$\phi_{eff} = \phi_o \left(1 - \frac{V_{ice}}{V_{void}} \right) \quad (2.2.5)$$

where ϕ_o is porosity of an ice free regolith. The volumetric heat capacity of a soil of porosity ϕ , containing ice, may be closely approximated by

$$\rho c_p = \phi_s \rho_s c_{p_s} + \phi \left[\frac{V_{ice}}{V_{void}} \rho_{ice} c_{p_{ice}} + \left(1 - \frac{V_{ice}}{V_{void}} \right) \rho_{atm} c_{p_{atm}} \right] \quad (2.2.6)$$

where c_{p_s} , $c_{p_{ice}}$, and $c_{p_{atm}}$ and ρ_s , ρ_{ice} , and ρ_{atm} are the specific heats and densities of the soil, ice, and gas phase, respectively. Finally, the effective thermal

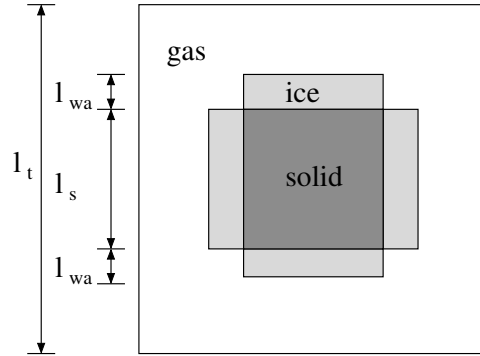


Figure 2.5: Cubic cell model for a soil with ice accumulated around the solid particle.

conductivity of an icy regolith can be estimated based on the theoretical model proposed by Gori and Corasaniti [74] (Fig. 2.5)

$$\begin{aligned} \frac{1}{k_{eff}} &= \frac{\beta - 1 - \frac{\gamma_i}{3}}{\beta k_{atm}} + \frac{\beta \gamma_i}{3 [k_{atm} ((\beta^2 - 1) + k_{ice})]} \\ &+ \frac{\beta}{k_s + \frac{2}{3} \gamma_i k_{ice} + k_{atm} (\beta^2 - 1 - \frac{2}{3} \gamma_i)} \end{aligned} \quad (2.2.7)$$

where k_{ice} and k_{atm} are the thermal conductivities of the ice and gas phase, respectively, β is defined as (Fig. 2.5)

$$\beta = \frac{l_t}{l_s} = \sqrt[3]{\frac{\rho_s}{\rho_{dry}}} = \sqrt[3]{\frac{1}{1-\phi}} \quad (2.2.8)$$

and γ_i is given by

$$\gamma_i = \frac{V_{ice}}{1-\phi} \quad (2.2.9)$$

with V_{ice} the volume of ice. The first term of Eqn. 2.2.7 represents the thermal resistance of the gas phase in the cross section l_t^2 , of length $(l_t - l_s - 2l_{wa})$. The second term is the thermal resistance of the ice and gas phase in the cross section l_t^2 , of length $(2l_{wa})$. The third term is the thermal resistance of the ice, gas and solid in the cross section l_t^2 , of length (l_s) . It must be noted that this is valid only for a low volume content of ice, which is fine for the time of the Phoenix mission. When the volume content of ice is higher, more complex equations which account for various ice distribution in the cell are desired.

2.2.1 Governing Equations for the Regolith

Transport of gas in the regolith is governed by the conservation of mass, momentum and energy through porous media. These processes have been studied both experimentally and theoretically for decades. Applications involving porous media are found in many areas of science and engineering, such as the movement of oil and gas in reservoirs, heat and mass transport in packed bed chemical reactors, contaminant transport in soil and the filtration processes in lungs to name a few. Porous materials, such as terrestrial soils, are considered as solids with a connected void space through which a fluid can flow. Such structures cause obstruction (resistance) to the fluid passing through them. To represent these effects, various macroscopic models have been developed. The simplest model is based on Darcy's law [75] which relates the volumetric

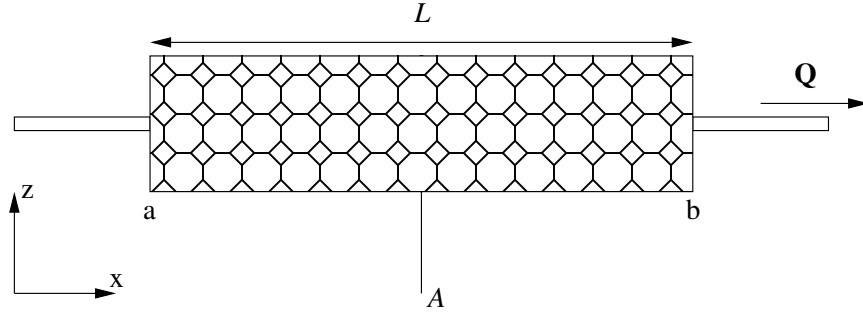


Figure 2.6: Diagram showing definitions and directions for Darcy's law.

flow rate, Q , through a porous medium under a hydraulic pressure gradient as

$$Q = -\frac{KA}{\mu} \frac{P_a - P_b}{L} \quad (2.2.10)$$

where K is the permeability of the porous medium, A is the total cross-sectional area orthogonal to the flow and $P_b - P_a$ is the pressure drop over a given distance L , as shown in Fig. 2.6. Dividing Eqn. 2.2.10 by the area leads to

$$\mathbf{w} = -\frac{K}{\mu} \nabla P \quad (2.2.11)$$

where \mathbf{w} is the filtration velocity and ∇P is the pressure gradient. Gravity effects may be incorporated by replacing the preceding pressure term by $P - \rho g$. The velocity \mathbf{w} , often referred to as the Darcy or superficial velocity, is not the velocity of the fluid in the pores. The solid matrix takes up some of the flow area, thus it is the velocity averaged over the medium. The velocity averaged over the pore space, \mathbf{v} is given by

$$\mathbf{v} = \frac{Q}{A\phi} = \frac{\mathbf{w}}{\phi} \quad (2.2.12)$$

The velocity \mathbf{v} , often referred to as interstitial or intrinsic velocity, accounts for the fact that only a fraction of the total medium is available for flow. Finally, the pore velocity is the velocity a conservative tracer would experience if carried by the fluid through the medium. Darcy's law was derived for steady state, unidirectional flow and holds for small velocities. For larger velocities

Dupuit [76] and Forchheimer [77] proposed the relation in which the drag is not linearly proportional to the velocity and inertial effects result in fluxes lower than those predicted by Darcy's law. Velocities in porous media are generally sufficiently slow, which means that the Reynolds number is order of unity or smaller. Therefore, in this work inertial effects are neglected and there is no need to account for the non-linear behaviour of the pressure difference versus velocity.

The permeability, which is a measure of a porous medium's resistance to fluid flow through its pores, is typically determined experimentally. An estimate of K is given by the Carman-Kozeny relationship [78]

$$K = \frac{D_o^2 \phi^3}{C_\tau (1 - \phi)^2} \quad (2.2.13)$$

where D_o is the pore size and C_τ includes the effect of the tortuosity factor, defined as the square of the ratio of the effective average path length in the porous medium to the shortest distance along the direction of the flow. Recent studies report $C_\tau=150$, which gives good agreement with experiments. This equation was derived for a packed bed of uniform, smooth spherical particles and it is only valid for laminar flow. Since the permeability measurements of a lunar soil simulant JSC-1A, for which the particle size and shape distribution are extremely wide, agree well with this relation [79], Eqn. 2.2.13 is used to predict the permeability of the regolith. Assuming the effective grain size of $\sim 80 \mu\text{m}$ [68], the resulting permeability is $K \sim 4 \times 10^{-11} \text{ m}^2$.

The conservation of the total mass for the regolith is

$$\frac{\partial \phi \rho}{\partial t} + \nabla \cdot (\rho \phi \mathbf{v}) = 0 \quad (2.2.14)$$

Upon derivation of the momentum equation for the regolith, an extra source term R_p is found, which accounts for a porous momentum resistance [80]

$$R_p = -\mathbf{v} \frac{\mu}{\phi K} \quad (2.2.15)$$

In case of an incompressible flow, the momentum equation in the regolith becomes [81]

$$\rho \left[\frac{\partial}{\partial t} (\phi \mathbf{v}) + \nabla \cdot (\phi \mathbf{v} \mathbf{v}) \right] = -\phi \nabla P + \nabla \cdot \left[\mu \phi \left(\nabla \mathbf{v} + (\nabla \mathbf{v})^T \right) \right] + \phi \rho \mathbf{g} - \mathbf{v} \frac{\mu}{K} \quad (2.2.16)$$

This equation is valid both in the regolith ($\phi \neq 1$, $K \ll \infty$) and in a fluid ($\phi=1$ and $K=\infty$). For a steady-state process, relatively small velocities and a homogenous porous medium, Eqn. 2.2.16 becomes the Darcy's law (Eqn. 2.2.11).

Heat transfer in the regolith domain is modelled separately for each phase. For the fluid phase the energy equation is

$$\rho \phi \left[\frac{\partial h}{\partial t} + \nabla \cdot (\mathbf{v} h) \right] = \phi \nabla \cdot (\Gamma_e \nabla h) + \phi S_E + Q_{fs} \quad (2.2.17)$$

where Γ_e is an effective thermal diffusivity defined as $\Gamma_e = k/(\rho c_p)$. For the solid phase the heat transfer is modelled with

$$\rho c_{p_s} \phi_s \left[\frac{\partial T_s}{\partial t} + \nabla \cdot (\mathbf{v}_s T_s) \right] = \phi_s \nabla \cdot (k_s \nabla T_s) + Q_{sf} \quad (2.2.18)$$

where T_s is the temperature of the solid phase. The interfacial heat transfer between the fluid and the solid, Q_{fs} , is determined using an overall transfer coefficient model

$$Q_{fs} = -Q_{sf} = \mathbf{h} A_{fs} (T_s - T_f) \quad (2.2.19)$$

where \mathbf{h} is the overall heat transfer coefficient between the fluid and the solid and A_{fs} is the fluid-solid area density.

2.2.2 Knudsen Diffusion

As discussed in previous section, the driving force for flow in a porous solid is typically the total pressure gradient. The resistance to flow is caused mainly

by the viscosity of the gas. The mass transport of gases results not only from advection but also from diffusion, where a difference in concentration, temperature, and pressure results in segregation of the different component gases. Thermodiffusion and barodiffusion are usually small compared with concentration diffusion. Although, in some cases on Mars, they can be significant. For example, considering dust devils, the pressure drop in the shallow regolith above the ice table, $\Delta p_0/p_0$, can be up to 15% [82]. In the present case, since dust devils are not considered, the pressure is considered constant through the regolith and the pressure diffusion effect can be safely omitted. Thermal diffusion, however, may play an important role in the surface soil layer where large daily fluctuations in temperature gradients occur [83]. This effect is discussed separately in the next section.

In an environment where temperature and pressure change little, the concentration diffusion J_{diff} is given by Fick's first law

$$J_{diff} = -D_{\alpha\beta} \frac{\partial \rho_\alpha}{\partial z} \quad (2.2.20)$$

where $D_{\alpha\beta}$ is the normal diffusion coefficient, and has been already explained in section 2.1.5. For a porous medium, the diffusion coefficient is written as [84]

$$D_p = \frac{\phi}{\tau} D_{\alpha\beta} \quad (2.2.21)$$

where τ is tortuosity and the ratio ϕ/τ is called the obstruction factor. This formulation is valid as long as the gas molecules collide more frequently with each other than with the pore walls. When the pressure is low, collisions are dominantly between the solid walls of the porous medium and molecule-molecule collisions have negligible effect. This is referred to as Knudsen diffusion. In this regime, the diffusive flux depends only on the mass concentration gradient of the species of interest and it is expressed as [84]

$$J_\alpha = -D_{\alpha K} \frac{\partial \rho_\alpha}{\partial z} \quad (2.2.22)$$

where $D_{\alpha K}$ is the Knudsen diffusion coefficient, which can be estimated by [85]

$$D_{\alpha K} = \frac{2}{3} r_p \left(\frac{8RT}{\pi M_w} \right)^{\frac{1}{2}} \quad (2.2.23)$$

r_p is the pore radius and R is the universal gas constant. $D_{\alpha K}$ is a function of the pore radius, is independent of total pressure and varies with $T^{\frac{1}{2}}$.

In the case where both collisions with pore walls and with other molecules occurs with similar frequency (which is the most likely case on Mars) the diffusion will have a mixed Fickian and Knudsen diffusion character. This transition region is defined by the ratio of the pore size to the mean free path r_p/λ . When $r_p/\lambda \ll 1$ the diffusion is said to lie in the Knudsen regime and in the Fickian regime, when $r_p/\lambda \gg 1$. In the transition regime, $r_p \sim \lambda$, an effective diffusion coefficient is usually represented by the Bosanquet relation [84]

$$\frac{1}{D'} = \frac{1}{D_{\alpha\beta}} + \frac{1}{D_{\alpha K}} \quad (2.2.24)$$

The Bosanquet equation requires the conditions of equimolar counterdiffusion of a binary mixture and it is rigorously valid only for diffusion within a long cylindrical pore. Pollard and Present [86] showed that, the reference diffusivity, D' , becomes equal to $D_{\alpha\beta}$ in the Fickian diffusion regime (i.e., high pressure) and to $D_{\alpha K}$ in the Knudsen regime (i.e., low pressure). Since on Mars $D_{\alpha K}$ is ten times larger than the bulk diffusivity, $D_{\alpha\beta}$, Eqn. 2.2.24 is applicable. As an alternative to Eqn. 2.2.24, Wheeler [87] suggested the semi-empirical formula

$$D' = D_{\alpha\beta} + \left[1 - \exp\left(-\frac{D_{\alpha K}}{D_{\alpha\beta}}\right) \right] \quad (2.2.25)$$

The calculation of effective diffusivities in the regolith requires equations 2.2.24 and 2.2.25 to be modified in order to account for pores that vary in size, shape and connectivity. Thus, effective diffusivities in the regolith become

$$D_{eff} = \frac{\phi}{\tau} D' \quad (2.2.26)$$

CHAPTER 2: THEORY

Here, the porosity, ϕ , accounts for the reduction in cross-sectional area for diffusion posed by the solid material and the tortuosity, τ , accounts for the increased diffusion length due to the tortuous nature of the pores and for the effects of constrictions and dead-end pores. The flux equation is again analogous to Fick's law

$$J_{diff} = -D_{eff} \frac{\partial \rho_\alpha}{\partial z} \quad (2.2.27)$$

Hudson et al. [42] performed a series of experiments on a variety of materials that could resemble the Martian regolith. For most of their samples, the diffusion coefficients were in the range of 1.9 to 4.7 cm² s⁻¹ at 600 Pa and 200 K. For JSC Mars-1, with porosity of 58% and same pressure and temperature, the diffusion coefficient was found to be 3.67±0.5 cm² s⁻¹. Knowing that the ordinary diffusion coefficient of water vapour in CO₂ gas is 16.19 cm² s⁻¹ (Eqn. 2.1.44) at 600 Pa and 200 K, and assuming the effective pore radius of 40μm, D' can be obtained from equations 2.2.23 - 2.2.24. Next, solving Eqn. 2.2.26 for tortuosity gives

$$\tau = \phi \frac{D'}{D_{eff}} = 0.58 \frac{14.4}{3.67} = 2.3 \quad (2.2.28)$$

This is within the range $\tau=2.6\pm0.4$ calculated by Hudson et al. [42]. With tortuosity of 2.3 and porosity of 58%, D_{eff} can now be calculated for different temperature and pressure. For example, for $P=774$ Pa and $T_{reg}=215$ K, equations 2.2.23 - 2.2.26 yield $D_{eff}=3.2\pm0.5$ cm² s⁻¹. This includes all the ob-

ρ_s	c_{ps}	k_s	D_{H_2O,CO_2}	D_{eff}	OF	K
[kg m ⁻³]	[J kg ⁻¹ K ⁻¹]	[W m ⁻¹ K ⁻¹]	[cm ² s ⁻¹]	[cm ² s ⁻¹]	[-]	[m ²]
3293	768	0.04 [†]	14.0	3.2	0.23	4×10 ⁻¹¹

[†]After including the obstruction factor

Table 2.1: *Regolith properties used in the simulations.*

struction and Knudsen effect, which are given here by the obstruction factor

$$OF = \frac{D_{eff}}{D_{H_2O,CO_2}} = \frac{3.2}{14} = 0.23 \quad (2.2.29)$$

Table 2.1 summarizes all regolith properties used in the simulations.

2.2.3 Thermal Diffusion

Thermal diffusion is the transfer of gas caused by a temperature gradient. It results from momentum exchange between molecules of different masses [88]. This phenomena should be taken into account when a multi-component mixture is exposed to a relatively high temperature gradient. Since Martian soil is continuously subjected to changing temperatures, it is possible for thermal diffusion to become important. It is also possible for water to move from a warm to a cooler area in cases when thermal gradients dominate. This could explain why during the Phoenix mission, the reduction in atmospheric vapour content started before either the surface or atmosphere has cooled to the frost point each night.

To include the effect of thermal diffusion, an additional term is required in Eqn. 2.1.22. Mills [89] showed that for a binary mixture, the mass flux, \mathbf{j}_α , is

$$\mathbf{j}_\alpha = -\rho D_{\alpha\beta} \left[\nabla\omega_\alpha + \frac{M_{w_\alpha} M_{w_\beta} k_{T_\alpha}}{M_{w_{\alpha\beta}}^2 T} \nabla T \right] \quad (2.2.30)$$

where k_{T_α} is the thermal diffusion ratio of component α . It measures the relative importance of thermal and ordinary diffusion. If k_{T_α} is positive, component α diffuses to a cooler region; otherwise, it moves toward a hotter region [50]. An alternative form of the diffusion flux is obtained by introducing the thermal diffusion factor

$$\alpha_{T_\alpha} = \frac{k_{T_\alpha}}{x_\alpha x_\beta} \quad (2.2.31)$$

Substituting Eqn. 2.2.31 into Eqn. 2.2.30 gives

$$\mathbf{j}_\alpha = -\rho D_{\alpha\beta} \left[\nabla\omega_\alpha + \omega_\alpha \omega_\beta \frac{\alpha_{T_\alpha}}{T} \nabla T \right] \quad (2.2.32)$$

This form is more preferable since α_{T_α} is independent of composition [90]. For the binary mixture, the thermal diffusion factor is obtained via the relation given by Bzowski et al. [91]

$$\alpha_{T_\alpha} = (6C_{\alpha\beta}^* - 5) \left(\frac{x_\alpha S_\alpha - x_\beta S_\beta}{x_\alpha^2 Q_\alpha + x_\alpha x_\beta Q_{\alpha\beta} + x_\beta^2 Q_\beta} \right) \quad (2.2.33)$$

where the functionals S and Q are reproduced in A.6 and the coefficient $C_{\alpha\beta}^*$ is discussed below. Multiplying the first term in Eqn. 2.2.33 by the terms containing the S 's and Q 's removes the strong dependencies on composition, molecular mass and the collision integrals that represent the interactions of like molecules. This derivation of α_{T_α} demonstrates a temperature dependent quantity, which is dominated by only the unlike interactions. In general, the interaction between a pair of molecules is given by a potential energy function. The typical shape of an interaction potential between two neutral atoms is shown in Fig. 2.7. At short range, the interaction is repulsive due

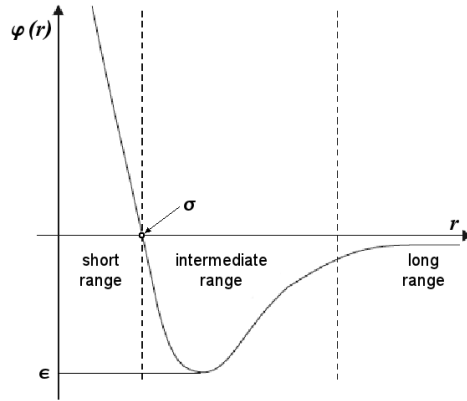


Figure 2.7: *Generic shape of an interaction potential.*

to Coulomb forces between the electron clouds surrounding both atoms. At intermediate range, the interaction is attractive but its influence vanishes at large separations. The most commonly used potential is the Lennard-Jones (12-6) potential (LJ) [92], given by

$$\varphi(r) = 4\epsilon \left[\left(\frac{\sigma}{r} \right)^{12} - \left(\frac{\sigma}{r} \right)^6 \right] \quad (2.2.34)$$

where σ is a characteristic diameter of the molecules at which the potential energy is zero and ϵ is the maximum energy of attraction between interacting molecules. Values of σ and ϵ are known for a number of non-polar molecules including CO₂. Such information is also available for strongly polar molecules such as H₂O. The main difficulty is to predict σ and ϵ for mixtures. This is done through the use of empirical combining rules which relate the force constants between non-identical components. In mixtures, where both polar and non-polar molecules are present, Hirschfelder et al. [51] suggests the following correlation

$$\sigma_{np} = \frac{1}{2} (\sigma_n + \sigma_p) \xi^{-\frac{1}{6}} \quad (2.2.35)$$

$$\epsilon_{np} = \sqrt{\epsilon_n \epsilon_p} \xi^2 \quad (2.2.36)$$

where

$$\xi = 1 + \frac{1}{4} \alpha_n^* \nu_p^{*2} \sqrt{\frac{\epsilon_p}{\epsilon_n}} \quad (2.2.37)$$

Here, σ_n , ϵ_n are LJ potential parameters for the non-polar molecules, σ_p , ϵ_p are Stockmayer potential parameters for the polar molecules, α_n^* is reduced polarizability of the non-polar molecule, and ν_p^{*2} is reduced dipole moment of the polar molecule. Using force constants for the Stockmayer potential, Hirschfelder et al. [51] calculated the third virial coefficient, $C_{\alpha\beta}^*$, for three gases including H₂O. Since there is a distinct disagreement between the calculated and experimental values for water vapour and the calculation of the thermal diffusion ratio (Eqn. 2.2.33) requires $C_{\alpha\beta}^*$, the above combining rules do not give appropriate results in some situations. A more accurate empirical laws are based on the work of Tang and Toennies [93] and were extended to molecular systems by Bzowski et al. [91]. It has been also shown [51] that, the effective potential energy of interaction between a polar and a non-polar molecule (e.g., H₂O-CO₂) has the same form as that between two non-polar molecules. Hence the force constants for the Lennard-Jones potential may be used for calculations of the functionals in Eqn. 2.2.33. These functionals are expressed in terms of the collision integrals $\Omega_{\alpha\beta}^{(1,1)*}$ and $\Omega_{\alpha\beta}^{(2,2)*}$ and the

higher order coefficients $A_{\alpha\beta}^*$, $B_{\alpha\beta}^*$, $C_{\alpha\beta}^*$ which are functions of the dimensionless temperature $T^* = k_b T / \epsilon$. In this study, these functions are calculated using polynomial expressions, which have been developed in order to update the current transport packages (e.g., MIXRUN, CHEMKIN and EGLIB) [94]. The new approach is based on more physically realistic molecular potential, which allows to include the dipole-induced dipole and dipole-dipole attractive terms directly into the collision integrals for non polar-polar interactions. In addition, the relations for the collision integrals were extended to lower reduced temperatures, T^* , where quantum effects become important. They cover the range $0.2 \leq T^* < 1.0$. This was done to get the correct values for species like H_2O . The new potential parameters for H_2O and CO_2 are tabulated in Table 2.2 along with the Stockmayer potential parameters for H_2O .

Substance	σ [\AA]	ϵ/k_b [K]	ν [debyes]	α [\AA^3]	C_6^*
CO_2	3.769	245.30	0	2.65	1.860
$\text{H}_2\text{O}^\dagger$	2.673	532.21	1.847	1.45	1.612
$\text{H}_2\text{O}^\ddagger$	2.650	380.00	1.830	-	-

[†]Values for the Effective central potential

[‡]Values for the Stockmayer potential

Table 2.2: *Molecular potential parameters.*

According to Zent et al. [4], the reduction in atmospheric water vapour content (Sol 70) begins during the early evening when the ground and air temperatures are well above the frost point. At this time ($\sim 17:00$ local Mars time) the regolith temperature was reported to be 215 K (at the ice table) and 245 K (at the surface) with a volume mixing ratio of 0.0014. Within this temperature range, the reduced temperatures are calculated using the values from Table 2.2 and the combining rules proposed by Bzowski et al. [91] (shown in A.7). Next, the collision integrals and the higher order coefficients (provided

in A.8 for completeness) are programmed in Matlab (see B.1) and used for the calculation of $\alpha_{T_{H_2O}}$. Fig. 2.8 shows the thermal diffusion factor as a function of temperature. As a comparison, the values of $\alpha_{T_{H_2O}}$ calculated from

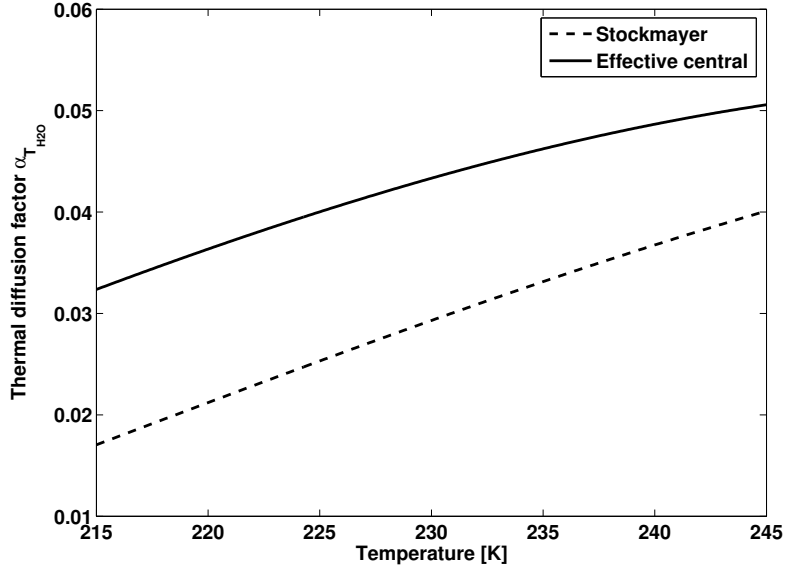


Figure 2.8: Thermal diffusion factor for mixture of H_2O-CO_2 at constant volume mixing ratio. Solid line shows the values of $\alpha_{T_{H_2O}}$ calculated from the force constants for the central potential and the dotted line for the Stockmayer molecular potential.

the Hirschfelder et al. [51] empirical laws are also plotted. The difference is up to 50%. It is not known whether the difference is due to incorrect input parameters or to not including the correction for dipoles for the Stockmayer potential. There is no available data whereby these results may be checked. However, it is interesting to note that when applying the Stockmayer potential in order to fit experimental viscosity data for species with a reduced parameter $\delta^* > 1$, the Stockmayer fits are found to be poor. The reduced parameter $\delta^* = \nu^{*2}/2\epsilon\sigma^3$ and is 1.2 for H_2O . Rather, the fits using the effective central potential agree well for H_2O and for all other polar species tested over the range $0.03 \leq \delta^* < 2.4$ [94]. Therefore, in the simulations, values of thermal diffusion factor calculated based on the central potential will be used.

2.3 Surface Temperature and Solar Radiation

The day to day variation of the local water vapour content is controlled primarily by the amount of solar radiation reaching the surface. Thus, the first step in modelling water cycle on Mars is to calculate energy flux to the surface, which represents the net heat load from the Sun.

The surface energy flux into the ground, \dot{q}_{ground} , depends on the irradiation from the Sun and the atmosphere (G_S), the radiation from the soil to the sky (I_{rad}), the wind dependent sensible heat flux (H), and the latent heat flux (LE) [95]

$$\dot{q}_{ground} = G_S - I_{rad} - H - LE \quad (2.3.1)$$

The sensible and latent heat fluxes are usually small comparing to the other fluxes [30] and are not considered here. Hence, the resulting total net radiation at the surface is calculated as the net value of heat absorbed due to incident solar irradiation and heat emitted due to surface radiation using

$$R_{net} = S_{net} - L_{net} \quad (2.3.2)$$

The ground-absorbed net solar flux, S_{net} , is expressed as

$$S_{net} = \alpha_S G_S \quad (2.3.3)$$

where α_S is the fraction of irradiation absorbed by the surface. The total solar energy incident on a horizontal surface, G_S , is composed of direct and diffusive components. The direct component is the light reaching the surface directly from the Sun, while the diffusive component is the light which comes from atmospheric scattering. The direct solar ray is affected by gas molecules and suspended dust particles in the atmosphere. The intensity of this attenuation is defined in terms of the optical depth τ_o , an atmospheric sciences term that refers to the relative “distance” a beam of light penetrates through the atmosphere. τ_o is measured downwards from the top of the atmosphere,

so $\tau_o=0$ at the top, and it increases downward as the spatial distance to the object decreases. Measurements of the optical depth allows for an estimate of a fraction of radiation that is lost from an original ray. Recent measurements of optical depth in the atmosphere of Mars were taken by the Phoenix Lander and the Mars Reconnaissance Orbiter (MRO). During the Phoenix mission, the optical depth was found to be $0.1 < \tau_o < 1.0$ [62].

To calculate the direct solar irradiation, the solar irradiation at the top of the atmosphere must be calculated first. The variation of the solar irradiation at the top of the atmosphere is governed by the location of Mars with respect to the sun, and is given by

$$S_{TOA} = 590 \frac{[1 + e_M \cos(L_S - 248^\circ)]^2}{(1 - e_M^2)^2} \quad (2.3.4)$$

where L_S is the aerocentric longitude of the sun [96]. On Mars, unlike on Earth, a given day is not determined by the day of the month. It is, however, specified by the position of Mars in its orbit around the Sun, L_S . In the Mars northern hemisphere at vernal equinox $L_S=0^\circ$, at summer solstice $L_S=90^\circ$, at autumnal equinox $L_S=180^\circ$, and at winter solstice $L_S=270^\circ$. The aerocentric longitude of Mars perihelion is 248° . Since Mars orbital eccentricity e_M is greater than of Earth, its solar time can diverge from clock time much more than on Earth. Thus, the difference between the Local True Solar Time (LTST) and the Local Mean Solar Time (LMST) varies between -51.1 min and +39.9 min [97]. For Earth, the difference is three times smaller. The Sun-Mars mean distance is 1.5236915 AU (astronomical units), and the solar constant at the distance of 1 AU (the mean Sun-Earth distance) is 1371 W m^{-2} . Therefore, the mean solar flux at the top of the Martian atmosphere is $1371/1.5236915^2=590 \text{ W m}^{-2}$.

Next, the direct solar irradiation on the Martian surface normal to the solar rays is

$$S_D = S_{TOA} \cos(\Theta_z) \exp\left(-\frac{\tau_o}{\cos(\Theta_z)}\right) \quad (2.3.5)$$

CHAPTER 2: THEORY

where Θ_z is the solar zenith angle given by

$$\cos(\Theta_z) = \sin(\phi_L) \sin(\delta_s) + \cos(\phi_L) \cos(\delta_s) \cos(\gamma_h) \quad (2.3.6)$$

Here ϕ_L is latitude, γ_h is hour angle ($\gamma_h = 15t - 180^\circ$) and δ_s is the solar declination angle defined by

$$\sin(\delta_s) = \sin(\delta_0) \sin(L_S) \quad (2.3.7)$$

where $\delta_0=24.936^\circ$ is the Mars obliquity of rotation axis. Furthermore, the global solar irradiation, G_S , on a horizontal surface is determined by the normalized net solar flux function $f(\Theta_z, \tau_o, a)$ according to Appelbaum et al. [98] as

$$G_S = S_{TOA} \cos(\Theta_z) \frac{f(\Theta_z, \tau_o, a)}{\alpha_S} \quad (2.3.8)$$

where a is the surface albedo or reflectivity. For opaque surfaces, the sum of the fractions of irradiation absorbed and emitted by the surface is equal to one ($1 - a = \alpha_S$). Next, using equations 2.3.3 and 2.3.8 gives

$$S_{net} = S_{TOA} \cos(\Theta_z) f(\Theta_z, \tau_o, a) \quad (2.3.9)$$

The diffusive irradiance is obtained by subtracting the direct from the global irradiances (Eqns. 2.3.5 and 2.3.8). The net radiation heat loss rate from the ground can be calculated as

$$L_{net} = L_u - L_d \quad (2.3.10)$$

The surface long-wave upwelling flux is

$$L_u = \varepsilon k_b T_g^4 \quad (2.3.11)$$

where ε is the emissivity and T_g is the surface temperature. The downwelling flux from the atmosphere L_d is more constant, and it is assumed to be $\sim 30 \text{ W m}^{-2}$ [99].

3

Numerical Method

In the last few decades, due to availability of powerful computers and CFD software numerical solution to practical fluid problems is possible. In this chapter, the numerical discretization procedure, which is based on the Finite Volume Method (FVM), is introduced. Software limitations and additional steps, which are required to represent certain boundaries and sources, are also discussed.

3.1 Numerical Code

In this study, the commercial code ANSYS CFX 13.0 is used. It was chosen, because it has capabilities of solving multiphase, multicomponent flow with heat and mass transfer for solids and fluids. The use of parallel solver is an important feature, since phase change modelling is computationally very expensive. As it is a finite volume based code, strong conservation is ensured on all control volumes. ANSYS CFX 13 uses first and second order discretization schemes. For the advection term, it offers the High Resolution scheme, which blends between upwind (UDS) and central (CDS) differencing schemes automatically. For small gradients and fine grids, it uses pure CDS, while pure UDS is employed in regions of high gradients to prevent non-physical oscillations. For the transient term, two Euler methods are available. In this work, the second order backward Euler implicit scheme is used. This scheme is very robust, but it may create some non-physical oscillations, especially at large Δt . A domain is discretized into finite control volumes using a mesh and all solution variables along with fluid properties are stored at mesh nodes. More detailed explanation of numerical discretization is given in [A.4](#). To avoid decoupling of adjacent cells the pressure is interpolated at cell centres using the Rhie and Chow discretization [100]. The resulting linear set of equations are discrete conservation equations, which written for all control volumes are expressed as

$$\sum_{nb_i} a_i^{nb} \varphi_i^{nb} = b_i \quad (3.1.1)$$

where φ is the solution, b the right hand side, a the coefficients of the equation, i the number of control volume, and nb is the neighbour node. For a scalar equation (e.g., enthalpy), a_i^{nb} , φ_i^{nb} and b_i are each single numbers. For all three momentum equations, u , v , w , and the mass continuity equation, which

is given in terms of pressure are

$$a_i^{nb} = \begin{bmatrix} a_{uu} & a_{uv} & a_{uw} & a_{up} \\ a_{vu} & a_{vv} & a_{vw} & a_{vp} \\ a_{wu} & a_{wv} & a_{ww} & a_{wp} \\ a_{pu} & a_{pv} & a_{pw} & a_{pp} \end{bmatrix}_i^{nb} \quad (3.1.2)$$

and

$$\varphi_i^{nb} = \begin{bmatrix} u \\ v \\ w \\ P \end{bmatrix}_i^{nb} \quad (3.1.3)$$

$$b_i^{nb} = \begin{bmatrix} b_u \\ b_v \\ b_w \\ b_p \end{bmatrix}_i \quad (3.1.4)$$

Instead of solving each equation in turn, a coupled solver combines the entire set of hydrodynamic equations (u , v , w , P) into a single system and solves them simultaneously. While the mass and momentum equations are strongly coupled, the energy equation is not and is therefore solved separately from the others. Additional variables are also solved separately. Multiple domains are connected using a general grid interface algorithm (GGI), which is fully coupled and fully conservative in mass, momentum and energy. In ANSYS CFX, multiple domains are solved simultaneously. It is important to note that, the coefficients at an interface are calculated based on the existing solution on either side of the interface, as opposed to simply interpolating nodal values. The treatment of the interface fluxes is fully implicit, therefore the presence of an interface does not adversely affect overall solution convergence.

CHAPTER 3: NUMERICAL METHOD

The convergence rate is improved by the use of a technique known as multigrid. In ANSYS CFX 13, Algebraic Multigrid (AMG) with an ILU smoother is used to accelerate the solution. With this technique, the discretization of the non-linear equations is performed only once for the finest mesh. Then, control volumes are added together to form larger ones and the direct solver is used. An error correction is solved on each of the coarser grid and passed back up to the finer grid to improve the solution. The exact solution is approached after several iterations, by starting with an initial, approximate solution, φ^n , then correcting it by φ' from coarser grid levels at each iteration, until a converged result is obtained

$$\varphi^{n+1} = \varphi^n + \varphi' \quad (3.1.5)$$

φ' is obtained from

$$A\varphi' = r^n \quad (3.1.6)$$

where r^n is the residual, which comes from imbalance between LHS and RHS of balance equation

$$r^n = b - A\varphi^n \quad (3.1.7)$$

If after n iterations, the normalized residual is below some tolerance δ_{tol} , the iterative procedure stops.

In this study, models are solved in parallel on an 8 processor multicore machine and converged when maximum residuals of the solution are less than 10^{-5} . The maximum residual, or L_∞ norm, is preferred because the most relevant region of the domain (regolith) and where most of the discretization error is concentrated is relatively small compared with the total size of the domain and RMS of the residual, or L_2 norm, would not adequately ensure convergence in that region.

3.2 Theory of Grid Independence

When solving a CFD problem, it is important to check that the solution is not affected by a refinement of the grid size. This can be accomplished by obtaining solutions from various grids. If the difference in some predetermined quantity is less than some threshold, then the numerical solution is said to be asymptotic or grid independent. Information about how close the solution is to the exact solution is known as discretization error. The discretization error, which is due to truncation error (the truncation of the Taylor series), is defined as

$$\epsilon_h^d = \Phi_e - \varphi_h \quad (3.2.1)$$

where Φ_e and φ_h are the exact solution and the numerical solution at grid level h , respectively. For grids that are fine enough, the truncation error is proportional to the leading term in the Taylor series

$$\epsilon_h^d = \alpha' h^p + O \quad (3.2.2)$$

where O is the higher order terms and α' depends on the derivatives at a given point. Using Eqn. 3.2.2, the exact solution can be written as

$$\Phi_e = \varphi_h + \alpha' h^p + O = \varphi_{2h} + \alpha' (2h)^p + O \quad (3.2.3)$$

The exponent p , which is the order of the scheme, can be calculated using

$$p = \frac{\log\left(\frac{\varphi_{2h} - \varphi_{4h}}{\varphi_h - \varphi_{2h}}\right)}{\log 2} \quad (3.2.4)$$

Furthermore, Eqn. 3.2.4 can be used to estimate the discretization error, ϵ_h^d , which then added to the solution on the finest grid results in a better approximation using

$$\epsilon_h^d \approx \frac{\varphi_h - \varphi_{2h}}{2^p - 1} \quad (3.2.5)$$

This method is known as Richardson extrapolation and becomes accurate, when the convergence is monotonic [101]. If the expansion factor between two progressively and systematically refined grids is not two, the factor 2 in the last three equations has to be replaced by that ratio.

3.3 Numerical Implementation

There are two distinct multiphase models that are available in ANSYS CFX, an Eulerian-Eulerian multiphase model and a Lagrangian Particle Tracking multiphase model. In the Eulerian model the interactions between particles are at the continuum level which follows that all particles are treated as a source or sink. For such an approach global information of the particle phase is available. The Lagrangian model, however, is capable of tracking the particle motion explicitly. This gives information on behaviour and residence time of individual particles, but it is expensive if a large number of particles have to be tracked.

In this study, the simulated atmosphere is initialized as a mixture of CO_2 and H_2O in a gaseous phase, and H_2O in a solid phase. A more accurate solution to this problem would be to treat the flow as a single fluid, $\text{CO}_2+\text{H}_2\text{O}$, with the water particles modelled using particle tracking. This would give better details for mass and heat transfer, but it involves complex physics, such as nucleation of the fog and size dependent tracking the dust particles. For a large concentration of particles, it would be computationally very expensive. A more economic way is to consider the flow to be a multicomponent fluid of CO_2^G and H_2O^G in a gaseous phase, while the solid H_2O^S phase can be modelled as an “additional variable”, using the generic transport equation. The additional variable in CFX is treated as a conserved quantity, whose interaction with other conserved variables needs to be explicitly coded. Mass and energy balances use source terms that account for the mass and heat losses during phase change. Defining $\alpha \in \{ \text{CO}_2^G, \text{H}_2\text{O}^G, \text{H}_2\text{O}^S \}$, the total mass conservation equation is

$$\frac{\partial \rho}{\partial t} + \nabla \cdot (\rho \mathbf{v}) = 0 \quad (3.3.1)$$

CHAPTER 3: NUMERICAL METHOD

The mass balance for each component, α , is

$$\frac{\partial \rho_{CO_2}^G}{\partial t} + \nabla \cdot (\rho_{CO_2}^G \mathbf{v} + \mathbf{j}_{CO_2}^G) = r_{CO_2}^G \quad (3.3.2)$$

$$\frac{\partial \rho_{H_2O}^G}{\partial t} + \nabla \cdot (\rho_{H_2O}^G \mathbf{v} + \mathbf{j}_{H_2O}^G) = r_{H_2O}^G \quad \text{and} \quad (3.3.3)$$

$$\frac{\partial \rho_{H_2O}^S}{\partial t} + \nabla \cdot (\rho_{H_2O}^S \mathbf{v} + \mathbf{j}_{H_2O}^S) = r_{H_2O}^S \quad (3.3.4)$$

where the superscripts G and S denote gas and solid phase, respectively, r is the component source/sink term, and \mathbf{j} is the diffusive flux. Using equations 2.1.9 and 2.1.11, Eqn. 3.3.1 is written as

$$\begin{aligned} \frac{\partial}{\partial t} (\rho_{CO_2}^G + \rho_{H_2O}^G + \rho_{H_2O}^S) + \nabla \cdot (\rho_{CO_2}^G \mathbf{v}_{CO_2}^G + \rho_{H_2O}^G \mathbf{v}_{H_2O}^G + \\ + \rho_{H_2O}^S \mathbf{v}_{H_2O}^S) = 0 \end{aligned} \quad (3.3.5)$$

Re-arranging and using equations 3.3.2 to 3.3.4 results in

$$r_{CO_2}^G + r_{H_2O}^G + r_{H_2O}^S = \nabla \cdot (\mathbf{j}_{CO_2}^G + \mathbf{j}_{H_2O}^G + \mathbf{j}_{H_2O}^S) \quad (3.3.6)$$

As shown in A.5, the sum of all mass fluxes is zero and the above equation reduces to

$$r_{CO_2}^G + r_{H_2O}^G + r_{H_2O}^S = 0 \quad (3.3.7)$$

The governing equations for the atmosphere are solved only for the components that are in a gaseous phase, i.e., the volume occupied by the ice fog is essentially neglected. Thus, the last source term in Eqn. 3.3.7 is eliminated, and

$$r_{CO_2}^G = -r_{H_2O}^G \quad (3.3.8)$$

Next, writing Eqn. 2.1.23 for the components that are in a gaseous phase, it follows that the mass fractions are governed by

$$\frac{\partial \omega_{CO_2}^G}{\partial t} + \mathbf{v} \cdot \nabla \omega_{CO_2}^G - D_{H_2O^G, CO_2^G} \nabla^2 \omega_{CO_2}^G = r_{CO_2}^G \quad (3.3.9)$$

and

$$\frac{\partial \omega_{H_2O}^G}{\partial t} + \mathbf{v} \cdot \nabla \omega_{H_2O}^G - D_{H_2O^G, CO_2^G} \nabla^2 \omega_{H_2O}^G = r_{H_2O}^G \quad (3.3.10)$$

where $\omega_{CO_2}^G = \rho_{CO_2}^G/\rho$ and $1 - \omega_{CO_2}^G = \omega_{H_2O}^G$. It should be noted that the last term in Eqn. 3.3.9 is expected to be zero (CO_2 is not expected to have changed phase during the mission), but is needed, however, in order for equations 3.3.9 and 3.3.10 to reduce to Eqn. 3.3.1. The solid H_2O phase is modelled as an additional variable, φ , using the general transport equation

$$\rho \left[\frac{\partial}{\partial t} (\phi\varphi) + \nabla \cdot (\phi\mathbf{v}\varphi) \right] = \nabla \cdot (\phi\Gamma_\varphi \nabla\varphi) + \phi S_\varphi \quad (3.3.11)$$

where Γ_φ is the diffusivity of φ and S_φ is the source term for the generic quantity, which in porous medium is

$$S_\varphi = \varphi \frac{\mu}{\phi K} + S_0 \quad (3.3.12)$$

and S_0 are other sources. For the solid H_2O , Γ_{H_2O} was assumed zero (see section 2.1.5), hence Eqn. 3.3.11 results in

$$\rho \left[\frac{\partial}{\partial t} (\phi\rho_{H_2O}^S) + \nabla \cdot (\phi\mathbf{v}\rho_{H_2O}^S) \right] = \rho_{H_2O}^S \frac{\mu}{K} + \phi r_{H_2O}^S \quad (3.3.13)$$

where $r_{H_2O}^S$ is the sublimation/deposition source term. Whenever the condensed phase increases, the corresponding mass fraction of water vapour is taken out from the domain. In order to keep the total amount of water present in the atmosphere constant, the same mass source term is applied to both the gas and solid phases. Assuming that in a time Δt the thermodynamic equilibrium is reached, the source term for water mass balance is written as

$$r_{H_2O} = \frac{1}{\Delta t} [\rho_{H_2O}^G(T, P_{H_2O}^G) - \rho_{H_2O}^G(T, P_{H_2O}^{Gsat})] \quad (3.3.14)$$

Next, assuming that in a time Δt there is a constant release of a latent heat, the source term for the energy equation becomes

$$S_E = \frac{1}{\Delta t} [\rho_{H_2O}^G(T, P_{H_2O}^{Gsat}) - \rho_{H_2O}^G(T, P_{H_2O}^G)] h_{GS} \quad (3.3.15)$$

An additional source term, in the thermal diffusion model for the water vapour balance equation, is

$$\mathbf{j}_{th}^{H_2O^G} = \nabla \cdot \left(\rho D_{H_2O,CO_2} \alpha_T \omega_{H_2O}^G \omega_{CO_2}^G \frac{\nabla T}{T} \right) \quad (3.3.16)$$

3.4 Software Limitations

Due to limitations in the numerical code, additional steps are required to represent certain boundaries and sources. For example, to represent the ice table at the bottom of the regolith an additional physical domain is needed. This requires a finer mesh and would take more time to solve. Moreover, the current version of ANSYS CFX (13.0) does not support certain variables to be functions of additional variables (e.g., volume porosity, thermal conductivity, heat capacity). In this work, the solid H₂O phase is modelled as an additional variable, and there is no option available in the code to represent the variations in thermal properties and the porosity of the regolith. In this case, a block of ice with constant properties can be replaced by prescribing a constant amount of ice at the bottom boundary. This is done by using a step function available in the code. Therefore, the amount of ice is given as

$$\rho_{H_2O}^S = \rho_{ice} \cdot \text{step}(-Z - Z_{ice}) \quad (3.4.1)$$

which means that, everything below Z_{ice} ¹ is the solid H₂O. Here, the regolith-atmosphere interface is at $Z = 0$.

Another software limitation is the diffusion coefficient, which is globally set as the same for all domains. In order to limit the free continuum diffusion in the porous domain, the ordinary diffusion coefficient, $D_{\alpha\beta}$, has to be multiplied by a factor < 1 (the obstruction factor, OF , defined in section 2.2.2). One possible way is to set the OF as the porous medium porosity in ANSYS CFX. Therefore, in the porous domain the binary diffusion coefficient will be multiplied by the effective porosity (or the obstruction factor) and it will result in the effective diffusion coefficient. In this case, the effective porosity should represent all effects which lower the mass flow.

Finally, the sublimation/deposition source term is implemented numerically

¹The ice table depth is given here as a positive value.

in the code. Here the following conditions are assumed:

- ▶ Sublimation vs deposition

$$\begin{aligned}
 RH < RH_{crit} &\implies \text{Sublimation} \\
 RH = RH_{crit} &\implies \text{Equilibrium} \\
 RH > RH_{crit} &\implies \text{Deposition}
 \end{aligned} \tag{3.4.2}$$

- ▶ Zero ice in control volume

$$\rho_{H_2O}^S = 0 \implies \text{Stop sublimation} \tag{3.4.3}$$

- ▶ Zero water vapour in control volume

$$\rho_{H_2O}^G = 0 \implies \text{Stop deposition} \tag{3.4.4}$$

- ▶ Pores filled with ice

$$Y_{ice} \geq 1 \implies \text{Stop deposition} \tag{3.4.5}$$

This can be coded using the following conditional statement available in ANSYS CFX syntax

$$if(\text{conditional expression}, \text{true expression}, \text{false expression}) \tag{3.4.6}$$

and then, defining the conditional expression as

$$\Delta\rho_{H_2O}^G = \rho_{H_2O}^G - \rho_{H_2O}^G_{sat} \tag{3.4.7}$$

similarly, the sublimation/deposition source term, for the atmosphere, is written as

$$\rho_{H_2O}^G = if(\Delta\rho_{H_2O}^G > 0, \Delta\rho_{H_2O}^G \cdot StopSub, \Delta\rho_{H_2O}^G \cdot StopDep) \tag{3.4.8}$$

Here

$$StopSub \equiv if(\rho_{H_2O}^S < 1e-14, 0, 1) \tag{3.4.9}$$

CHAPTER 3: NUMERICAL METHOD

and

$$StopDep \equiv if (\rho_{H_2O}^G < 1e-14, 0, 1) \quad (3.4.10)$$

In numerical methods it is preferred to avoid zero. Since a double precision solver is used, the value of 1e-14 is a good choice, which is close to machine precision. For the regolith, Eqn. 3.4.5 is added to the last term in Eqn. 3.4.8.

4

Validation and Verification

The most common way to validate a numerical model is to compare the results with an exact solution. If an exact solution is not known, the model can be compared with experimental results or a more accurate model. In this work, environmental conditions reported for Sol 30 of the Phoenix mission are simulated and compared with the results from one-dimensional, numerical model of Savijärvi and Määttänen [38], which are regarded as having high quality. Next, the calculations are verified by performing a grid convergence study. The results of the present one-dimensional model are examined for spatial and temporal convergence. Finally, a transient model of the thermodiffusion effect in a porous medium is solved numerically and compared with experimental measurements of Davarzani et al. [102].

4.1 Validation of Near Surface Atmosphere

To predict the water cycle at the surface of Mars accurately, understanding of near surface phenomena, such as fog or frost formation, is of great importance. Deposition of water vapour depends on several parameters that are not well known: for example, the vertical distribution of dust, which serves as seed particles, the size of these particles, the wetting coefficient and the mixing ratio of water vapour near the surface. In this case, the multicomponent models may not correctly resolve the time at which fog concentration is high, its vertical extent and amount of water ice within it. To validate its correctness, the present model was compared with results from Savijärvi and Määttänen [38] for Sol 30 of the Phoenix mission.

In their paper, a one-dimensional version of the atmospheric mesoscale model of Mars is combined with a numerically accurate temperature diffusion scheme for the soil. The soil temperature diffusion equation is solved numerically within the ground, using the five-point Crank-Nicholson scheme. The surface is forced with predicted surface net energy flux, while deep in the ground the energy flow is zero with the temperature set to a constant value. The surface albedo is set to 0.18 and the thermal inertia to $150 \text{ J m}^{-2} \text{ s}^{-0.5} \text{ K}^{-1}$. The volumetric heat capacity of the ground is assumed to be $0.8 \times 10^{-6} \text{ J m}^{-3} \text{ K}^{-1}$. The model includes turbulence, radiation and cloud and dust physics.

For the validation case, the domain is divided into two regions, a porous region representing the regolith and a pure fluid region representing the atmosphere. The regolith domain is 6.5 cm deep and the atmosphere domain is 12.5 m high. To limit computational costs, the domain size is limited to only one control volume in z - direction. The domain is discretized using a structured quadrilateral mesh with a total of 5500 nodes. The mesh size systematically increases from being fine in the regolith and at the interface, to a coarser sized mesh at the top of the domain, in atmosphere. Free slip adiabatic boundary

conditions are used at the top of the domain. This interpretation is necessary due to limited computational resources. It is also reasonable to assume no momentum transfer since radiation fog requires nearly quiescent atmospheric conditions. At the bottom of the regolith, a no-slip wall with a constant ice temperature of 207.5 K is applied. At the atmosphere-regolith interface, a conservative flux for all transport variables is prescribed. All side boundaries are taken to be symmetry boundaries. The initial surface pressure is taken from Savijärvi and Määttänen [38], as are the temperature and moisture profiles and the properties described below. Initially, there is no ice in the domain, except at the bottom surface of the regolith, which is the ice table and its density is set to 918 kg m^{-3} . The critical relative humidity for fog formation is assumed to be 120%. For the regolith, 45% volume porosity is used and the permeability is set to $1 \times 10^{-12} \text{ m}^2$. Thermal conductivity of the regolith is calculated based on the volumetric heat capacity and thermal inertia used by Savijärvi and Määttänen [38]. Thus, for the solid part of the regolith, the

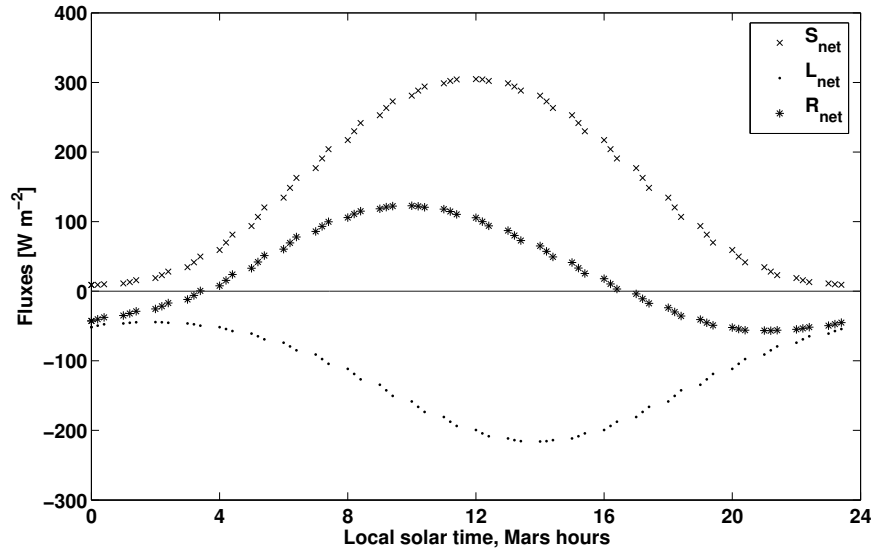


Figure 4.1: Surface energy fluxes calculated for Sol 30 of the Phoenix mission. S_{net} is the net solar irradiation flux, L_{net} is the net radiation from the ground, and R_{net} is the net radiation at the surface.

resulting thermal conductivity is

$$k_s = \frac{I^2}{c_v(1-\phi)} = \frac{150^2}{0.8 \cdot 10^6 \cdot (1-0.45)} = 0.051 \text{ W m}^{-1} \text{ K}^{-1} \quad (4.1.1)$$

The surface temperature is driven by the net solar energy flux, which is applied at the regolith-atmosphere interface boundary. Assuming that the surface albedo is 0.18 and the optical depth is 0.6 (same as in Savijärvi and Määttänen [38]), the surface energy flux can be calculated based on the theory described in section 2.3. Fig. 4.1 shows the model's surface energy fluxes calculated for Sol 30 ($L_S=90^\circ$) of the Phoenix mission. The fluxes are calculated as functions of local true solar time (LT). The net radiation at the surface R_{net} is negative between 1700 LT and 0400 LT, with the lowest -60 W m^{-2} at about 2100 LT. The L_{net} long wave flux from the ground is strongly negative in the afternoon.

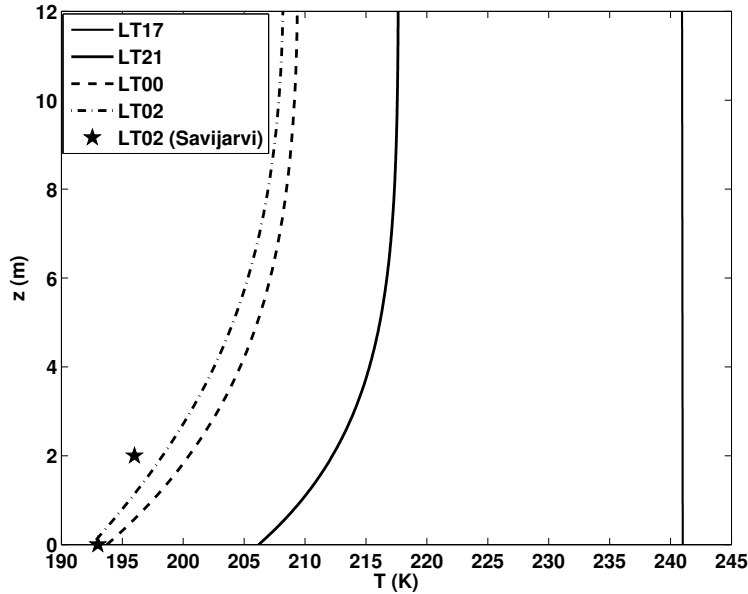


Figure 4.2: Temperature profiles for the Phoenix site at $L_S=90^\circ$ at 1719, 2100, 0000 and 0200 LT from the Sol 30 simulation.

The model starts at 1719 LT, which corresponds to 1700 LMST (mean local solar time) for $L_S=90^\circ$. For this time of the day, the moisture profiles display nearly constant values of specific humidity (about 0.3 g kg^{-1}) up to 4 km height [38]. The surface temperature is set to 241 K, which corresponds to the Phoenix mission observations and is taken to be dry adiabatic in the atmosphere (4.5 K/km). In the regolith, the temperature profile is linear at 1700 LMST [15]. The surface reference pressure remains constant at 817 Pa. The latent heat of sublimation of water is set to 2830 kJ kg^{-1} and the binary diffusion coefficient of water vapour in carbon dioxide is $0.014 \text{ m}^2 \text{ s}^{-1}$. In this simulation a time step of 1.0 s is used.

Results of the validation are shown in figures 4.2 - 4.4. Fig. 4.2 illustrates the model's temperature profiles at 1719, 2100, 0000 and 0200 LT. Initially, the atmosphere is well-mixed, which results in a near constant temperature profile

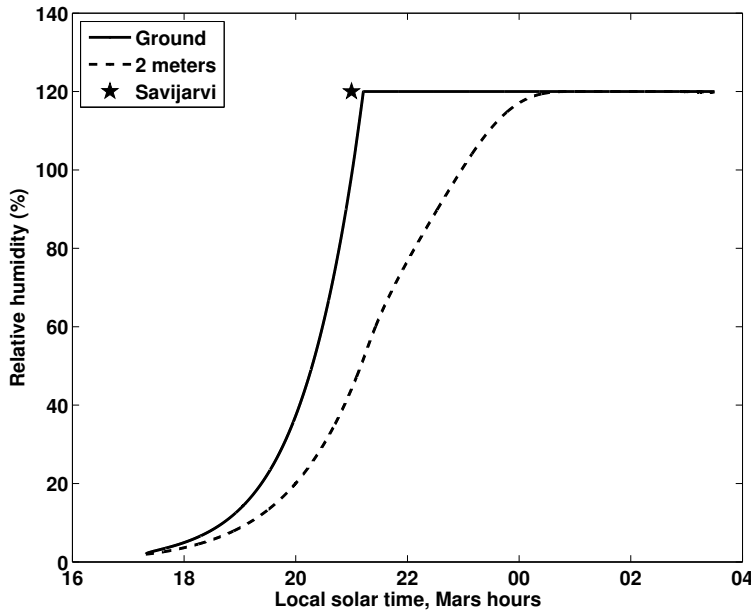


Figure 4.3: Modelled relative humidity at the ground (solid) and at 2 m above the ground (dashed) for Phoenix sols 30 to 31.

at 1719 LT. According to Savijärvi and Määttänen [38], such a well-mixed layer extends to 4 km by 1700 LMST. Then, the air near the surface cools strongly and the ground temperature drops to 192.5 K at 0200 LT. This gives a good agreement with $T_g=193$ K in the model of Savijärvi and Määttänen [38]. The difference between 2 m temperatures at 0200 LT is about 1%.

Relative humidity values in the domain are less than 5% (Fig. 4.3) during daytime, but they increase rapidly in the evening, leading to ground frost formation at 2112 LT. This is just 12 min later than the time, when the ground reached the frost point in the model of Savijärvi and Määttänen [38]. The frost formation removes water vapour rapidly from the atmosphere, as shown in Fig. 4.4, and there is another sink of humidity: fog. The amount of fog increases slowly with ice mixing ratio reaching 40.7 ppmm (parts per million by mass) at 2 m by 0200 LT (Fig. 4.5). This gives less than 2% error when comparing to 40 ppmm reported by Savijärvi and Määttänen [38].

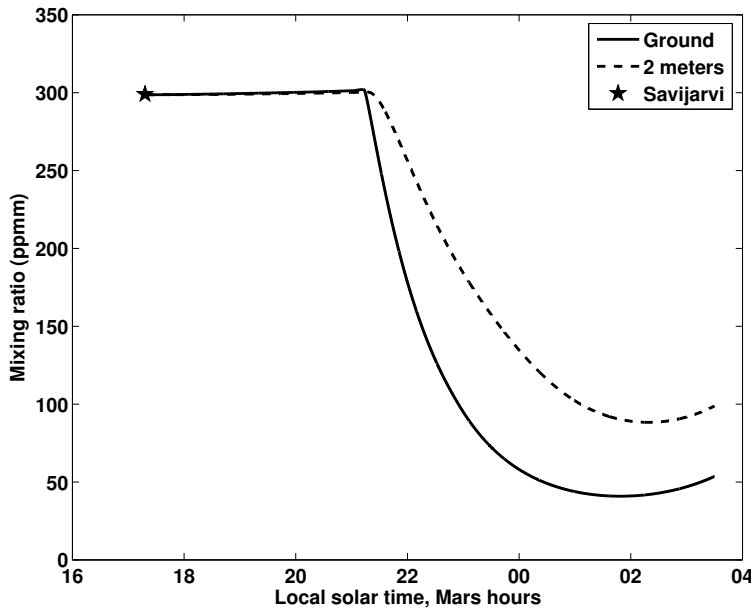


Figure 4.4: *Modelled water vapour mixing ratio for Phoenix sols 30 to 31.*

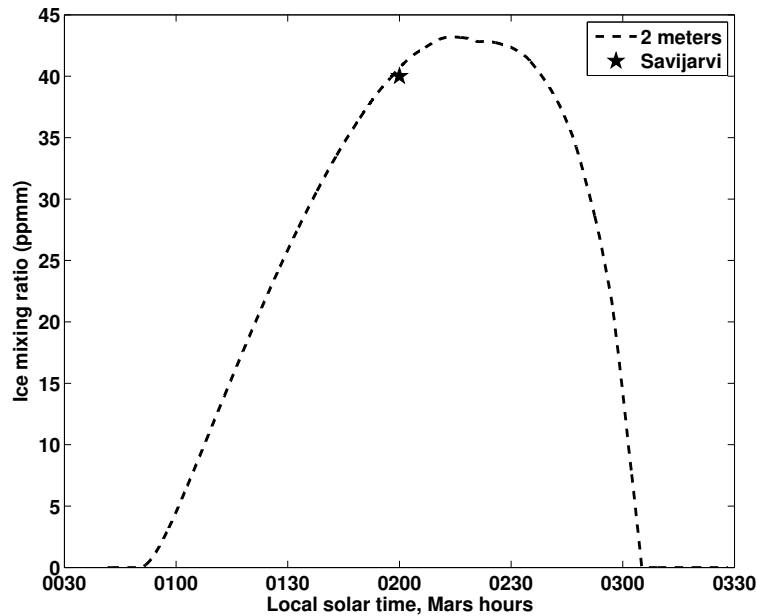


Figure 4.5: *Modelled water ice mixing ratio for Phoenix sols 30 to 31.*

The fog stays until 0300 LT, when it sublimates back into vapour due to the solar heating. This indicates that sublimation and convection drive the moisture correctly back into the atmosphere in the present model.

4.2 Grid Independence Analysis

The grid independence analysis is performed at five systematically refined grids (h_1 to h_5), with a constant arbitrary ratio of 1.5. The results are verified by calculating an arbitrary variable, which has relevance in the analysis. Here the time integral of water vapour mass flux area average at a horizontal plane 1 mm above the surface is calculated. The results are plotted in Fig. 4.6 and listed in Table 4.1.

Grid level	h_1	h_2	h_3	h_4	h_5
No. of nodes	1108	1660	2492	3740	5612
Refinement rate	1.5	1.5	1.5	1.5	1.5
$\int \hat{j}_{H_2O}^G dt @ \text{planeXY}$	1.20e-08	1.22e-08	1.24e-08	1.24e-08	1.25e-08

Table 4.1: Time integral of water vapour mass flux area average at a horizontal plane 1 mm above the surface, calculated at five grid levels.

To ensure that the solution is fairly grid independent in time, the time-step is progressively reduced by ratio of 2. Due to memory resources, only one hour period is simulated. The results of time independence analysis are shown in Fig. 4.7. The time integral of water vapour mass flux varies less than 10^{-9} in space and time directions, which is considered negligible. The results do not allow to estimate the effective order of the scheme, because the variations

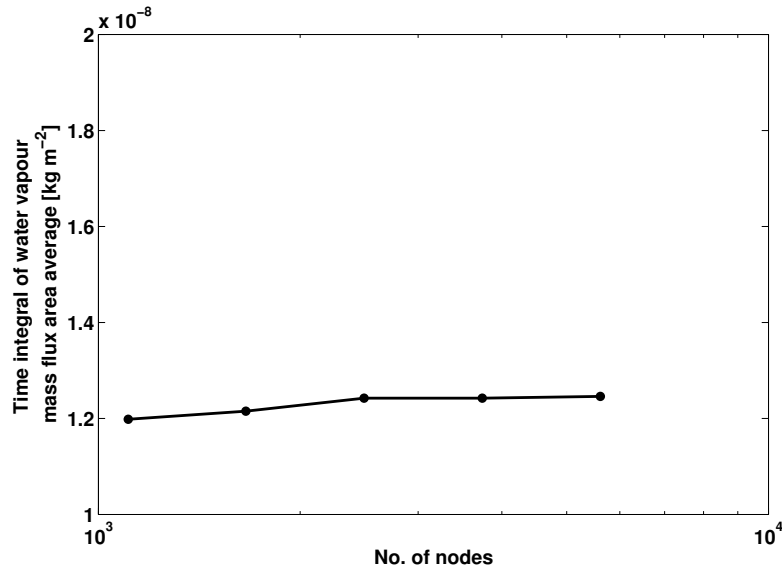


Figure 4.6: Time integral values of water vapour mass flux area average at different grid levels.

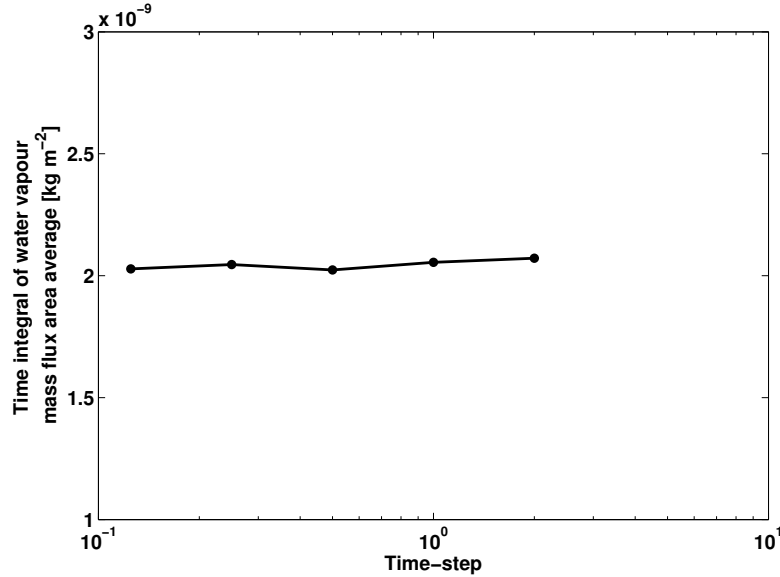


Figure 4.7: *Time integral values of water vapour mass flux area average at different time-steps.*

are close to the machine precision. The solution looks to be in the asymptotic region, which means that the solution is grid independent. Finally, the grid level h_3 has been chosen for the calculations.

4.3 Validation of Thermal Diffusion in the Regolith

To validate the thermal diffusion model in the regolith, a numerical simulation was performed and compared with experimental measurements of Davarzani et al. [102]. In their experiments, they measured the thermal diffusion in a porous medium using binary mixture of He-CO₂. The measurements were obtained with a two-bulb system, containing two chambers joined by a small tube (shown in Fig. 4.8). Each bulb has a constant volume of 1000 cm³.

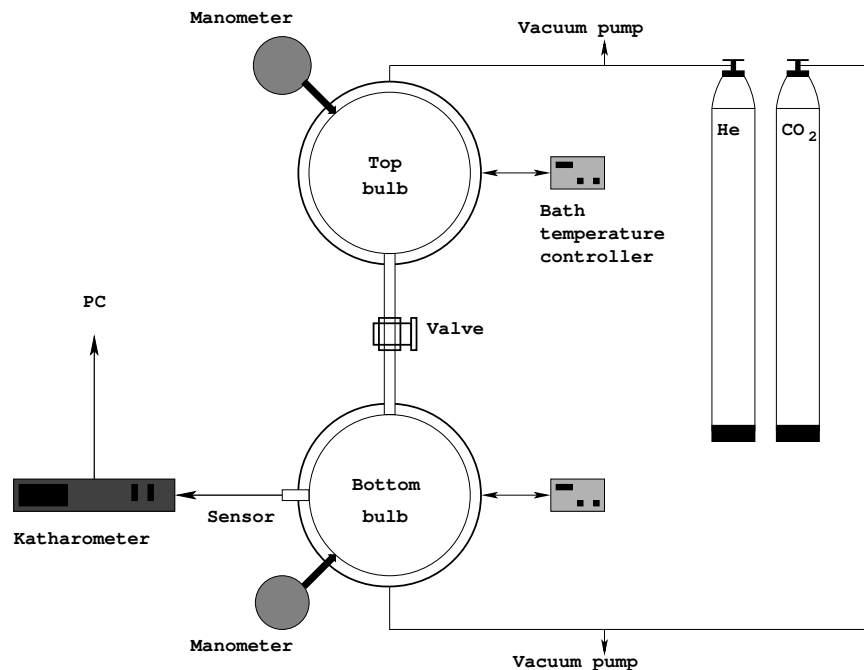


Figure 4.8: Sketch of the two-bulb experiment.

The inner diameter of the connecting tube is 0.795 cm and its total length is 13.87 cm (including the valve length). The bottom 4 cm is filled with the porous medium with particles between 200-210 μm diameter and porosity of 40.2%. At the beginning of the experiment, the valve is opened and the gases are mixed at a constant temperature of 300 K. After reaching steady-state ($x_{\text{He}}=x_{\text{CO}_2}=0.5$), the valve is closed and the temperature of the top bulb is increased to 350 K. Next, a small tap on the top bulb is opened to decrease the pressure until it reaches an equilibrium between the two bulbs. The thermal diffusion starts after the valve between the two bulbs is opened. This is a starting point for the numerical model. The model geometry and boundary conditions are the same as in the experiment. The system pressure is set to constant at 1 atm. The binary diffusion coefficient with the obstruction and thermal diffusion factors are set to the experimental values and are listed in Table 4.2. The permeability is calculated from Eqn. 2.2.13. Assuming the effective pore diameter of 205 μm , the resulting permeability is $\sim 4 \times 10^{-11} \text{ m}^2$.

D_{He,CO_2}	D_{effHe,CO_2}	$OF = \frac{D_{effHe,CO_2}}{D_{He,CO_2}}$	α_{TCO_2}
0.528	0.32	0.6	0.364

Table 4.2: Measured binary and effective diffusion coefficients for mixture of He- CO_2 and calculated obstruction and thermal diffusion factors.

The domain is discretized using unstructured mesh with a total of 112×10^3 nodes (Fig. 4.9).

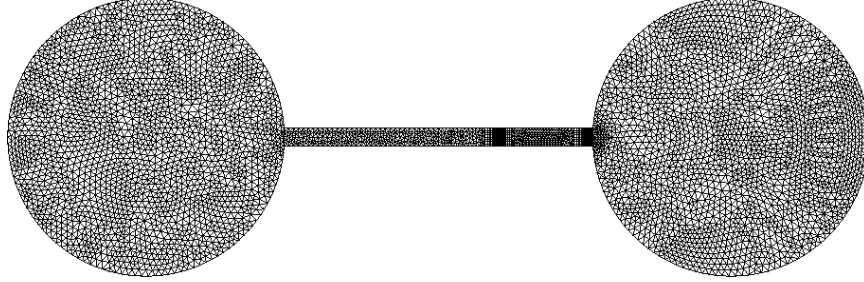


Figure 4.9: The two-bulb mesh.

The initial mass fraction is calculated using

$$\omega_\alpha = x_\alpha \frac{M_{w_\alpha}}{M_{w_{\alpha\beta}}} \quad (4.3.1)$$

where

$$M_{w_{\alpha\beta}} = x_\alpha M_{w_\alpha} + x_\beta M_{w_\beta} \quad (4.3.2)$$

and $x_\alpha = x_\beta = 0.5$.

The results of the simulation are shown in Fig. 4.10 along with those found in the experiment. Here one finds that, due to the effect of thermal diffusion, the concentration of CO_2 increases in the colder region. This is expected and is caused by the positive value of α_{TCO_2} . The results from the model are in good agreement with the experimental results. The error is less than 0.5%. This is within the range of a katharometer device used to analyze the

gas composition. It should be mentioned that, in the paper of Davarzani et al. [102], the thermal diffusion factor is obtained with respect to an average temperature and the effect of composition on $\alpha_{T_{CO_2}}$ is ignored. They also found that, the presence of a porous medium does not change the value of thermal diffusion factor. Therefore, $\alpha_{T_{CO_2}}$ is the same for a free medium and porous media. There is no available experimental data to validate the thermal diffusion for the mixture of H_2O-CO_2 under Mars conditions. Therefore, the previously described experimental results are used here only to validate the thermal diffusion implementation in CFD code. Since the results are in good agreement, there is no need for a finer mesh.

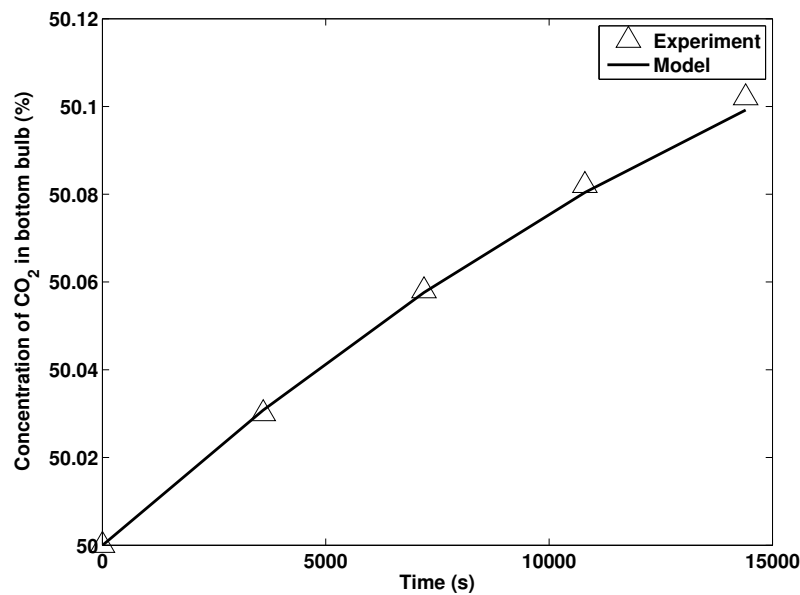


Figure 4.10: *The modelled (solid line) and experimental (triangles) results of thermal diffusion separation for He-CO₂ binary mixture.*

5

Numerical Simulations

In this chapter, results of the one- and two-dimensional models of the water cycle at the surface of Mars are presented. The one-dimensional simulations are summarized for two cases. The first is restricted to the transport by convection and ordinary diffusion only, i.e., neglecting thermal diffusion in the regolith. For the second case, the transport of water vapour is also determined by thermal diffusion. Results are discussed based on the observations from Sol 70 of the Phoenix mission and initial TECP measurement results from Zent et al. [15]. To demonstrate effects of the local topography a two-dimensional model is simulated in addition to the 1-D model.

5.1 One-Dimensional Model of Sol 70 of the Phoenix Mission

To simulate Sol 70 of the Phoenix mission, the same 1-D domain as discussed in section 4.1 is used. The ice temperature at the bottom of the regolith is set to the saturation temperature (213 K). The initial surface pressure and temperature are set to the observed 774 Pa and 241 K [103]. Inside the regolith, the temperature profile is assumed to be linear, which gives the best agreement with the predicted temperature profile (1700 LMST) by Zent et al. [15], for the same ice table depth. According to Whiteway et al. [55], the water vapour was well mixed throughout the boundary layer by the daytime turbulence and convection, so that in the late afternoon, the volume mixing ratio of water vapour was approximately constant up to a height of 4 km. They estimated this value to be 0.0014. The modelled atmospheric pressure at the surface is 774 Pa (Sol 70), which results in an initial water vapour pressure at the

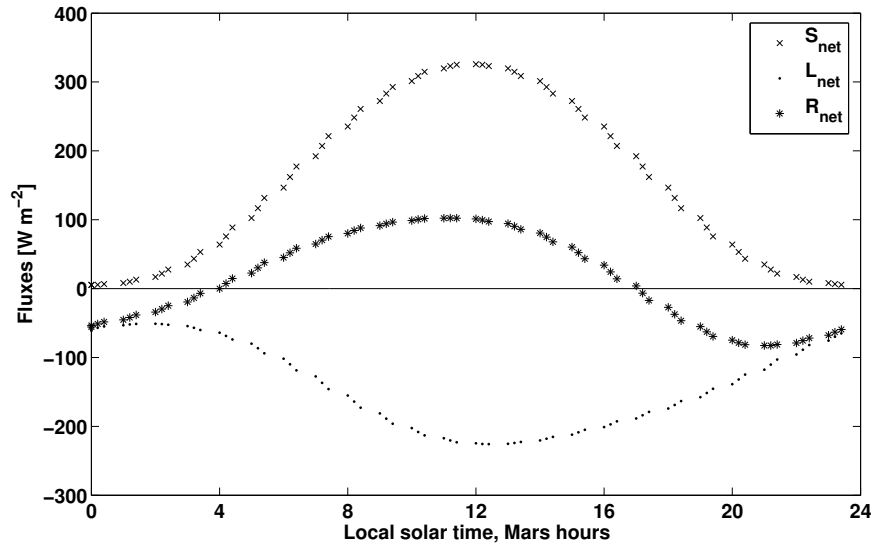


Figure 5.1: Surface energy fluxes calculated for Sol 70 of the Phoenix mission. S_{net} is the net solar irradiation flux, L_{net} is the net radiation from the ground, and R_{net} is the net radiation at the surface.

surface of 1.08 Pa. The critical relative humidity for the atmosphere domain is assumed to be 120%. Since the regolith is made up of many ice and dust particles, immediate condensation at 100% is assumed within that regolith.

Based on the TECP results from Zent et al. [15], the regolith thermal inertia is set to $280 \text{ J m}^{-2} \text{ s}^{-0.5} \text{ K}^{-1}$. Using the regolith material properties calculated in section 2.2 and effective porosity of 23% (Eqn. 2.2.29), the resulting thermal conductivity of the solid phase is $0.04 \text{ W m}^{-1} \text{ K}^{-1}$. The site surface albedo is set to 0.18 as in Savijärvi and Määttänen [38], and the optical depth is fixed to the observed 0.4 [62]. The calculated surface energy fluxes for the Sol 70 model are shown in Fig. 5.1. The R_{net} becomes positive after 0400 LT and at 0700 LT it is higher than 60 W m^{-2} .

Since the CO_2 is a participant gas, it emits and absorbs long wave radiation, cooling off during the night and heating up during the day. To avoid the huge complexity of this process, a highly simplified approach is implemented in the model. To get the desired effect of gradual cooling/heating a volumetric heat

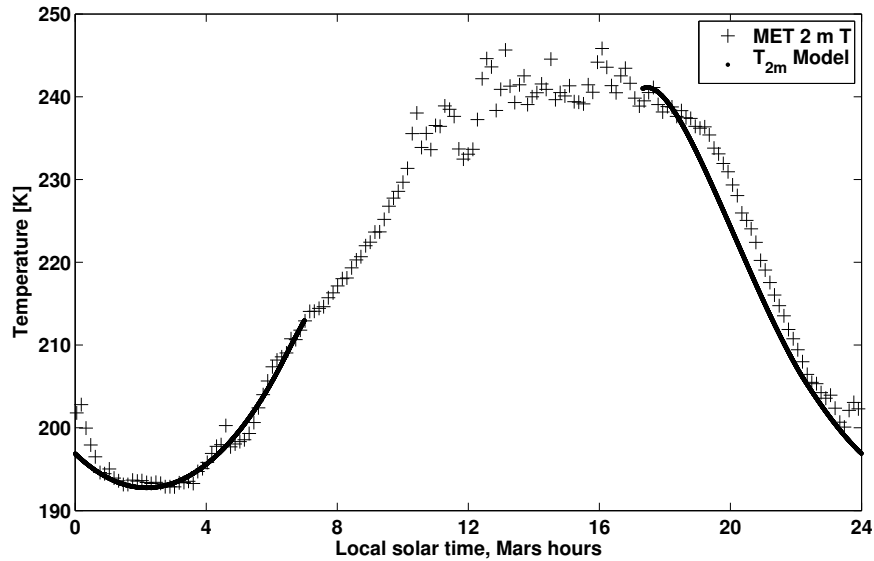


Figure 5.2: Observed 2 m (points) and modelled 2 m (solid line) temperatures for Sol 70 of the Phoenix mission.

sink/source is applied to the atmosphere domain. The value of this sink has been adjusted in such a way that the temperature at 2 m matches observations. The results are shown in Fig. 5.2. For computational reasons, only the period from 17 to 07 LT (overnight) is modelled since, during the daytime, complicating effects of thermal plumes and turbulent winds are present.

Results of one-dimensional simulations of Sol 70 of the Phoenix mission are shown in figures 5.3-5.10. Figures 5.3-5.4 illustrate the atmosphere and the regolith temperature profiles at 17, 20, 22, 01, 04, and 06 LT. During late afternoon (17 LT) the atmosphere is well-mixed and the temperature profiles display nearly constant values of T . The air then cools down due to radiative cooling, where it reaches the night-time minimum (at 01 LT) of 192 K at the ground. At 04 LT, the net radiation flux at the surface becomes positive, which results in a surface temperature inversion in the LT04 and LT06 profiles. The maximum temperature difference between the top surface of the regolith and

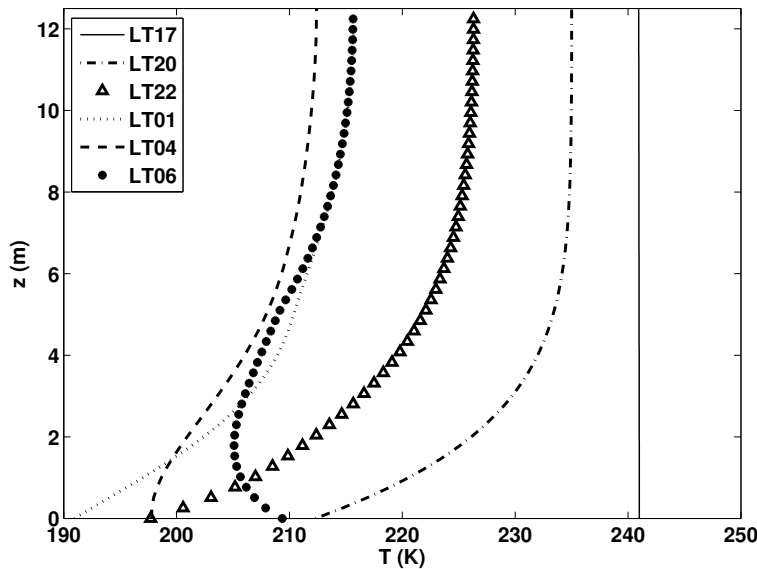


Figure 5.3: *The atmosphere temperature profiles at 17, 20, 22, 01, 04, and 06 LT during the Sol 70 simulations.*

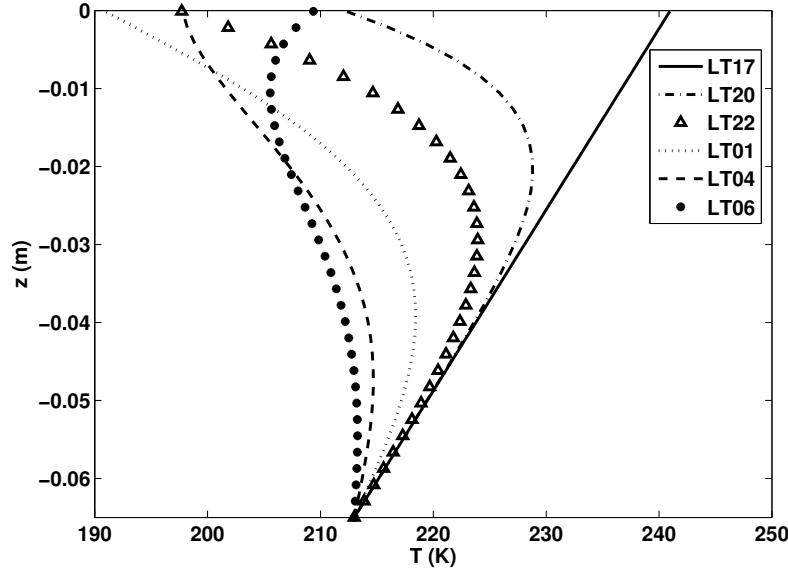


Figure 5.4: *The regolith temperature profiles at 17, 20, 22, 01, 04, and 06 LT during the Sol 70 simulations.*

the ice table is on the order of 30 K (Fig. 5.4).

Fig. 5.5 shows the model’s relative humidities. The rapid increase of relative humidity in the evening, due to the falling temperatures, leads to saturation. At about 20 LT the ground has reached the frost point and weak ground frost formation takes place in the model. At this time a sharp decrease in atmospheric H_2O was observed by Phoenix [4]. The frost formation on the ground removes water vapour from the atmosphere, as shown in Fig. 5.6, but the cooling is so strong that the critical humidity of 120% is reached at 2 m height at 2230 LT, and at 7 m height at 0300 LT (not shown). The fog growth removes more water from the sub-saturated regions. Close to the surface the water vapour in the model remains saturated throughout the night and reaches a minimum value of ~ 0.05 Pa between 00 and 02 LT. This is in agreement with the TECP measurements from the Phoenix mission [4]. Soon after sunrise (04 LT) the existing fog sublimates back to vapour due to solar heating (Fig.

CHAPTER 5: NUMERICAL SIMULATIONS

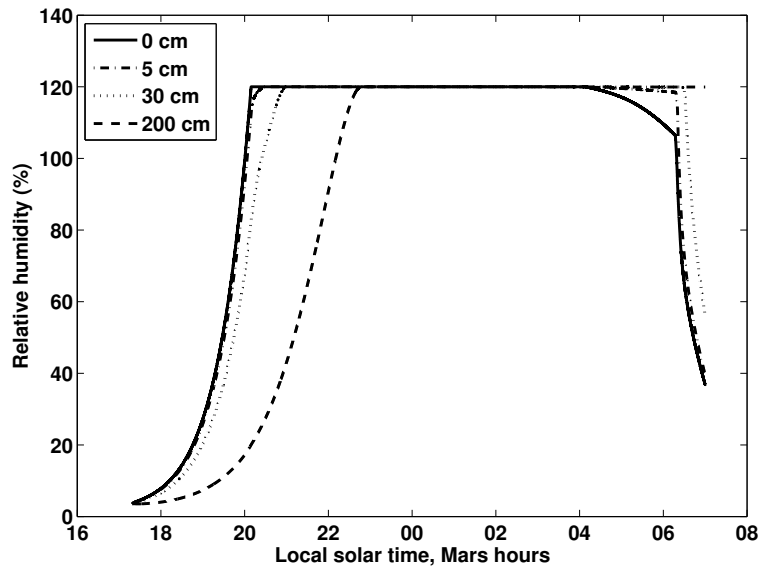


Figure 5.5: *Modelled relative humidity at different heights for Phoenix sols 70 to 71.*

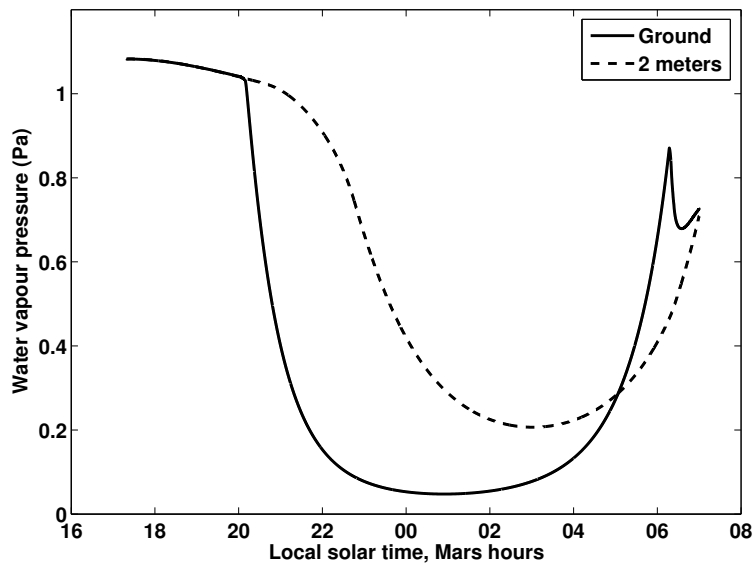


Figure 5.6: *Modelled water vapour pressure at the ground (solid) and at 2 m above the ground (dashed) for Phoenix sols 70 to 71.*

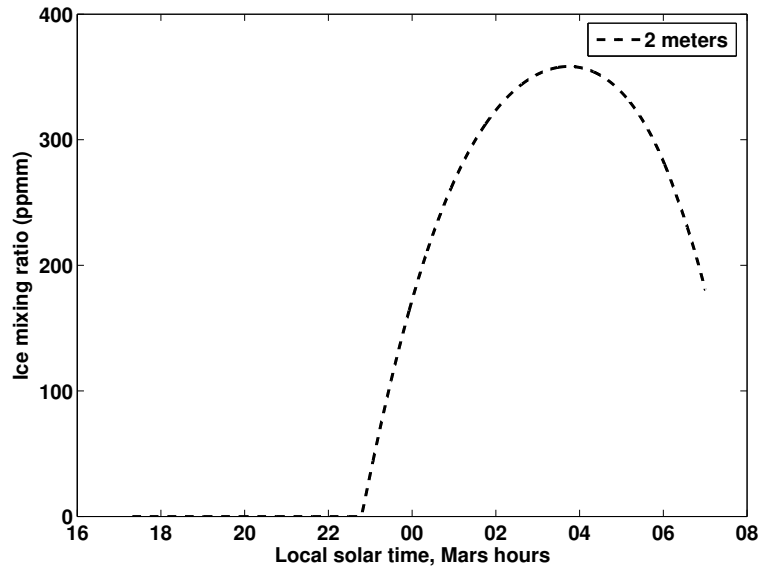


Figure 5.7: Modelled water ice mixing ratio at 2 m above the ground for *Phoenix* sols 70 to 71.

5.7). The temperature of the atmosphere is low enough for fog to be present until about 07 LT¹. With solar heating in the morning, the vapour pressure increases in the atmosphere and relative humidity decreases rapidly near the ground. This demonstrates that most of the ice accumulated at the surface during the night sublimates and diffuses back into the atmosphere by 07 LT.

Fig. 5.8 shows that ice deposition in the regolith does not begin until 04 LT (since the downward movement of the ground thermal wave is slow). Temperature decline deep in the regolith leads to saturation, and then results in a temporary flux of vapour from the atmosphere to the ground. This explains a small instability in vapour pressure at 06 LT (Fig. 5.6) at the regolith surface. With stronger heating after 06 LT, the surface is rapidly warming, which increases the sublimation and replenishes the moisture field in the atmosphere.

¹In this study, the simulations end at 07 LT but from results in Fig. 5.7 the inference is that fog may stay until 08 LT.

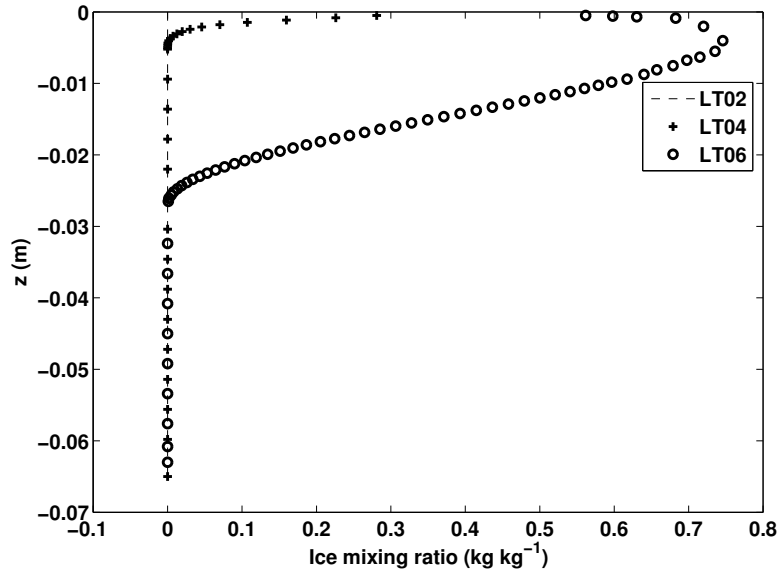


Figure 5.8: *The regolith ice mixing ratio profiles at 02, 04, and 06 LT during the Sol 70 simulations.*

5.1.1 Effect of Thermal Diffusion

Next, the same model was run with an additional source term, which accounts for the effect of thermal diffusion. Here, only the most significant differences between the two models are presented. Fig. 5.9 shows the water vapour mixing ratio at 5 cm above the ground for both models. At 17 LT the atmosphere is well-mixed and the initial water vapour mixing ratio is ~ 574 ppm. For the case with thermodiffusion, the reduction in atmospheric water vapour begins just after the simulation is started, even though the regolith and atmospheric temperatures are both well above the frost point. While for the non-thermodiffusion case there is no change in the mixing ratio prior to saturation. Fig. 5.10 illustrates time averaged water vapour fluxes across a horizontal surface at 5 cm above the ground for the period from 17 to 23 LT. The time average is taken every 15 min. Since at 17 LT the vapour concentration in the soil is in equilibrium with the atmospheric vapour there is no

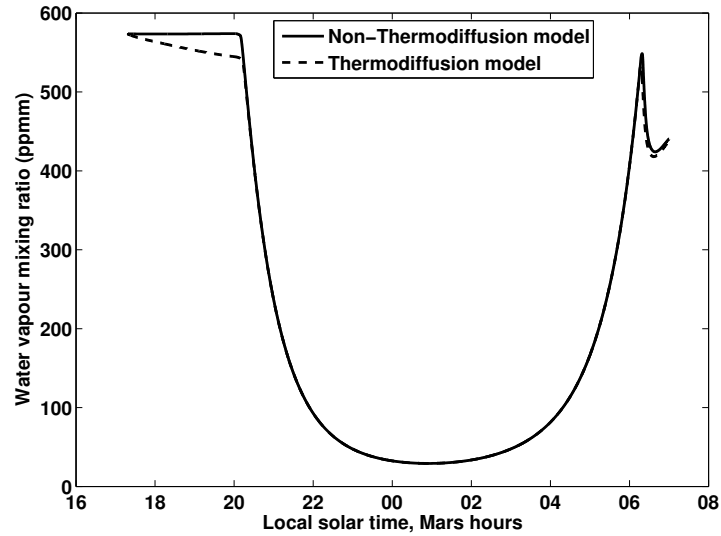


Figure 5.9: Modelled water vapour mixing ratio at 5 cm above the ground for thermodiffusion (dashed) and non-thermodiffusion (solid) case.

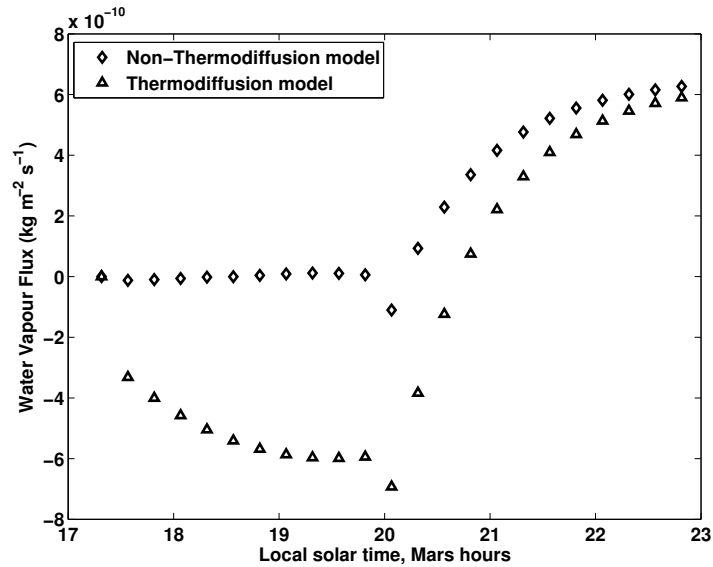


Figure 5.10: Total average water vapour fluxes across a horizontal surface at 5 cm above the ground for thermodiffusion (triangles) and non-thermodiffusion (diamonds) case.

significant flux crossing the surface. However, there is additional transport of water which results from the thermal diffusion. The direction of the flux indicates the mass transport of atmospheric water down to the regolith. This is expected since the thermal diffusion factor for H_2O is positive and the temperature is decreasing downwards (as shown in Fig. 5.11). Recall from section 2.2.3 that for positive α_{T_α} , species α moves toward the colder region.

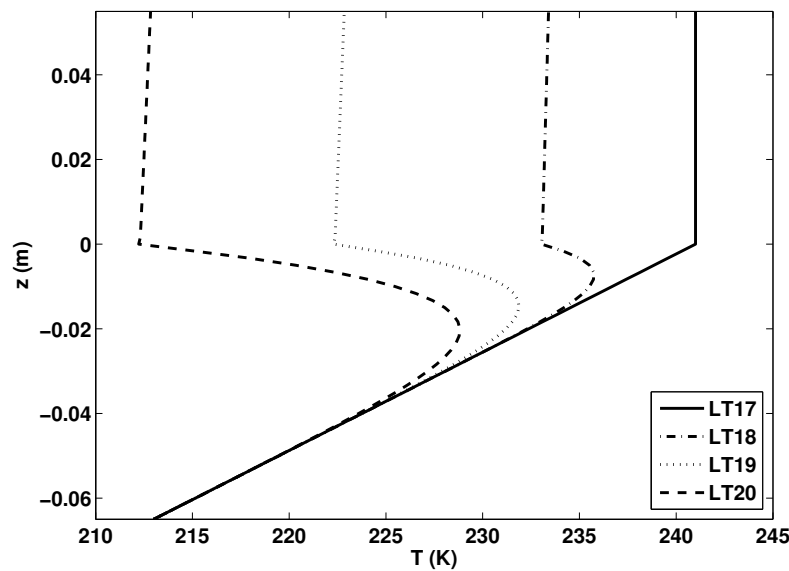


Figure 5.11: *The regolith and near-surface temperature profiles at 17, 18, 19, and 20 LT during the Sol 70 simulations.*

5.2 Two-Dimensional Model of Sol 70 of the Phoenix Mission

In this work 2-D effects are demonstrated using a simple slope with the angle of inclination γ . The angle is given by $\tan(\gamma) = 1/2$, and is measured counterclockwise from the part of the horizontal axis to the right of the line. If the

hour angle is zero ($\gamma_h = 0$) at noon, then $\gamma = 26.565^\circ$, which gives about 1 hr 46 min shift in R_{net} . This can cause a difference in local surface temperature and it may contribute to more or less intensive water vapour exchange between the atmosphere and the regolith. It can also affect the time of frost occurrence and its amount in the regolith.

The computational domain is divided into the atmosphere and the regolith part. The atmosphere part is 1250 cm high and the regolith depth is variable from minimum 4 to maximum 11.5 cm. The domain is 100 cm wide and 1 cm thick in the symmetry direction. It is discretized using structured hexahedral mesh with a total of approximately 50k nodes. The grid size systematically increases from very fine control volumes in the regolith and at the bottom of the atmosphere, to coarser control volumes at the top. Such refinement is possible using inflated layers at the domain interface. Here the first layer thickness is 0.18 mm (Fig. 5.12).

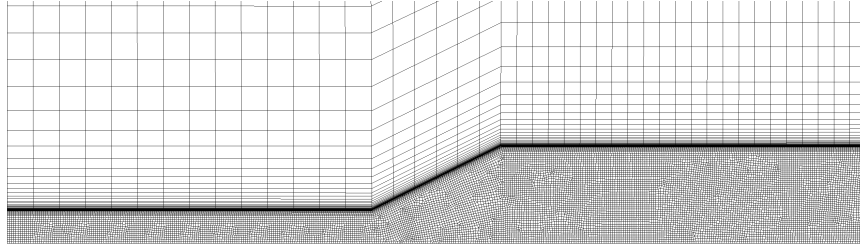


Figure 5.12: *View of the structured hexahedral mesh with local refinement used for 2-D simulations.*

Free slip adiabatic boundary conditions are used at the top and side surfaces. The front and back walls are considered symmetry boundaries. At the bottom of the regolith, a no-slip wall with a constant ice temperature of 213 K is applied. At the atmosphere-solid interface, conservative flux for all transport variables is prescribed and two different energy fluxes are applied for horizontal and inclined surfaces, corresponding to the distinct radiation loads. The initial conditions are the same as for the 1-D case. 120% critical relative humidity is

assumed for both the regolith and atmosphere domain.

Results of the two-dimensional model are illustrated in figures 5.13-5.16. The reduction in water vapour pressure at 2 m above the ground begins before 20 LT (as shown in Fig. 5.13). Saturation is first reached at the slope due to the higher cooling rate at this region. This is expected and is caused from lower values of R_{net} , which is applied at the inclined surface. Fig. 5.14 shows temperature and relative humidity contours in the domain just after the surface has reached the frost point ($RH=120\%$). Here only 1.2 m of the atmosphere

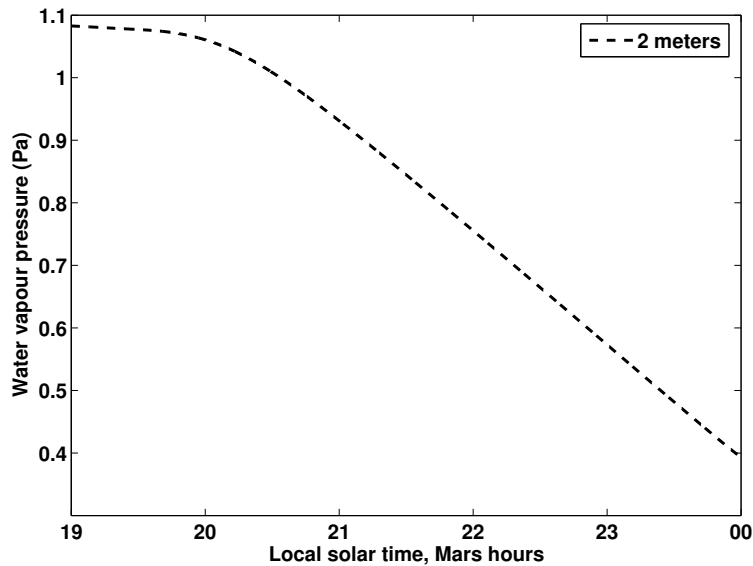


Figure 5.13: *Modelled water vapour pressure at 2 m above the ground.*

domain is shown, although its total height is 12.5 m. When the near-surface air gets saturated with respect to H_2O ice, surface frost is formed. Fig. 5.15 illustrates frost formation and fog evolution in the domain. Deposition of water vapour initially begins at the slope. Then water vapour from adjacent regions of the ground and atmosphere diffuses to the surface where it condenses as ice. Fig. 5.16 shows how the moisture is transported to the near-surface. Cool air above the inclination is more dense than warm air at the lower level so it falls

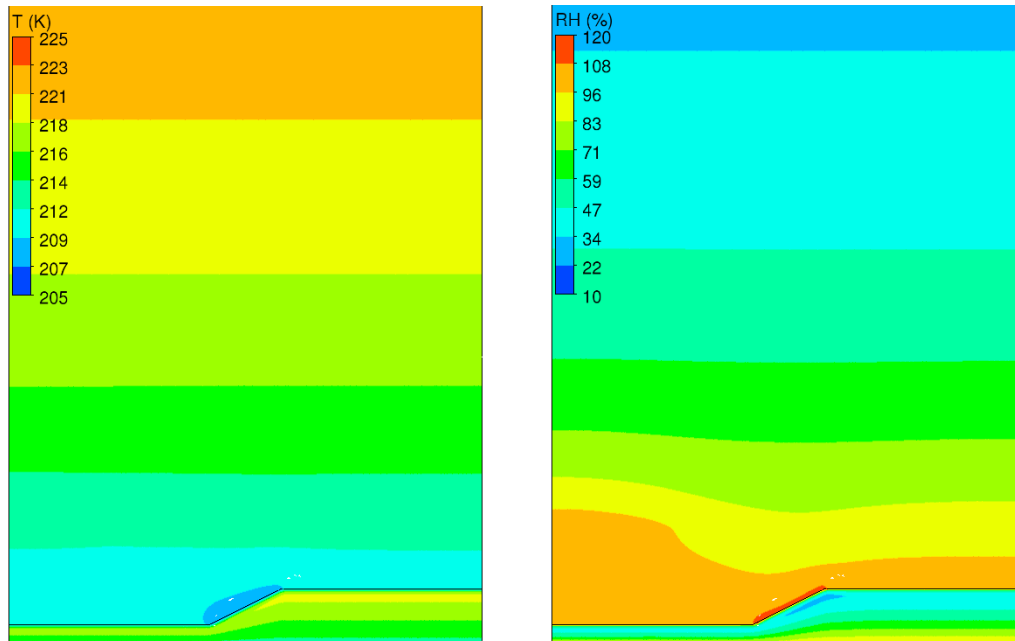


Figure 5.14: *Temperature (left) and relative humidity (right) contours at 1930 LT.*

through the warmer air and it results in a down-slope convective transport. When moist air travels over colder regions, it cools by heat conduction to the surface and saturation occurs. This preferential deposition is typical, e.g., in the shadow of large rocks [104]. As the cooling is getting stronger, the layers of air above the surface also cool below their saturation point leading to the formation of fog. Overnight more frost accumulates on the surface and in the regolith. With solar heating in the morning (not simulated with 2-D model), frost is expected to sublimate, as it does in the 1-D model.

CHAPTER 5: NUMERICAL SIMULATIONS

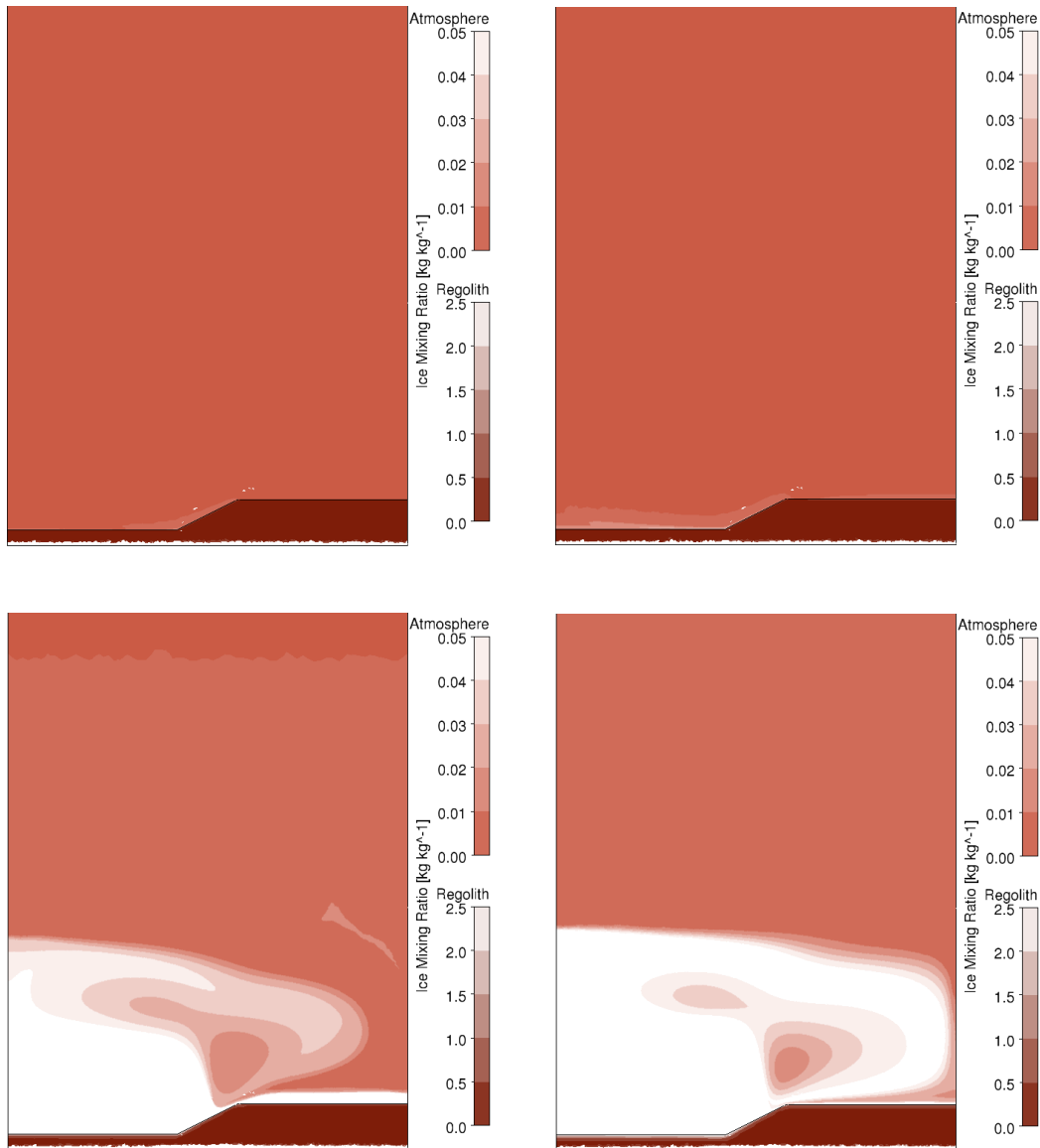


Figure 5.15: Fog contours at 1925 LT (top left), 1930 LT (top right), 2200 LT (bottom left), and 2300 LT (bottom right).

CHAPTER 5: NUMERICAL SIMULATIONS

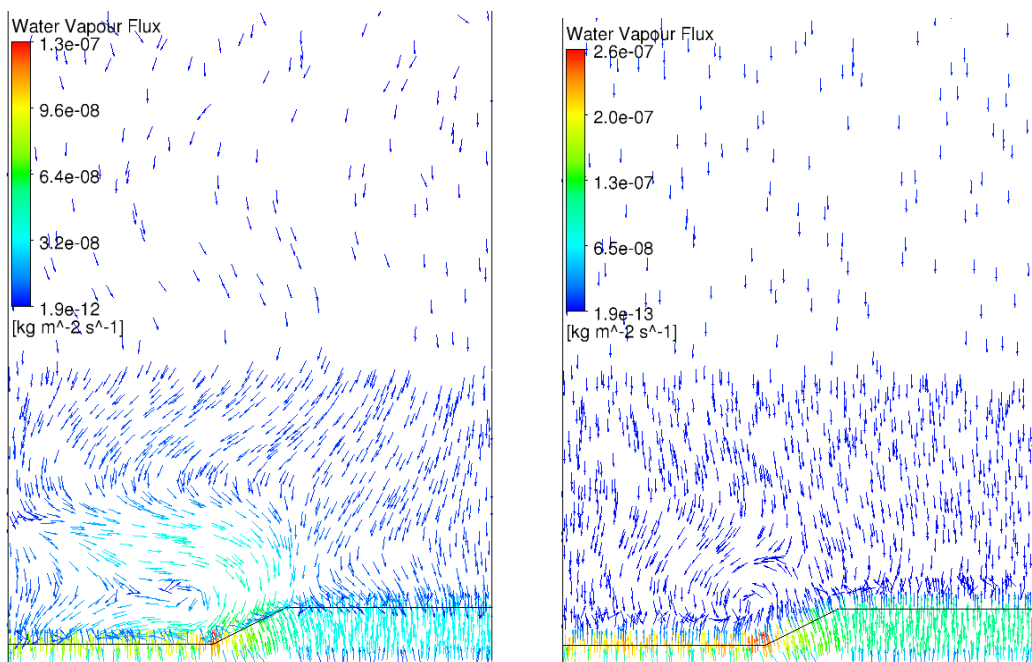


Figure 5.16: *Near-surface water vapour flux vectors at 1930 LT (left) and 2200 LT (right).*

6

Conclusions

6.1 Summary

In this study, the diurnal cycle of water across the surface of Mars was simulated. The simulations implement fog formation in the atmosphere and frost deposition on the surface and in the regolith. The diffusion of water vapour in the ground is treated for Knudsen and thermal diffusion effects. A simple surface radiation model is implemented to model the surface temperature. The main goal of this implementation was a fully functional, two-dimensional model with the source terms that count for the mass and heat transfer between the gaseous and solid phases and for the transfer of gas caused by a

temperature gradient. An important point of the demonstration cases are the meteorological data transmitted from the Phoenix mission. Based on these data, the models have been setup using the properties at the time, when the temperatures of saturation, condensation and freezing of water vapour are expected to be reached. Numerical simulations of the evening hours of Sol 70 confirmed that under such conditions a deposition of water vapour can exist on Mars. The results show how phase change occurred right after the temperature of air is cooled down below the frost point and deposited on the surface as frost. The rapid increase of vapour pressure during the morning hours indicates that sublimation and convection drive the moisture correctly back into the atmosphere. Results of the two-dimensional model show that there are always considerable spatial fluctuations of the fog structure for which variations in the nature and slope of the local terrain are at least partly responsible. The most important contribution of the present work is that thermal gradients in the regolith are large enough that thermal diffusion of water vapour toward the ice table is significant at certain times.

The presented model has been successfully validated and verified, therefore it may be used in the future for modelling and interpretation of orbital data far from the Phoenix site. It may help to find sites with more frequent heat and water exchange where chances for liquid water are higher.

6.2 Future Investigations

Development of the model of water cycle on Mars is a continuous task. The existing model should be improved to include the full spatial variability of the thermophysical quantities that represent arbitrary configurations of rocks, ice, and different soil types in the subsurface. A fully three-dimensional treatment of the surface is obviously necessary for realistic wind simulations, but this may require the use of open source code, which would allow access to more

CHAPTER 6: CONCLUSIONS

powerful computers. With more computational power, the model can be also initialized with zero water vapour in the atmosphere and run until temperature and humidity profiles does not change from sol to sol. Having the actual initial profiles would give better estimation of H₂O reduction in the atmosphere and higher accuracy of the results.

Since the atmosphere of Mars is composed mainly of carbon dioxide (95.32%), which molecules are large enough for absorbing and emitting the solar radiation, a full radiation model is also desirable. It might result in better radiative cooling of the air itself and could investigate the radiative effects of fog near the surface. It has been suggested by Roach et al. [105] that the radiative effects of a ground fog on Earth can lead to major temperature changes within the condensing region.

Future studies will employ more physical processes such as adsorption or effects of perchlorate brine at the bed of the ice table. Laboratory measurements of the adsorption of CO₂ and H₂O indicate that pulverized basalt has an extremely high internal surface area [106]. This suggests that a substantial amount of H₂O might be adsorbed by the Martian regolith and remains there as interfacial water due to attractive van der Waals interactions at ice-mineral interfaces [7]. Similar effects were observed on Earth in sub-zero temperature soils. Additionally, due to formation of brines, which can remarkably widen the range of temporary liquid water, the adsorbed water can remain mobile at temperatures down to 200 K [105].

Finally, direct thermodiffusion measurements would be the most valuable in order to determinate the force constants between H₂O and CO₂ molecules, especially at low pressures and temperatures as those on Mars. This would give better accuracy when modelling thermal diffusion of water vapour in the Martian regolith. The present effort however, is believed to be useful for future CFD calculations in water cycle studies on Mars. The current approach and suitable formulas are easy to implement in existing numerical codes.

References

- [1] R. Span and W. Wagner. A new equation of state for carbon dioxide covering the fluid region from the triple-point temperature to 1100 K at pressures up to 800 MPa. *J. Phys. Chem. Ref. Data*, 25:1509–1596, 1996.
- [2] W. T. Parry. *ASME international steam tables for industrial use : based on the IAPWS Industrial Formulation 1997 for the Thermodynamic Properties of Water and Steam (IAPWS-IF97)*. American Society of Mechanical Engineers, New York, NY., 2 edition, 2009.
- [3] V. A. Krasnopolsky. Photochemistry of the martian atmosphere: Seasonal, latitudinal, and diurnal variations. *Icarus*, 185(1):153–170, 2006.
- [4] A. P. Zent, M. C. Hecht, D. R. Cobos, S. E. Wood, T. L. Hudson, S. M. Milkovich, L. P. DeFlores, and M. T. Mellon. Initial results from the thermal and electrical conductivity probe (TECP) on Phoenix. *J. Geophys. Res.*, 115: E00E14, 2010.
- [5] R. L. Levin and J. L. Weatherwax. Liquid water on Mars. volume 3446, pages 145–157, 2004.
- [6] G. M. Marion, D. C. Catling, K. J. Zahnle, and M. W. Claire. Modeling aqueous perchlorate chemistries with applications to Mars. *Icarus*, 207(2): 675–685, 2009.
- [7] D. Möhlmann. The three types of liquid water in the surface of present Mars. *International Journal of Astrobiology*, 9(01):45–49, 2010.
- [8] M. H. Hecht, S. P. Kounaves, R. C. Quinn, S. J. West, S. M. M. Young, D. W. Ming, D. C. Catling, B. C. Clark, W. V. Boynton, J. Hoffman, L. P. DeFlores,

REFERENCES

- K. Gospodinova, J. Kapit, and P. H. Smith. Detection of perchlorate and the soluble chemistry of Martian soil at the Phoenix Lander Site. *Science*, 325(5936):64–67, 2009.
- [9] O. N. Pestova, L. A. Myund, M. K. Khripun, and A. V. Prigaro. Polythermal study of the systems $M(\text{ClO}_4)_2\text{-H}_2\text{O}$ ($M^{2+} = \text{Mg}^{2+}, \text{Ca}^{2+}, \text{Sr}^{2+}, \text{Ba}^{2+}$). *Rus. J. App. Chem.*, 78(3):409–413, 2005.
- [10] P. A. Taylor, D. C. Catling, M. Daly, C. S. Dickinson, H. P. Gunnlaugsson, A. Harri, and C. F. Lange. Temperature, pressure, and wind instrumentation in the Phoenix meteorological package. *J. Geophys. Res.*, 113:E00A10, 2008.
- [11] J. Whiteway, M. Daly, A. Carswell, T. Duck, C. Dickinson, L. Komguem, and C. Cook. Lidar on the Phoenix mission to Mars. *J. Geophys. Res.*, 113:E00A08, 2008.
- [12] J. E. Moores, L. Komguem, J. A. Whiteway, M. T. Lemmon, C. Dickinson, and F. Daerden. Observations of near-surface fog at the Phoenix Mars Landing Site. *Geophys. Res. Lett.*, 38(L04203):1–6, 2011.
- [13] J. E. Moores, M. T. Lemmon, P. H. Smith, L. Komguem, and J. A. Whiteway. Atmospheric dynamics at the Phoenix landing site as seen by the Surface Stereo Imager. *J. Geophys. Res.*, 115:E00E08, 2010.
- [14] J. F. Bell III, S. W. Squyres, K. E. Herkenhoff, J. N. Maki, H. M. Arneson, D. Brown, S. A. Collins, A. Dingizian, S. T. Elliot, E. C. Hagerott, A. G. Hayes, M. J. Johnson, J. R. Johnson, J. Joseph, K. Kinch, M. T. Lemmon, R. V. Morris, L. Scherr, M. Schwochert, M. K. Shepard, G. H. Smith, J. N. Sohl-Dickstein, R. J. Sullivan, W. T. Sullivan, and M. Wadsworth. Mars Exploration Rover Athena Panoramic Camera (Pancam) investigation. *J. Geophys. Res.*, 108(E12)(8063), 2003.
- [15] A. P. Zent, M. H. Hecht, D. R. Cobos, G. S. Campbell, C. S. Campbell, G. Cardell, M. C. Foote, S. E. Wood, and M. Mehta. Thermal and Electrical Conductivity Probe (TECP) for Phoenix. *J. Geophys. Res.*, 114:E00A27,

REFERENCES

- 2009.
- [16] P. A. Taylor, H. Kahanpää, W. Weng, A. Akingunola, C. Cook, M. Daly, C. Dickinson, A. Harri, D. Hill, V. Hipkin, J. Polkko, and J. Whiteway. On pressure measurement and seasonal pressure variations during the Phoenix mission. *J. Geophys. Res.*, 115:E00E15, 2010.
- [17] R. Davy, J. A. Davis, P. A. Taylor, C. F. Lange, W. Weng, J. Whiteway, and H. P. Gunnlaugson. Initial analysis of air temperature and related data from the Phoenix MET station and their use in estimating turbulent heat fluxes. *J. Geophys. Res.*, 115:E00E13, 2010.
- [18] S. M. Nelli, N. O. Renno, J. R. Murphy, W. C. Feldman, and S. W. Bougher. Simulations of atmospheric phenomena at the Phoenix landing site with the Ames General Circulation Model. *J. Geophys. Res.*, 115:E00E21, 2010.
- [19] M. C. Malin and K. S. Edgett. Fossil fans in Melas Chasma, 2007.
- [20] S. W. Squyres, R. E. Arvidson, J. F. Bell, J. Brckner, N. A. Cabrol, W. Calvin, M. H. Carr, P. R. Christensen, B. C. Clark, L. Crumpler, D. J. Des Marais, C. d’Uston, T. Economou, J. Farmer, W. Farrand, W. Folkner, M. Golombek, S. Gorevan, J. A. Grant, R. Greeley, J. Grotzinger, L. Haskin, K. E. Herkenhoff, S. Hviid, J. Johnson, G. Klingelhfer, A. H. Knoll, G. Landis, M. Lemmon, R. Li, M. B. Madsen, M. C. Malin, S. M. McLennan, H. Y. McSween, D. W. Ming, J. Moersch, R. V. Morris, T. Parker, J. W. Rice, L. Richter, R. Rieder, M. Sims, M. Smith, P. Smith, L. A. Soderblom, R. Sullivan, H. Wnke, T. Wdowiak, M. Wolff, and A. Yen. The Opportunity Rover’s athena science investigation at Meridiani Planum, Mars. *Science*, 306(5702):1698–1703, 2004.
- [21] J.-P. Bibring, Y. Langevin, A. Gendrin, B. Gondet, F. Poulet, M. Berth, A. Soufflot, R. Arvidson, N. Mangold, J. Mustard, P. Drossart, and the OMEGA team. Mars surface diversity as revealed by the OMEGA/Mars Express observations. *Science*, 307(5715):1576–1581, 2005.

REFERENCES

- [22] A. Gendrin, N. Mangold, J.-P. Bibring, Y. Langevin, B. Gondet, F. Poulet, G. Bonello, C. Quantin, J. Mustard, R. Arvidson, and S. LeMoulic. Sulfates in martian layered terrains: The OMEGA/Mars Express view. *Science*, 307(5715):1587–1591, 2005.
- [23] W. V. Boynton, D. W. Ming, S. P. Kounaves, S. M. M. Young, R. E. Arvidson, M. H. Hecht, J. Hoffman, P. B. Niles, D. K. Hamara, R. C. Quinn, P. H. Smith, B. Sutter, D. C. Catling, and R. V. Morris. Evidence for calcium carbonate at the Mars Phoenix landing site. *Science*, 325(5936):61–64, 2009.
- [24] P. H. Smith, L. K. Tamppari, R. E. Arvidson, D. Bass, D. Blaney, W. V. Boynton, A. Carswell, D. C. Catling, B. C. Clark, T. Duck, E. DeJong, D. Fisher, W. Goetz, H. P. Gunnlaugsson, M. H. Hecht, V. Hipkin, J. Hoffman, S. F. Hviid, H. U. Keller, S. P. Kounaves, C. F. Lange, M. T. Lemmon, M. B. Madsen, W. J. Markiewicz, J. Marshall, C. P. McKay, M. T. Mellon, D. W. Ming, R. V. Morris, W. T. Pike, N. Renno, U. Staufer, C. Stoker, P. Taylor, J. A. Whiteway, and A. P. Zent. H₂O at the Phoenix Landing Site. *Science*, 325: 58–61, 2009.
- [25] H. Spinrad, L. D. Kaplan, and G. Munch. The detection of water vapor on Mars. *Astrophys. J.*, 137(4):1319–1321, 1963.
- [26] F. M. Flasar and R. M. Goody. Diurnal behaviour of water on Mars. *Planetary and Space Science*, 24(2):161–181, 1976.
- [27] S. L. Hess. The vertical distribution of water vapor in the atmosphere of Mars. *Icarus*, 28(2):269–278, 1976.
- [28] D. Davies. The vertical distribution of Mars water-vapor. *J. Geophys. Res.*, 84:2875–2879, 1979.
- [29] J. A. Ryan, R. D. Sharman, and R. D. Lucich. Mars water vapor, near-surface. *J. Geophys. Res.*, 87(C9):7279–7284, 1982.
- [30] H. Savijärvi. Mars boundary layer modeling: Diurnal moisture cycle and soil properties at the Viking Lander 1 Site. *Icarus*, 117(1):120–127, 1995.

REFERENCES

- [31] D. T. F. Möhlmann, M. Niemand, V. Formisano, H. Savijärvi, and P. Wolkenberg. Fog phenomena on Mars. *Planetary and Space Science*, 57(14-15):1987–1992, 2009.
- [32] B. M. Jakosky and R. M. Haberle. *The seasonal behavior of water on Mars*. University of Arizona Press, Tucson, 1992.
- [33] A. P. Zent, R. M. Haberle, H. C. Houben, and B. M. Jakosky. A coupled subsurface-boundary layer model of water on Mars. *J. Geophys. Res.*, 98(E2):3319–3337, 1993.
- [34] B. M. Jakosky, A. P. Zent, and R. W. Zurek. The Mars water cycle: Determining the role of exchange with the regolith. *Icarus*, 130(1):87–95, 1997.
- [35] A. D. Toigo, M. I. Richardson, S. P. Ewald, and P. J. Gierasch. Numerical simulation of Martian dust devils. *J. Geophys. Res.*, 108(E6):5047, 2003.
- [36] D. R. Wing and G. L. Austin. Description of the University of Auckland global Mars mesoscale meteorological model. *Icarus*, 185:370–382, 2006.
- [37] J. Kauhanen, T. Siili, S. Järvenoja, and H. Savijärvi. The Mars limited area model and simulations of atmospheric circulations for the Phoenix landing area and season of operation. *J. Geophys. Res.*, 113:E00A14, 2008.
- [38] H. Savijärvi and A. Määttä. Boundary-layer simulations for the Mars Phoenix lander site. *Q. J. R. Meteorol. Soc.*, 136(1):1497–1505, 2010.
- [39] H. Houben, R. M. Haberle, R. E. Young, and A. P. Zent. Modeling the Martian seasonal water cycle. *J. Geophys. Res.*, 102(E4):9069–9083, 1997.
- [40] M. T. Mellon and B. M. Jakosky. Geographic variations in the thermal and diffusive stability of ground ice on Mars. *J. Geophys. Res.*, 98(E2):3345–3364, 1993.
- [41] N. Schorghofer and O. Aharonson. Stability and exchange of subsurface ice on Mars. *J. Geophys. Res.*, 110:E05003, 2005.

REFERENCES

- [42] T. L. Hudson, O. Aharonson, N. Schorghofer, B.C. Farmer, M. H. Hecht, and N. T. Bridges. Water vapor diffusion in Mars subsurface environments. *J. Geophys. Res.*, 112:E05016, 2007.
- [43] J. A. Beattie and S. Ikehara. An equation of state for gas mixtures. II. A study of the methods of combination of the constants of the Beattie-Bridgeman equation of state. *Proceedings of the American Academy of Arts and Sciences*, 64(7):127–176, 1930.
- [44] Y. A. Cengel and A. M. Boles. *Thermodynamics: An Engineering Approach*. McGraw-Hill College, 4 edition, 2002. p.89.
- [45] C. L. Yaws, editor. *Chemical Properties Handbook*, chapter Viscosity of Gas, pages 452–453. Mc Graw-Hill, 1999c.
- [46] C. L. Yaws, editor. *Chemical Properties Handbook*, chapter Thermal Conductivity of Gas, pages 505–506. Mc Graw-Hill, 1999b.
- [47] C. L. Yaws, editor. *Chemical Properties Handbook*, chapter Heat Capacity of Gas, pages 30–31. Mc Graw-Hill, 1999a.
- [48] J. F. Crifo. Inferences concerning water vapour viscosity and mean free path at low temperatures. *Astron. Astrophys.*, 223:365–368, 1989.
- [49] A. Eucken. *Physik. Z.*, 14:324–333, 1913.
- [50] R. B. Bird, W. E. Stewart, and E. N. Lightfoot. *Transport Phenomena*. John Wiley and Sons, Inc., 2 edition, 2001.
- [51] J. O. Hirschfelder, Ch. F. Curtis, and R. B. Bird. *Molecular Theory of Gases and Liquids*. John Wiley and Sons, Inc., NY, 2 edition, 1964.
- [52] L. Monchick and E. A. Mason. Transport properties of polar gases. *J. Chem. Phys.*, 35(5):1676–1697, 1961.
- [53] A. L. Buck. New equation for computing vapor pressure and enhancement factor. *J. Appl. Meteorol.*, 20:1527–1532, 1981.

REFERENCES

- [54] R. J. List. *Smithsonian Meteorological Tables*. Smithsonian Institution, Washington, DC, 6 edition, p. 343, 1949.
- [55] J. A. Whiteway, L. Komguem, C. Dickinson, C. Cook, M. Illnicki, J. Seabrook, V. Popovici, T. J. Duck, R. Davy, P. A. Taylor, J. Pathak, D. Fisher, A. I. Carswell, M. Daly, V. Hipkin, A. P. Zent, M. H. Hecht, S. E. Wood, L. K. Tamppari, N. Renno, J. E. Moores, M. T. Lemmon, F. Daerden, and P. H. Smith. Mars water-ice clouds and precipitation. *Science*, 325(5936):68–70, 2009.
- [56] A. A. Tsonis. *An Introduction to Atmospheric Thermodynamics*. Cambridge University Press, 2002.
- [57] P. R. Field, O. Möhler, P. Connolly, M. Krämer, R. Cotton, A. J. Heymsfield, H. Saathoff, and M. Schnaiter. Some ice nucleation characteristics of Asian and Saharan desert dust. *Atmos. Chem. Phys.*, 6(10):2991–3006, 2006.
- [58] A. Määttänen, H. Vehkamäki, A. Lauri, S. Merikallio, J. Kauhanen, H. Savijärvi, and M. Kulmala. Nucleation studies in the Martian atmosphere. *J. Geophys. Res.*, 110:E02002, 2005.
- [59] E. W. Washburn, editor. *International Critical Tables of Numerical Data, Physics, Chemistry and Technology (1st Electronic Edition)*, volume V, ebook Interdiffusion of gases and vapors, pages 62–63. Knovel, 2003.
- [60] T. R. Marrero and E. A. Mason. Gaseous diffusion coefficients. *J. Phys. Chem. Ref. Data*, 1(1):3–118, 1972.
- [61] D. Wallace and C. Sagan. Evaporation of ice in planetary-atmospheres - ice-covered rivers on Mars. *Icarus*, 39(3):385–400, 1979.
- [62] L. K. Tamppari, D. Bass, B. A. Cantor, I. Daubar, C. Dickinson, D. Fisher, K. Fujii, H. P. Gunnlauggson, T. L. Hudson, D. Kass, A. Kleinbohl, L. Komguem, M. T. Lemmon, M. T. Mellon, J. E. Moores, A. Pankine, J. Pathak, M. Searls, F. Seelos, M. D. Smith, S. E. Smrekar, P. A. Taylor, C. Holstein-Rathlou, W. Weng, J. Whiteway, and M. Wolff. Phoenix and

REFERENCES

- MRO coordinated atmospheric measurements. *J. Geophys. Res.*, 115:E00E17, 2010.
- [63] W. C. Hinds. *Aerosol Technology*. John Wiley and Sons, Inc., 2 edition, 1998.
- [64] W. H. Finlay. *The Mechanics of Inhaled Pharmaceutical Aerosols: An Introduction*. Academic Press, 2001.
- [65] J. Moores. The red planet of dust, 2008. <http://phoenix.lpl.arizona.edu/blogs.php>.
- [66] M. T. Mellon, R. E. Arvidson, H. G. Sizemore, M. L. Searls, D. L. Blaney, S. Cull, M. H. Hecht, T. L. Heet, H. U. Keller, M. T. Lemmon, W. J. Markiewicz, D. W. Ming, R. V. Morris, W. T. Pike, and A. P. Zent. Ground ice at the Phoenix Landing Site: Stability state and origin. *J. Geophys. Res.*, 114:E00E07, 2009.
- [67] S. P. Kounaves, M. H. Hecht, J. Kapit, K. Gospodinova, L. DeFlores, R. C. Quinn, W. V. Boynton, B. C. Clark, D. C. Catling, P. Hredzak, D. W. Ming, Q. Moore, J. Shusterman, S. Stroble, S. J. West, and S. M. M. Young. Wet Chemistry experiments on the 2007 Phoenix Mars Scout Lander mission: Data analysis and results. *J. Geophys. Res.*, 115:E00E10, 2010.
- [68] W. T. Pike, H. Sykulska, and S. Vijendran. Fractal analysis of the microstructure of the Martian soil at the Phoenix Landing Site. *Lunar Planet. Sci. XL*, 2009. abstract 1909.
- [69] G. R. Johnson and G. R. Olhoeft. *Handbook of Physical Properties of Rocks*, volume III, chapter Densities of rocks and minerals, pages 1–28. CRC Press, Boca Raton, Fla, 1984.
- [70] W. A. Deer, R. A. Howie, and J. Zussman. *An Introduction to the Rock Forming Minerals*. Prentice Hall, 1966.
- [71] A. E. Wechsler and P. E. Glaser. Pressure effects on postulated lunar materials. *Icarus*, 4:335–352, 1965.

REFERENCES

- [72] F. Grønvold and E. F. Westrum. α -Ferric Oxide: Low temperature heat capacity and thermodynamic functions. *J. Am. Chem. Soc.*, 81:1780–1783, 1959.
- [73] H. G. Sizemore and M. T. Mellon. Laboratory characterization of the structural properties controlling gas transport in Mars-analog soils. *Icarus*, 197(2):606–620, 2008.
- [74] F. Gori and S. Corasaniti. Theoretical prediction of the thermal conductivity and temperature variation inside mars soil analogues. *Planetary and Space Science*, 52:91–99, 2004.
- [75] H. P. C. Darcy. *Les Fontaines Publiques de la Ville de Dijon*. Victor Dalmont, Paris, 1856.
- [76] A. J. E. J. Dupuit. *Etudes Theoriques et Pratiques sur le Mouvement des Eaux dans les Canaux Découverts et a Travers les Terrains Perméables*. Victor Dalmont, Paris, 1863.
- [77] P. Forchheimer. Wasserbewegung durch Boden. *VDI Z.*, 45:1782–1788, 1901.
- [78] A. Bejan and D. A. Nield. *Convection in Porous Media*. Springer, 2 edition, 1999.
- [79] C. Q. LaMarche, J. S. Curtis, and P. T. Metzger. Permeability of JSC-1A: A lunar soil simulant. *Icarus*, 212(1):383–389, 2011.
- [80] D. D. Joseph, D. A. Nield, and G. Papanicolaou. Nonlinear equation governing flow in a saturated porous medium. *Water Resour. Res.*, 18(4):1049–1052, 1982.
- [81] M. Kaviany. *Principles of Heat Transfer in Porous Media*. Springer, New York, 1995.
- [82] K.-C. Chen. The influence of dust devils on martian water vapour transport, 2011. Master’s thesis.

REFERENCES

- [83] J. Richter. Evidence for significance of other-than-normal diffusion transport in soil gas exchange. *Geoderma*, 8:95–101, 1972.
- [84] E. A. Mason and A. P. Malinauskas. *Gas Transport in Porous Media: The Dusty-Gas Model*, volume 17. Elsevier, New York, 1983.
- [85] S. M. Clifford. A model for the hydrologic and climatic behavior of water on Mars. *J. Geophys. Res.*, 98(E6):10973–11016, 1993.
- [86] W. G. Pollard and R. D. Present. On gaseous self-diffusion in long capillary tubes. *Phys. Rev.*, 73(7):762–774, 1948.
- [87] A. Wheeler. Reaction rate and selectivity in catalyst pores. *Adv. Catal.*, 3: 249–327, 1951.
- [88] R. D. Present. *Kinetic theory of gases*. McGraw-Hill, New York, 1958.
- [89] A. F. Mills. *Mass Transfer*. Prentice Hall, Inc., New Jersey, 2001.
- [90] Y. Demirel. *Nonequilibrium Thermodynamics: Transport and rate processes in physical, chemical and biological systems*. Elsevier, Amsterdam, 2 edition, 2007.
- [91] J. Bzowski, J. Kestin, E. A. Mason, and F. J. Uribe. Equilibrium and transport properties of gas mixtures at low density: Eleven polyatomic gases and five noble gases. *J. Chem. Phys. Ref. Data*, 19(5):1179–1232, 1990.
- [92] J. E. Lennard-Jones. On the determination of molecular fields II. from the equation of state of a gas. *Proc. Roy. Soc. A.*, 106:473–477, 1924.
- [93] K. T. Tang and J. P. Toennies. New combining rules for well parameters and shapes of the van der Waals potential of mixed rare gas systems. *Z. Phys. D*, 1(1):91–101, 1986.
- [94] P. H. Paul. DRFM: A new package for the evaluation of gas-phase transport properties. *Office*, (November), 1997.
- [95] Y. A. Cengel. *Heat and Mass Transfer: A Practical Approach*. McGraw-Hill,

REFERENCES

- 3 edition, 2007.
- [96] J. Appelbaum and D. J. Flood. Solar radiation on Mars. *Solar Energy*, 45(6): 353–363, 1990.
- [97] M. Allison and R. Schmunk. Technical notes on Mars Solar Time as adopted by the Mars24 sunclock, 2004. <http://xpda.com/junkmail/junk156/notes.html>.
- [98] J. Appelbaum, G. A. Landis, and I. Sherman. Solar radiation on Mars-update 1991. *Solar Energy*, 50(1):35–51, 1993.
- [99] H. Savijärvi. A model study of the atmospheric boundary layer in the Mars Pathfinder lander conditions. *Q. J. R. Meteorol. Soc.*, 125:483–493, 1998.
- [100] C. M. Rhie and W. L. Chow. A numerical study of the turbulent flow past and isolated airfoil with trailing edge separation. *AIAA Journal*, 21(11):1525–1532, 1983.
- [101] J. H. Ferziger and M. Peric. *Computational Methods for Fluid Dynamics*. Springer-Verlag, Berlin, Heidelberg, Germany, 1996.
- [102] H. Davarzani, M. Marcoux, P. Costeseque, and M. Quintard. Experimental measurement of the effective diffusion and thermodiffusion coefficients for binary gas mixture in porous media. *Chemical Engineering Science*, 68(18): 5092–5104, 2010.
- [103] PDS. The Planetary Data System, 2010. <http://pds.jpl.nasa.gov/>.
- [104] T. Svitek and B. Murray. Winter frost at Viking Lander 2 site. *J. Geophys. Res.*, 95(B2):1495–1510, 1990.
- [105] W. T. Roach, R. Brown, S. J. Caughey, J. A. Garland, and C. J. Readings. The physics of radiation fog, I, A field study. *Q. J. R. Meteorol. Soc.*, 102: 313–334, 1976.
- [106] F. P. Fanale and W. A. Cannon. Adsorption on the Martian regolith. *Nature*,

REFERENCES

- 230, 1971.
- [107] C. R. Wilke. A viscosity equation for gas mixtures. *J. Chem. Phys.*, 18: 517–519, 1950.
- [108] E. A. Mason and S. C. Saxena. Approximate formula for the thermal conductivity of gas mixtures. *Phys. Fluids*, 1(5):361–369, 1958.
- [109] B. E. Poling, J. M. Prausnitz, and J. P. O’Connell. *The Properties of Gases and Liquids*. McGraw-Hill, 5 edition, 2001.

A

Appendix A: Derivations

A.1 Relationships for an ideal gas mixture

Amagat's law of additive volumes states that

$$V = \sum_{\alpha=1}^n V_{\alpha} \quad (\text{A.1.1})$$

Applying the ideal gas law to each volume of gas gives

$$V_{\alpha} = \frac{N_{\alpha} \cdot R}{T \cdot P} \quad \text{and} \quad V = \frac{N \cdot R}{T \cdot P} \quad (\text{A.1.2})$$

Taking the ratio of these two equations, it follows that

$$\frac{V_{\alpha}}{V} = \frac{N_{\alpha}}{N} = x_{\alpha} \quad (\text{A.1.3})$$

Dalton's law of partial pressures is

$$P = \sum_{\alpha=1}^n P_{\alpha}, \quad \text{where} \quad P_{\alpha} = \rho_{\alpha} R_{\alpha} T \quad (\text{A.1.4})$$

Dividing partial pressure by total pressure and substituting $R_{\alpha} = R/m_{\alpha}$, it gives

$$\frac{P_{\alpha}}{P} = \frac{\rho_{\alpha} \cdot R \cdot T}{m_{\alpha} \cdot P} = c_{\alpha} \frac{R \cdot T}{P} = x_{\alpha} \frac{c \cdot R \cdot T}{P} = x_{\alpha} \quad (\text{A.1.5})$$

A.2 Mixture properties

The mixture viscosity is calculated from method of Wilke [107]:

$$\mu = \frac{x_\alpha \mu_\alpha}{x_\alpha + x_\beta \Phi_{\alpha\beta}} + \frac{x_\beta \mu_\beta}{x_\beta + x_\alpha \Phi_{\beta\alpha}} \quad (\text{A.2.1})$$

where μ is viscosity of the mixture, μ_α , μ_β are pure component viscosities, x_α , x_β are mole fractions, and

$$\Phi_{\alpha\beta} = \frac{\left[1 + \left(\frac{\mu_\alpha}{\mu_\beta} \right)^{\frac{1}{2}} \left(\frac{M_{w\beta}}{M_{w\alpha}} \right)^{\frac{1}{4}} \right]^2}{\left[8 + \left(1 + \frac{M_{w\alpha}}{M_{w\beta}} \right) \right]^{\frac{1}{2}}} \quad (\text{A.2.2})$$

$$\Phi_{\beta\alpha} = \Phi_{\alpha\beta} \frac{\mu_\beta M_{w\alpha}}{\mu_\alpha M_{w\beta}} \quad (\text{A.2.3})$$

The mixture thermal conductivity is estimated by a method analogous to the above for viscosity [108]:

$$k = \frac{x_\alpha k_\alpha}{x_\alpha + x_\beta \Phi_{\alpha\beta}} + \frac{x_\beta k_\beta}{x_\beta + x_\alpha \Phi_{\beta\alpha}} \quad (\text{A.2.4})$$

where k is the thermal conductivity of the mixture, k_α , k_β are the thermal conductivities of the pure components, and the coefficients Φ are identical to those appearing in the viscosity equation (Eqns. A.2.2 and A.2.3). More semi-empirical formulas for estimating viscosities and thermal conductivities of gas mixtures are available in Poling et al. [109].

A.3 Derivation of thermal energy equation

The general form of the energy equation is

$$\frac{\partial}{\partial t}(\rho E) + \nabla \cdot (\rho E \mathbf{v}) = -\nabla \cdot \mathbf{q} - \nabla \cdot (P\mathbf{v}) + \rho \mathbf{g} \cdot \mathbf{v} - \nabla \cdot (\boldsymbol{\tau} \cdot \mathbf{v}) \quad (\text{A.3.1})$$

where E includes internal and kinetic energy¹.

$$E = e + \frac{1}{2}\mathbf{v}^2 \quad (\text{A.3.2})$$

It is advantageous to express the internal energy in terms of enthalpy

$$E = h - \frac{P}{\rho} + \frac{1}{2}\mathbf{v}^2 \quad (\text{A.3.3})$$

so that Eqn. A.3.1 becomes

$$\begin{aligned} \frac{\partial}{\partial t} \left[\rho \left(h + \frac{1}{2}\mathbf{v}^2 \right) - P \right] + \nabla \cdot \left[\rho \left(h + \frac{1}{2}\mathbf{v}^2 \right) \mathbf{v} - P\mathbf{v} \right] = \\ - \nabla \cdot \mathbf{q} - \nabla \cdot (P\mathbf{v}) + \rho \mathbf{g} \cdot \mathbf{v} - \nabla \cdot (\boldsymbol{\tau} \cdot \mathbf{v}) \end{aligned} \quad (\text{A.3.4})$$

This equation is further simplified by assuming an incompressible flow ($\rho=\text{const}$) to be

$$\rho \frac{D}{Dt} \left(h + \frac{1}{2}\mathbf{v}^2 \right) = \frac{\partial P}{\partial t} - \nabla \cdot \mathbf{q} + \rho \mathbf{g} \cdot \mathbf{v} - \nabla \cdot (\boldsymbol{\tau} \cdot \mathbf{v}) \quad (\text{A.3.5})$$

where $\frac{D}{Dt}() = \frac{\partial}{\partial t}() + \mathbf{v} \cdot \nabla()$ is known as the material derivative.

It is common practice to obtain a form of the thermal energy equation, which is suitable for low-speed flows, by removing the contributions of mechanical energy. The part of the energy equation attributable to the kinetic energy is found by forming the dot product of the velocity vector with the momentum equation (Eqn. 2.1.14), which is

$$\rho \frac{D}{Dt} \left(\frac{\mathbf{v}^2}{2} \right) = -\mathbf{v} \cdot \nabla P + \rho \mathbf{v} \cdot \mathbf{g} - \mathbf{v} \cdot [\nabla \cdot \boldsymbol{\tau}] + \mathbf{v} \cdot S_M \quad (\text{A.3.6})$$

Subtracting Eqn. A.3.6 from Eqn. A.3.5 and defining a new source term as $S_E = -\mathbf{v} \cdot S_M$ yields the thermal energy equation

$$\rho \frac{Dh}{Dt} = \frac{\partial P}{\partial t} + \mathbf{v} \cdot \nabla P - \nabla \cdot \mathbf{q} + \mathbf{v} \cdot [\nabla \cdot \boldsymbol{\tau}] - \nabla \cdot [\boldsymbol{\tau} \cdot \mathbf{v}] + S_E \quad (\text{A.3.7})$$

¹The potential energy is considered as work done against the gravitational force and it is included as a source term. The nuclear, radiative, electromagnetic and chemical forms of energy are not included.

APPENDIX A: DERIVATIONS

or using short vector-tensor operations

$$\rho \frac{Dh}{Dt} = \frac{DP}{Dt} - \nabla \cdot \mathbf{q} - (\boldsymbol{\tau} : \nabla \mathbf{v}) + S_E \quad (\text{A.3.8})$$

A.4 Numerical discretization

In finite volume method (FVM), the domain is divided in a set of control volumes (CVs) for which, the governing equations are solved. At the center of each CV lies a computational node at which, results are obtained. The conservation equations in integral form (Eqn. A.4.1) are approximated by using linear interpolation functions. These functions are integrated over each CV, producing fluxes of the conserved variable. This results in a system of algebraic equations for each CV, in which the values of field variables at the CV surface appear.

$$\frac{\partial}{\partial t} \int_V \rho \varphi dV + \int_S \rho \varphi \mathbf{v} \cdot \mathbf{n} dS = \int_S \Gamma \nabla \varphi \cdot \mathbf{n} dS + \int_V q_\varphi dV \quad (\text{A.4.1})$$

In the above equation, φ is a conserved quantity, Γ is the diffusion coefficient and q_φ is the source term. The volume integral in the Eqn. A.4.1 is replaced by the product of the value of the integrand at the CV center and the CV volume

$$\int_V q dV = \bar{q} \Delta V \approx q_P \Delta V \quad (\text{A.4.2})$$

where q_P is the value of q at the CV center. The simplest approximation to the surface integral is the midpoint rule, which follows

$$\int_{S_e} f dS = \bar{f}_e dS_e \approx f_e S_e \quad (\text{A.4.3})$$

Here S_e is the surface area and f_e is the value of f at the cell-face center, which has to be obtained by interpolation. Since this approximation is of second-order accuracy, the value of f_e has to be also computed with the same order accuracy.

The most commonly used approximations are: upwind differencing scheme (UDS) and central differencing scheme (CDS). The first one is very robust and never yields oscillatory solutions. However, it is a first order scheme and adds numerical diffusion especially for coarse grids. The second one, which is a second order scheme, may lead to non-physical oscillations (especially in case of steep gradients), but it is good for oscillating flows and has no artificial diffusion.

ANSYS-CFX 13.0 offers the High Resolution scheme with specified blend factor β , which can blend between UDS and CDS. For small gradients and fine grids, it

APPENDIX A: DERIVATIONS

may lead to pure CDS and to pure UDS for regions of high gradients to prevent non-physical oscillations. With this scheme the advection term is discretized as

$$\varphi_{ip} = \varphi_{up} + \beta \nabla \varphi \cdot \Delta \vec{r} \quad (\text{A.4.4})$$

where φ_{ip} is the value of φ at integration point (ip), φ_{up} is the upwind node value, and \vec{r} is the vector from the upwind node to the ip .

The diffusion term is discretized using the finite element shape functions, which describe the variation of transport quantity φ within an element as

$$\varphi = \sum_{i=1}^{N_{node}} N_i \varphi_i \quad (\text{A.4.5})$$

The shape function, N_i , requires that

$$\sum_{i=1}^{N_{node}} N_i = 1 \quad \text{and at node } j, N_i = \begin{cases} 1 & : i = j \\ 0 & : i \neq j \end{cases} \quad (\text{A.4.6})$$

For example, for a hexahedral element such as one in Fig. A.1, the shape functions are

$$\begin{aligned} N_1(s, t, u) &= (1 - s) (1 - t) (1 - u) \\ N_2(s, t, u) &= s (1 - t) (1 - u) \\ N_3(s, t, u) &= s t (1 - u) \\ N_4(s, t, u) &= (1 - s) t (1 - u) \\ N_5(s, t, u) &= (1 - s) (1 - t) u \\ N_6(s, t, u) &= s (1 - t) u \\ N_7(s, t, u) &= s t u \\ N_8(s, t, u) &= (1 - s) t u \end{aligned} \quad (\text{A.4.7})$$

Thus, the discretized diffusion term is

$$\left(\frac{\partial \varphi}{\partial x} \right)_{ip} = \sum_n \left(\frac{\partial N_n}{\partial x} \right)_{ip} \varphi_n \quad (\text{A.4.8})$$

Note that the net flux through the control volume boundary is the sum of integrals over all CV faces

$$\int_S f dS = \sum_i \int_{S_i} f dS \quad (\text{A.4.9})$$

APPENDIX A: DERIVATIONS

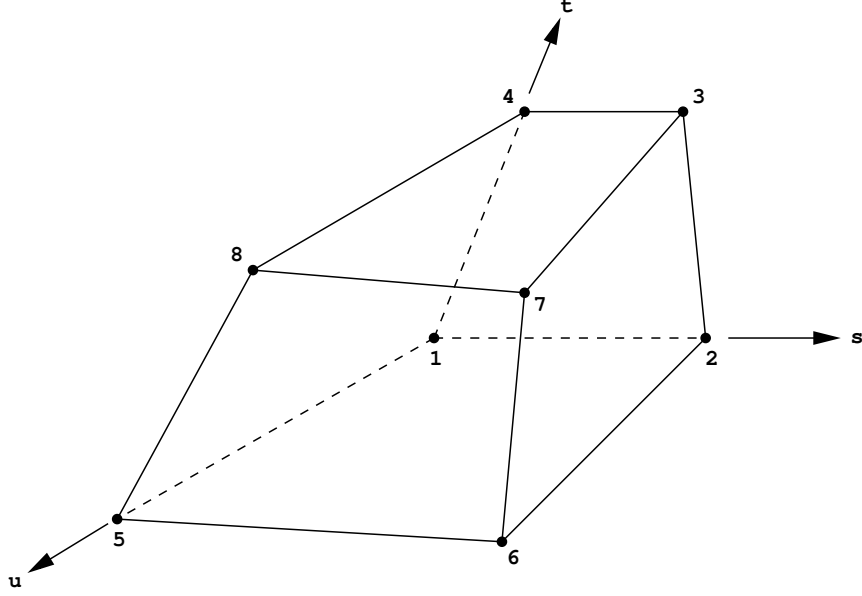


Figure A.1: *Hexahedral element.*

For example, calculating the surface integrals at the mid-point of the faces of CV element (ip), gives the discretized form of the Eqn. 3.1.1 as

$$V \left(\frac{\rho\varphi - \rho^o\varphi^o}{\Delta t} \right) + \sum_{ip} \dot{m}_{ip}\varphi_{ip} = \sum_{ip} \left(\Gamma \frac{\partial\varphi}{\partial x_j} \Delta n_j \right)_{ip} + S_\varphi V \quad (\text{A.4.10})$$

Here \dot{m}_{ip} is defined as

$$\dot{m}_{ip} = (\rho \mathbf{U}_j \Delta n_j)_{ip} \quad (\text{A.4.11})$$

and V is the control volume, Δt is the time-step, Δn_j is the discrete outward surface vector, and the superscript “ o ” denotes the previous time step. The transient term in Eqn. A.4.10 is discretized using the first order backward Euler scheme, although in this work a second order scheme is used. With the second order backward Euler scheme, the beginning and final time step values are respectively

$$(\rho\varphi)^{n-\frac{1}{2}} = (\rho\varphi)^o + \frac{1}{2} [(\rho\varphi)^o - (\rho\varphi)^{oo}] \quad (\text{A.4.12})$$

$$(\rho\varphi)^{n+\frac{1}{2}} = (\rho\varphi)^o + \frac{1}{2} [(\rho\varphi) - (\rho\varphi)^o] \quad (\text{A.4.13})$$

APPENDIX A: DERIVATIONS

Using these values, the resulting approximation of time integral is

$$\begin{aligned} \frac{\partial}{\partial t} \int_V \rho\varphi \, dV &\approx V \frac{(\rho\varphi)^{n+\frac{1}{2}} - (\rho\varphi)^{n-\frac{1}{2}}}{\Delta t} \\ &\approx V \frac{1}{\Delta t} \left(\frac{3}{2} (\rho\varphi) - 2 (\rho\varphi)^o + \frac{1}{2} (\rho\varphi)^{oo} \right) \end{aligned} \quad (\text{A.4.14})$$

This scheme is implicit and gives a good degree of robustness. It may create some non-physical oscillations, especially at large Δt .

The accuracy of solution in previously described approximations is governed by the number of cells or time-step factor. In general, the accuracy of the solution increases with number of cells and decreases with time-step. Although, higher order approximations reduces errors more quickly with mesh or time-step refinement, they are less numerically stable and more computationally expensive.

A.5 Relationships for the mass fluxes

From the definition of $\mathbf{j}_{CO_2}^G$, $\mathbf{j}_{H_2O}^G$, and $\mathbf{j}_{H_2O}^S$ [50],

$$\begin{aligned}\mathbf{j}_{CO_2}^G + \mathbf{j}_{H_2O}^G + \mathbf{j}_{H_2O}^S &= \rho_{CO_2}^G (\mathbf{v}_{CO_2}^G - \mathbf{v}) \\ &+ \rho_{H_2O}^G (\mathbf{v}_{H_2O}^G - \mathbf{v}) \\ &+ \rho_{H_2O}^S (\mathbf{v}_{H_2O}^S - \mathbf{v})\end{aligned}\quad (\text{A.5.1})$$

From Eqn. 2.1.9,

$$\rho = \rho_{CO_2}^G + \rho_{H_2O}^G + \rho_{H_2O}^S \quad (\text{A.5.2})$$

and from Eqn. 2.1.11,

$$\rho \mathbf{v} = \rho_{CO_2}^G \mathbf{v}_{CO_2}^G + \rho_{H_2O}^G \mathbf{v}_{H_2O}^G + \rho_{H_2O}^S \mathbf{v}_{H_2O}^S \quad (\text{A.5.3})$$

Re-arranging Eqn. A.5.1 and using equations A.5.2 to A.5.3, it follows

$$\begin{aligned}\mathbf{j}_{CO_2}^G + \mathbf{j}_{H_2O}^G + \mathbf{j}_{H_2O}^S &= (\rho_{CO_2}^G \mathbf{v}_{CO_2}^G + \rho_{H_2O}^G \mathbf{v}_{H_2O}^G + \rho_{H_2O}^S \mathbf{v}_{H_2O}^S) - \\ &- \mathbf{v} (\rho_{CO_2}^G + \rho_{H_2O}^G + \rho_{H_2O}^S) \\ &= \rho \mathbf{v} - \rho \mathbf{v}\end{aligned}\quad (\text{A.5.4})$$

Finally,

$$\mathbf{j}_{CO_2}^G + \mathbf{j}_{H_2O}^G + \mathbf{j}_{H_2O}^S = 0 \quad (\text{A.5.5})$$

A.6 Correlation equations for the functionals

Following is a description of the correlation equations for the functionals used in the calculation of the thermal diffusion factor. Defining $f = \frac{M_{w\alpha}}{M_{w\beta}}$ and assuming α as the heavier component ($M_{w\alpha} > M_{w\beta}$), the expressions for S and Q are as follows:

$$S_\alpha = f \left(\frac{2}{1+f} \right)^{\frac{1}{2}} \frac{\Omega_{\alpha\alpha}^{(22)*} \sigma_{\alpha\alpha}^2}{\Omega_{\alpha\beta}^{(11)*} \sigma_{\alpha\beta}^2} - \frac{4fA_{\alpha\beta}^*}{(1+f)^2} + \frac{15(f-1)}{2(1+f)^2} \quad (\text{A.6.1})$$

$$S_\beta = \left(\frac{2}{f+f^2} \right)^{\frac{1}{2}} \frac{\Omega_{\beta\beta}^{(22)*} \sigma_{\beta\beta}^2}{\Omega_{\alpha\beta}^{(11)*} \sigma_{\alpha\beta}^2} - \frac{4fA_{\alpha\beta}^*}{(1+f)^2} + \frac{15f(1-f)}{2(1+f)^2} \quad (\text{A.6.2})$$

$$Q_\alpha = \left(\frac{2}{1+f} \right)^{\frac{1}{2}} \frac{\Omega_{\alpha\alpha}^{(22)*} \sigma_{\alpha\alpha}^2}{\Omega_{\alpha\beta}^{(11)*} \sigma_{\alpha\beta}^2} \frac{(2.5 - 1.2B_{\alpha\beta}^*) f^2 + 3 + 1.2fA_{\alpha\beta}^*}{1+f} \quad (\text{A.6.3})$$

$$Q_\beta = \left(\frac{2f}{1+f} \right)^{\frac{1}{2}} \frac{\Omega_{\beta\beta}^{(22)*} \sigma_{\beta\beta}^2}{\Omega_{\alpha\beta}^{(11)*} \sigma_{\alpha\beta}^2} \frac{(2.5 - 1.2B_{\alpha\beta}^*) + 3f^2 + 1.2fA_{\alpha\beta}^*}{f+f^2} \quad (\text{A.6.4})$$

$$\begin{aligned} Q_{\alpha\beta} &= \frac{8(1+f)}{5f^{\frac{1}{2}}} \frac{\Omega_{\alpha\alpha}^{(22)*} \sigma_{\alpha\alpha}^2}{\Omega_{\alpha\beta}^{(11)*} \sigma_{\alpha\beta}^2} \frac{\Omega_{\beta\beta}^{(22)*} \sigma_{\beta\beta}^2}{\Omega_{\alpha\beta}^{(11)*} \sigma_{\alpha\beta}^2} + \frac{4fA_{\alpha\beta}^*}{(1+f)^2} (11 - 2.4B_{\alpha\beta}^*) \\ &+ 15 \left(\frac{f-1}{f+1} \right)^2 (2.5 - 1.2B_{\alpha\beta}^*) \end{aligned} \quad (\text{A.6.5})$$

A.7 Combination rules for mixtures

Following the method of Bzowski et al. [91], the potential parameters for mixtures are calculated using

$$\sigma_{\alpha\beta} = \frac{\sigma_\alpha + \sigma_\beta}{2} \quad (\text{A.7.1})$$

$$\epsilon_{\alpha\beta} = (\epsilon_\alpha \epsilon_\beta)^{\frac{1}{2}} \left[\frac{(\sigma_\alpha - \chi_\alpha)^3 (\sigma_\beta - \chi_\beta)^3}{(\sigma_{\alpha\beta} - \chi_{\alpha\beta})^6} \right] \frac{C_{\alpha\beta}^{(6)}}{(C_\alpha^{(6)} C_\beta^{(6)})^{\frac{1}{2}}} \quad (\text{A.7.2})$$

where

$$\chi_\alpha = \sigma_\alpha \left[1 - \left(\frac{C_\alpha^*}{2.2} \right)^{\frac{1}{6}} \right] \quad (\text{A.7.3})$$

$$\chi_\beta = \sigma_\beta \left[1 - \left(\frac{C_\beta^*}{2.2} \right)^{\frac{1}{6}} \right] \quad (\text{A.7.4})$$

and

$$C_\alpha^* = \frac{C_\alpha^{(6)}}{\epsilon_\alpha \sigma_\alpha^6} \quad (\text{A.7.5})$$

$$C_\beta^* = \frac{C_\beta^{(6)}}{\epsilon_\beta \sigma_\beta^6} \quad (\text{A.7.6})$$

The value of $C_{\alpha\beta}^{(6)}$ is calculated within an accuracy of 1% using

$$C_{\alpha\beta}^{(6)} = 2\alpha_\alpha \alpha_\beta \left[\frac{\alpha_\alpha^2}{C_\alpha^{(6)}} + \frac{\alpha_\beta^2}{C_\beta^{(6)}} \right]^{-1} \quad (\text{A.7.7})$$

where α_α and α_β are the dipole polarizabilities.

A.8 Relationships for the collision integrals

Defining $z = \ln(T^*)$, the collision integrals from Paul [94] are

$$\Omega^{(11)*} = \exp\left(\sum_{i=1}^5 a_i z^i\right) \quad (\text{A.8.1})$$

and

$$\Omega^{(22)*} = \exp\left(\sum_{i=1}^5 b_i z^i\right) \quad (\text{A.8.2})$$

The coefficients a and b for the ranges $0.2 \leq T^* < 1$ and $1 \leq T^* < 10$ are given in Table A.1. Higher order coefficients are calculated using

$$A^* = \frac{\Omega^{(22)*}}{\Omega^{(11)*}} \quad (\text{A.8.3})$$

$$C^* = 1 + \frac{1}{3} \sum_{i=1}^5 i a_i z^{i-1} \quad (\text{A.8.4})$$

and

$$B^* = 4C^* - 3C^{*2} - \frac{1}{9} \sum_{i=2}^5 i(i-1) a_i z^{i-2} \quad (\text{A.8.5})$$

The above expressions are valid only for a temperature range that is relevant in this work ($T^* \leq 10$). The relationships for a higher temperature range are available in Bzowski et al. [91].

$0.2 \leq T^* < 1$	$i=0$	1	2	3	4	5
\mathbf{a}_i	0.295402	-0.510069	0.189395	0.484463	0.417806	0.122148
\mathbf{b}_i	0.46641	-0.56991	0.19591	0.747363	0.662153	0.188447
$1 \leq T^* < 10$	$i=0$	1	2	3	4	5
\mathbf{a}_i	0.295402	-0.510069	0.189395	-0.045427	0.0037928	0.0
\mathbf{b}_i	0.46641	-0.56991	0.19591	-0.03879	0.00259	0.0

Table A.1: *The coefficients a and b for the collision integrals.*

B

Appendix B: Code

B.1 *thfactor.m*

```
function AlphaT21=thfactor(T)
% Function 'thfactor' calculates the thermal diffusion factor for the mixture of
% water and carbon dioxide based on the method presented by Bzowski et al. [91].
%%%%%%%%%%%%%%%%%%%%%%%%%%%%%%%%%%%%%%%%%%%%%%%%%%%%%%%%%%%%%%%%%%%%%%%%
% Initialization
%%%%%%%%%%%%%%%%%%%%%%%%%%%%%%%%%%%%%%%%%%%%%%%%%%%%%%%%%%%%%%%%%%%%%%%%
% Volume mixing ratio is calculated from Whiteway et al. [51] using values of
% pressure at a height of 4 km.
P = 522; % [Pa] % Initial atmospheric pressure %
PH2O = 0.73; % [Pa] % Initial vapour pressure %
kb = 1.38066e-23; % [J/K] % Stefan-Boltzmann's constant %
R = 8314.47; % [J/(kmol K)] % Universal gas constant %

% Clear screen
clc;
%%%%%%%%%%%%%%%%%%%%%%%%%%%%%%%%%%%%%%%%%%%%%%%%%%%%%%%%%%%%%%%%%%%%%%%%
% Display table header
%%%%%%%%%%%%%%%%%%%%%%%%%%%%%%%%%%%%%%%%%%%%%%%%%%%%%%%%%%%%%%%%%%%%%%%%
fprintf('\n          The temperature is: %3g K',T);
fprintf('\n          Components:  1 = CO2  2 = H2O \n');
fprintf('\n-----');
fprintf('\n      Variable          |    1    |    2    |    1,2    ');
fprintf('\n-----\n');
% Partial pressure over ice from Buck [53]
% Psat = 611.35 * exp( 22.542 * ( T - 273.16 ) * ( T + 0.32 )^-1 ); % [Pa]
%%%%%%%%%%%%%%%%%%%%%%%%%%%%%%%%%%%%%%%%%%%%%%%%%%%%%%%%%%%%%%%%%%%%%%%%
% Gas mixture properties
%%%%%%%%%%%%%%%%%%%%%%%%%%%%%%%%%%%%%%%%%%%%%%%%%%%%%%%%%%%%%%%%%%%%%%%%
M1=44.0096; % [g/mol] % Molecular weight of CO2
M2=18.0153; % [g/mol] % Molecular weight of H2O
x2=PH2O/P; % Molar fraction of H2O
x1=1-x2; % Molar fraction of CO2
x12=x1+x2; % Sum of molar fraction should be 1
M12=x1*M1+x2*M2; % Mean molar mass
MF1=x1*M1/M12; % Mass fraction of carbon dioxide
MF2=x2*M2/M12; % Mass fraction of water
MF12=MF1+MF2; % Sum of mass fraction should be 1
PCO2=P-PH2O; % [Pa] % Partial pressure of CO2
% Specific Heat Capacity of carbon dioxide from Yaws [47]
Cp1=(27.437+0.042315*T-0.00001955*T^2+0.0000000039968*T^3-0.00000000000029872*T^4)
/M1*10^3; % [J/(kg K)]
% Specific heat capacity of water vapour from www.engineeringtoolbox.com
% Second order polynomial interpolation is used
% Valid for temperature range: 175 - 325 K
Cp2=0.0009904761905*T^2-0.3580952381*T+1882.571429; % [J/(kg K)]
% Specific heat capacity of the mixture from Eqn. 2.1.8
Cp12=MF1*Cp1+MF2*Cp2; % [J/(kg K)]
% Dynamic viscosity of carbon dioxide from Yaws [45]
eta1=0.0000011336+0.000000049918*T-0.00000000010876*T^2; %[Pa s]
```

APPENDIX B: CODE

```

% Dynamic viscosity of water from Crifo [48]
eta2=0.0000925*(T/300)^1.1; % [Pa s]
% Dynamic viscosity of the mixture from Eqn. 2.1.8
eta12=MF1*eta1+MF2*eta2; % [Pa s]
% The coefficient of thermal conductivity of carbon dioxide from Yaws [46]
lam1=(-0.01183+0.00010174*T-0.000000022242*T^2); % [W/m K]
% The coefficient of thermal conductivity of water from Eucken [49]
lam2=(Cp2+(5/4)*(R/M2))*eta2; % [W/m K]
% The coefficient of thermal conductivity of the mixture from Eqn. 2.1.8
lam12=(x1*(M1/M12)*lam1+x2*(M2/M12)*lam2); % [W/m K]
%%%%%%%%%%%%%%%%%%%%%%%%%%%%%%%%%%%%%%%%%%%%%%%%%%%%%%%%%%%%%%%%%%%%%%%%
% Potential parameters for carbon dioxide and water
%%%%%%%%%%%%%%%%%%%%%%%%%%%%%%%%%%%%%%%%%%%%%%%%%%%%%%%%%%%%%%%%%%%%%%%%
%1% %%CO2%% - {Sandia National Laboratories (1997) - Table B1 (Appendix B)}
sigma_11=3.769; % [Angstrom]
ek_11=245.30; % [K]
e_11=ek_11*kb*1e+07; % [erg]
alpha_11=2.65; % [A^3]
C1_6=1.86;

%2% %%H2O%% - {Sandia National Laboratories (1997) - Table B1 (Appendix B)}
sigma_22=2.673; % [Angstrom] Alter: 2.71
ek_22=535.21; % [K] Alter: 506
e_22=ek_22*kb*1e+07; % [erg]
alpha_22=1.45; % [A^3] Alter: 1.47
mu_22=1.847e-18; % [esu cm] % Dipole moment of the polar molecule % Alter: 1.83e-18
C2_6=1.612;

%12% %%CO2-H2O%% - {Bzowski et al. [91]}
C1red=C1_6/(e_11*sigma_11^6);
C2red=C2_6/(e_22*sigma_22^6);
C12_6=(2*alpha_11*alpha_22)/(((alpha_11^2)/C1_6)+((alpha_22^2)/C2_6));

a_1=sigma_11*(1-(C1red/2.2)^(1/6));
a_2=sigma_22*(1-(C2red/2.2)^(1/6));
a_12=0.5*(a_1+a_2);

% To get sigma_12, the following equation need to be solved numerically:
% sigma_12-a_12=0.5*((sigma_11-a_1)+(sigma_22-a_2))*(1+0.5*(log(sigma_12-a_12)
% -(1/7)*lnE));
% where
% lnE=0.5*log(e_11*e_22) + 3*log(sigma_11-a_1)*(sigma_22-a_2)
% - ((sigma_11-a_1)/((sigma_11-a_1)+(sigma_22-a_2)))*log(e_11/(sigma_11-a_1))
% - ((sigma_22-a_2)/((sigma_11-a_1)+(sigma_22-a_2)))*log(e_22/(sigma_22-a_2));
% Bzowski et al. [91] proposed the first approximation to the solution,
% which changes the value of sigma_12 by less than 1%
sigma_12=0.5*(sigma_11+sigma_22); % [Angstrom]
ek_12=((ek_11*ek_22)^(0.5))*(((sigma_11-a_1)^3)*((sigma_22-a_2)^3))
/((sigma_12-a_12)^6)*C12_6/((C1_6*C2_6)^(0.5)); % [K]

%%%%%%%%%%%%%%%%%%%%%%%%%%%%%%%%%%%%%%%%%%%%%%%%%%%%%%%%%%%%%%%%%%%%%%%%
% Calculate reduced temperatures
%%%%%%%%%%%%%%%%%%%%%%%%%%%%%%%%%%%%%%%%%%%%%%%%%%%%%%%%%%%%%%%%%%%%%%%%
red.T11=T/ek_11;
red.T22=T/ek_22;
red.T12=T/ek_12;

%%%%%%%%%%%%%%%%%%%%%%%%%%%%%%%%%%%%%%%%%%%%%%%%%%%%%%%%%%%%%%%%%%%%%%%%
% Relationships for the Collision Integrals
% {Sandia National Laboratories (1997)}
%%%%%%%%%%%%%%%%%%%%%%%%%%%%%%%%%%%%%%%%%%%%%%%%%%%%%%%%%%%%%%%%%%%%%%%%
% Let
z11=log(red.T11);
z22=log(red.T22);
z12=log(red.T12);

% and
% 0.2<T*<1          1<T*<10
a0=0.295402;         c0=0.295402;
a1=-0.510069;        c1=-0.510069;
a2=0.189395;         c2=0.189395;
a3=0.484463;         c3=-0.045427;
a4=0.417806;         c4=0.0037928;
a5=0.122148;         c5=0.0;

b0=0.46641;          d0=0.46641;
b1=-0.56991;         d1=-0.56991;
b2=0.19591;          d2=0.19591;
b3=0.747363;         d3=-0.03879;
b4=0.662153;         d4=0.00259;
b5=0.188447;         d5=0.0;

if red.T12<1
omega12_11=exp(a0*(z12^0)+a1*(z12^1)+a2*(z12^2)+a3*(z12^3)+a4*(z12^4)
+a5*(z12^5));
omega12_22=exp(b0*(z12^0)+b1*(z12^1)+b2*(z12^2)+b3*(z12^3)+b4*(z12^4)
+b5*(z12^5));
C12=1+(1/3)*(1*a1*(z12^0)+2*a2*(z12^1)+3*a3*(z12^2)+4*a4*(z12^3)

```

APPENDIX B: CODE

```

+5*a5*(z12^4));
B12=(4*C12)-(3*(C12^2))-((1/9)*((2*a2*(z12^0)+(6*a3*(z12^1)+(12*a4*(z12^2)
+(20*a5*(z12^3))));
else
omega12.11=exp(c0*(z12^0)+c1*(z12^1)+c2*(z12^2)+c3*(z12^3)+c4*(z12^4)+c5*(z12^5));
omega12.22=exp(d0*(z12^0)+d1*(z12^1)+d2*(z12^2)+d3*(z12^3)+d4*(z12^4)+d5*(z12^5));
C12=1+(1/3)*(1*c1*(z12^0)+2*c2*(z12^1)+3*c3*(z12^2)+4*c4*(z12^3)+5*c5*(z12^4));
B12=(4*C12)-(3*(C12^2))-((1/9)*((2*c2*(z12^0)+(6*c3*(z12^1)+(12*c4*(z12^2)
+(20*c5*(z12^3))));
end
if red_T11<1
omega11.22=exp(b0*(z11^0)+b1*(z11^1)+b2*(z11^2)+b3*(z11^3)+b4*(z11^4)+b5*(z11^5));
else
omega11.22=exp(d0*(z11^0)+d1*(z11^1)+d2*(z11^2)+d3*(z11^3)+d4*(z11^4)+d5*(z11^5));
end
if red_T22<1
omega22.22=exp(b0*(z22^0)+b1*(z22^1)+b2*(z22^2)+b3*(z22^3)+b4*(z22^4)+b5*(z22^5));
else
omega22.22=exp(d0*(z22^0)+d1*(z22^1)+d2*(z22^2)+d3*(z22^3)+d4*(z22^4)+d5*(z22^5));
end
A12=omega12.22/omega12.11;
% Order i and j such that m-j<m.i and define z=m.i/m.-j
z=M1/M2;
%%%%%%%%%%%%%%%%%%%%%%%%%%%%%%%%%%%%%%%%%%%%%%%%%%%%%%%%%%%%%%%%%%%%%%%%
% Full expression for the thermal diffusion factor
%%%%%%%%%%%%%%%%%%%%%%%%%%%%%%%%%%%%%%%%%%%%%%%%%%%%%%%%%%%%%%%%%%%%%%%%
S1=z*((2/(1+z))^0.5)*(omega11.22/omega12.11)*((sigma.11^2)/(sigma.12^2))
-((4*z*A12)/((1+z)^2))+((15*(z-1))/(2*(1+z)^2));
S2=((2/(z+(z^2)))^0.5)*(omega22.22/omega12.11)*((sigma.22^2)/(sigma.12^2))
-((4*z*A12)/((1+z)^2))+((15*z*(1-z))/(2*(1+z)^2));
Q1=((2/(1+z))^0.5)*(omega11.22/omega12.11)*((sigma.11^2)/(sigma.12^2))
*((2.5-1.2*B12)*(z^2))+3+(1.2*z*A12)/(1+z);
Q2=((2*z)/(1+z))^0.5*(omega22.22/omega12.11)*((sigma.22^2)/(sigma.12^2))
*((2.5-1.2*B12)+(3*(z^2)+(1.2*z*A12)/(z+(z^2)));
Q12=(8*(1+z)/(5*(z^(0.5))))*(omega11.22/omega12.11)*((sigma.11^2)/(sigma.12^2))
*(omega22.22/omega12.11)*((sigma.22^2)/(sigma.12^2))+((4*z*A12)/((1+z)^2))
*(11-2.4*B12)+15*((z-1)/(z+1))^2*(2.5-1.2*B12);
%%%%%%%%%%%%%%%%%%%%%%%%%%%%%%%%%%%%%%%%%%%%%%%%%%%%%%%%%%%%%%%%%%%%%%%%
% The thermal diffusion factor
%%%%%%%%%%%%%%%%%%%%%%%%%%%%%%%%%%%%%%%%%%%%%%%%%%%%%%%%%%%%%%%%%%%%%%%%
AlphaT12=(6*C12-5)*((x1*S1-x2*S2)/((x1^2)*Q1+(x2^2)*Q2+(x1*x2*Q12)));
AlphaT21=-AlphaT12;
% Note: The binary thermal diffusion factor
% is assymmetric under exchange of indices.
% Here, it is multiplied by (-1) in order to get
% the thermal diffusion factor for H2O in CO2.
fprintf('Pressure (Pa) %11g %11g %11g \n',PCO2,PH2O,P);
fprintf('Molecular Weight (kg/kmol) %11g %11g %11g \n',M1,M2,M12);
fprintf('Mole fraction (mol/mol) %11g %11g %11g \n',x1,x2,x12);
fprintf('Mass fraction (kg/kg) %11g %11g %11g \n',MF1,MF2,MF12);
fprintf('Heat Capacity (J/Kg K) %11g %11g %11g \n',Cp1,Cp2,Cp12);
fprintf('Dynamic Viscosity (Pa s) %11g %11g %11g \n',etal,eta2,etal2);
fprintf('Thermal conductivity (W/m K) %11g %11g %11g \n',lam1,lam2,lam12);

fprintf('\n-----');
fprintf('\n i | 1 | 2 | 1');
fprintf('\n j | 1 | 2 | 2');
fprintf('\n-----\n');

fprintf('sigma (A) %11g %11g %11g \n',sigma.11,sigma.22,sigma.12);
fprintf('e/kb (K) %11g %11g %11g \n',ek.11,ek.22,ek.12);
fprintf('T (K) %11g %11g %11g \n',red.T11,red.T22,red.T12);
fprintf('-----\n\n');
disp(['The thermal diffusion factor is: ', num2str(AlphaT21)]);

```